UNIVERSITY OF CALIFORNIA
RIVERSIDE

The Study of Mechanical Motion Using Photoreactions in the Presence of a Magnetic Field

A Dissertation submitted in partial satisfaction
of the requirements for the degree of

Doctor of Philosophy

in

Materials Science and Engineering

by

Jacob B. Rodriguez

March 2024

Dissertation Committee:
Dr. Christopher J. Bardeen Chairperson
Dr. Pingyun Feng
Dr. Alex Greaney

The Dissertation of Jacob B. Rodriguez is approved:

_____

_____

_____

Committee Chairperson

University of California, Riverside

Portions of the dissertation are adapted with permission from the following references:

Chapter 3:

Rodriguez, J. B.; Lam, K.; Anwar, T. Bin; Bardeen, C. J. Robust Supercooled Liquid Formation Enables All-Optical Switching Between Liquid and Solid Phases of TEMPO. ACS Omega 2024. https://doi.org/10.1021/acsomega.3c06717.

ABSTRACT OF THE DISSERTATION

The Study of Mechanical Motion Using Photoreactions in the Presence of a Magnetic Field

by

Jacob B. Rodriguez

Doctor of Philosophy, Graduate Program in Materials Science and Engineering
University of California, Riverside, March 2024
Dr. Christopher J. Bardeen, Chairperson

This dissertation delves into the field of photomechanical motion, exploring the manipulation of materials using light. Central to the research is the study of TEMPO, hexaarylbiimidazole (HABI), and pyrolytic graphite (PG), each offering unique insights into energy transfer and material control. The study begins with TEMPO, demonstrating its capabilities in controlled mechanical motion due to its stable free radical properties. This exploration lays the groundwork for further investigations into HABI and PG, where their photoresponsive behavior is examined. An important aspect of this research is the ability of light to alter the magnetic susceptibility of materials, enabling controlled movement in magnetic fields.

This dissertation underscores the importance of understanding the thermal and magnetic properties of materials in developing advanced technologies. The implementation of photothermal and photochemical techniques has broad applications, from magnetic levitation to sophisticated manufacturing processes. Future research is suggested to

develop new methods leveraging light-matter interactions, with vast potential for advancements in energy systems, manufacturing, and biomedical technologies.

In summary, this work contributes significantly to the understanding of photomechanical motion, offering new methodologies with far-reaching implications in various scientific and technological domains.

Table of Contents

List of Tables

List of Figures

Chapter 1. Introduction

Light is one way to transfer energy from one part of the galaxy to the other. It can be explained as a flow of photons, which are weightless bundles of energy. Light allows for precise spatial and temporal control.[1] By adjusting parameters such as light intensity, wavelength, and duration, one can precisely control the initiation and extent of photomechanical motion.[2] This high level of control is valuable in applications requiring fine-tuned movements such as biomedical imaging[3–5], laser cutting[6,7], and photolithography in semiconductor manufacturing[8] to name a few. Photomechanical motion refers to the movement or deformation of materials in response to light. This phenomenon occurs when materials undergo physical changes, such as shape distortion, when exposed to light.[9] The interaction between light and the material can induce various effects, including bending[10], twisting[11], crawling[12], rolling[13], and jumping[14]. The process often involves the absorption of light energy by the material, leading to alterations in its structure or properties, which, in turn, result in observable mechanical motion. Light-driven mechanisms operate without physical contact, making them non-invasive. This is particularly advantageous in applications like laser eye surgery[15], biomedical diagnostics[16], and light-driven sensors[17] involving delicate or sensitive materials where traditional mechanical methods might be disruptive or damaging.

There are multiple ways light can be converted into energy, one of them being photochemically.[18] Photochemical reactions can be selectively activated by light of specific wavelengths. This selectivity allows for precise control over when and where the reaction occurs, enabling targeted mechanical motion in a controlled manner.

Photochemical reactions can also exhibit rapid response times and have tunable parameters.[19] However, photochemical reactions exhibit disadvantages as well. Photochemical reactions can be sensitive to environmental conditions, such as temperature.[20] Variations in these conditions may influence the efficiency and reliability of the photochemical process. Some photoactive compounds may experience photodegradation or loss of activity over time due to prolonged exposure to light.[21] This can limit the long-term stability and durability of photochemical systems.

Besides converting light photochemically into energy, there are also radiation pressure and photothermal methods. Radiation pressure refers to the mechanical force exerted by electromagnetic radiation (such as light) on a surface or object.[22] This force arises due to the transfer of momentum from photons to the surface or object upon interaction. The concept is based on the principle that light carries momentum, and when it interacts with matter, it imparts this momentum, resulting in a pressure-like force. Photothermal refers to a process or phenomenon in which light is converted into heat.[23] This conversion occurs when light is absorbed by a material, and the absorbed energy is transformed into thermal energy, raising the temperature of the material.

Another concept that we explore in this lab is utilizing the magnetic properties of materials in order to generate photomechanical motion in the presence of a magnetic field, and that is the backbone of this dissertation. Light can modify an object's magnetic susceptibility by changing its internal electron configuration.[24] Magnetic susceptibility indicates the degree of magnetization of a material in response to an applied magnetic

field.[25] In a simple case, the creation of unpaired electrons would make an object paramagnetic, causing it to be attracted to a nearby magnet.

There are three main types of magnetism: ferromagnetism, paramagnetism, and diamagnetism.[26] Ferromagnetism is a property of certain materials that have a natural magnetic moment and can be magnetized to retain a permanent magnetic state. This is due to the alignment of unpaired spins in the material, even without the presence of a magnetic field. Paramagnetism is a property of some materials that are attracted to a magnet when in the presence of a magnetic field. Without the field, those materials have randomly oriented unpaired electrons, giving a net magnetic moment. They have a positive magnetic susceptibility (χ). Some examples are triplet states and free radicals. Diamagnetism is a property of all matter where there are no unpaired electrons. This is because all orbital shells are filled. Under an applied magnetic field, however, the spins are opposed by the field, causing them to align opposite the magnetic field. This gives the material a negative χ. Paramagnetic materials have diamagnetism since all materials exhibit diamagnetism, but the magnitude of paramagnetism is so large that it cancels out the diamagnetism.

To exploit the properties of magnetism, we studied the stable free radical 2,2,6,6-tetramethyl-1-piperidinyloxy[27] (TEMPO) (**Figure 1.1**) Before attempting to change the properties of any materials, we doped the polymer, polymethyl methacrylate (PMMA), with TEMPO. We decided on PMMA because it is clear, commercially available, and unreactive to the ambient atmosphere.

We used TEMPO as a test case to see if an object with free radicals can move when near a magnet. As expected, a TEMPO-doped polymer is attracted to a magnet since it is

paramagnetic. While analyzing TEMPO, we fortuitously came across the phenomenon of supercooling (which will be discussed in the next section of this chapter).

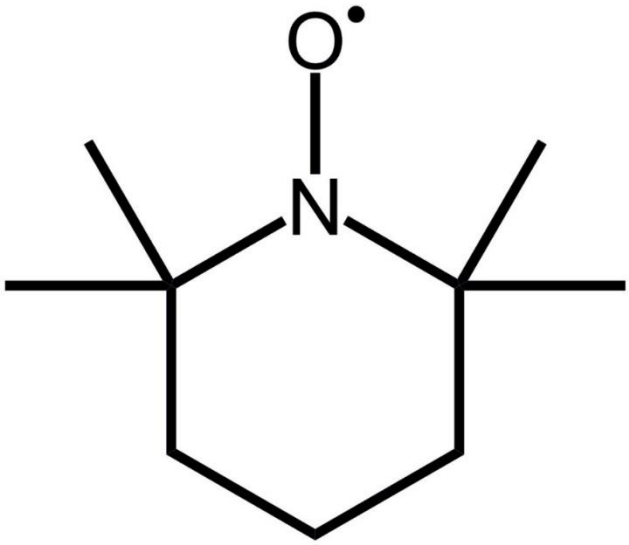

Figure 1.1. Chemical structure of 2,2,6,6-tetramethyl-1-piperidinyloxy (TEMPO)

With TEMPO demonstrating motion, we had two strategies to show that creating radical spins and then moving objects under the presence of a magnetic field is possible. Approach one: Use photochemistry to create radical spins in ortho-chloro-hexaarylbiimidizole (o-Cl-HABI, but it will be called HABI for the purposes of this dissertation). Approach two: Photothermally creating radical spins by heating up pyrolytic graphite (PG). Both approaches exhibit a tunable way to increase/decrease the strength of motion depending on the strength of the magnetic field. In theory, photothermal reactions can go on forever since it is not doing photochemistry that may lead to degradation of breaking and making bonds which is a reason why we moved forward with photothermal reactions over photochemical ones.

The rest of this chapter is organized into three parts: the supercooling of TEMPO, photochemical changes involving HABI, and photothermal changes involving PG.

1.1 Supercooled TEMPO

TEMPO is a stable free radical.[27] The nitroxyl group on it allows TEMPO to persist as a radical. Normally, free radicals are unstable.[28] They are usually highly reactive and will react with the air and the molecules around them.

1.1.1 Applications

TEMPO and its derivatives are stable nitroxyl radicals and are used in a variety of applications. Given the properties of these radicals, they can be used as oxidizing agents.[29] Among the various nitroxyl-radical catalysts, TEMPO is most frequently used because it is commercially available.[30] In addition, TEMPO radicals are used as scavengers of unstable radicals species.[31] For example, to afford stable trialkylhydroxylamines, the trapping of transient carbon-centered radicals by nitroxides such as TEMPO is used.

TEMPO radicals are also found in applications in spin labels in the study of conformation and structural mobility of biological systems.[32] For example, starburst dendrimers can be characterized by Electron Paramagnetic Resonance (EPR) with TEMPO radicals as spin labels. TEMPO radicals are also frequently employed as functional materials, such as oxidants of alcohols[33] and polymeric stabilizers[34]. Since TEMPO is stable, it can be attached to other molecules, which is called a spin label. The spin label can then be used in EPR to study the dynamics and interactions of the labeled molecule. EPR is a characterization method used to study molecules with unpaired electrons. An example of an EPR spectrum is shown in **Figure 1.2**. It can provide information about the immediate

surroundings and magnetic behavior of unpaired electrons. It can be used with studying radicals formed in chemical reactions, which I will discuss in the next section.

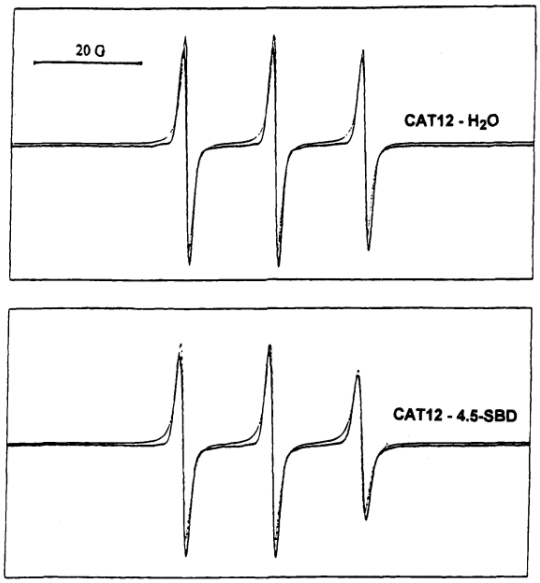

Figure 1.2. Example EPR spectra. Experimental (full lines) and computed (dashed lines) EPR spectra of 4-ammonio-2,2,6,6-tetramethylpiperidine-N-oxyl iodide derivatives (CAT12) in water solution and in solution containing starburst dendrimers (SBDs). Copyright © 1995, American Chemical Society[32]

While analyzing TEMPO, we fortuitously came across the phenomenon of supercooling.

1.1.2 Supercooling

We had melted TEMPO in a vial, and then as it cooled back down to room temperature, it remained a liquid. Supercooling is exactly that; it is when a liquid material drops below its freezing point and remains liquid. Water is a common supercoolable liquid. It is studied in meteorology because supercooled droplets exist in clouds and play a role in the formation of precipitation.[35] The freezing of supercooled water releases latent heat, preventing plants from freezing. Supercooled liquids (SCLs) are also used in rechargeable

heat packs. When a supercooled liquid (SCL) is disturbed inside a heat pouch, a nucleation site occurs, and like in plants, the latent heat creates heat in the heat packs.

1.1.3 Nucleation

Nucleation refers to the initiation of a phase change in a material. For SCLs, it is the single starting point of the solidification process. There are two types of nucleation: homogenous and heterogenous.[36] Homogenous nucleation is spontaneous and happens within the liquid without any foreign surfaces or impurities being present. Heterogeneous nucleation happens when there are surfaces with defects on the container or impurities in the liquid. Comparing the two types, it is much harder for homogeneous nucleation to occur because the SCL needs to overcome a substantial energy barrier, while that is not the case for heterogenous nucleation.[37] SCL TEMPO falls under heterogenous nucleation. SCL TEMPO sublimes within its container, and this causes the appearance of a nucleation site on the container's walls or under the lid. After hours, days, and even sometimes months, crystal growth occurs at the nucleation site which eventually causes SCL TEMPO to fully solidify.

1.1.4 Crystal Growth

Crystal growth is the process by which a seed crystal (nucleation site) becomes larger as molecules add to its crystalline structure. The rate of crystal growth is influenced by multiple factors, which include the presence of impurities, temperature, concentration of particles in the surrounding area, and even agitation. Depending on the application, crystals may be grown for their purity, size, and other properties.[38]

1.1.5 Thermal Properties

To characterize TEMPO's ability to be a SCL, we analyzed its thermal properties using differential scanning calorimetry (DSC). DSC is a thermoanalytical technique that measures the variation in heat needed to raise the temperature of a sample compared to a reference, plotted against temperature.[39] DSC can detect both endothermic processes like melting and exothermic processes like crystallization. For TEMPO, which will be discussed in more detail in chapter 3, it has an exothermic peak for melting, but it does not have any endothermic peaks as it is cooled back down to room temperature, indicating that it remains an SCL.

We prove that mechanical motion is possible by incorporating a stable free radical into a polymer, but we wanted to incorporate light to have controllable photomechanical motion. In the next section, we will discuss our strategy to photomechanically move hexaarylbiimidizole (HABI) doped in PMMA.

1.2 HABI

HABI is a molecule that contains two imidazole rings that are substituted with aryl groups. HABI is yellow as its monomer and then becomes purple free radical dimers as shown in **Figure 1.3** because it is a photochromic molecule, which is explained in section 1.2.1. The molecule is unreactive to the air, commercially available, ready to use right from the manufacturer, and can easily be irradiated to become free radicals, which is why it was chosen for the photochemical approach to this dissertation.

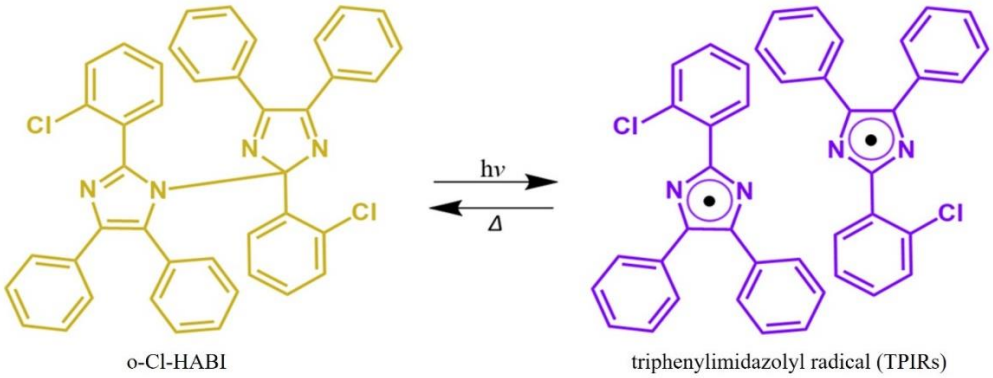

Figure 1.3. HABI molecule. (**Left**) The dimer, o-Cl-HABI and (**Right**) the monomer free radicals.

1.2.1 Photochromism

Photochromism can be described as the reversible alteration of a chemical species induced by light, resulting in a transition between two forms characterized by distinct absorption spectra. Photochromic materials change color upon photoirradiation and are a well-known class of molecules.[14,40–51] Photochromic systems can be divided into two categories based on the thermal stability of the photogenerated species: T-type (thermally reversible) systems, where the photogenerated isomers return to their original forms through thermal processes, and P-type (photochemically reversible) systems, where this reversion to the initial isomers doesn't occur even at elevated temperatures.[42] Typical examples of T-type photochromic compounds include azobenzenes, spiropyrans, and hexaarylbiimidazoles, while stable P-type photochromic compounds include diarylethenes with heterocyclic rings.[41] This dissertation will focus on hexaarylbiimidazoles in chapter 1.2 and chapter 4.

1.2.2 Applications

HABI is a great candidate for efficient photoinitiation techniques[52–54], like coatings that are cured with light, because a single molecule becomes two free radicals. This puts

HABI in an advantage compared to other molecules that only produce a single free radical. The study of HABIs dates back to the 1960s[46], with their discovery bringing to light their peculiar properties. Their photochromic behavior, which causes a change from yellow to purple under UV irradiation, is attributed to the photoinduced cleavage of the C-N bond between imidazole rings. This process forms radicals, specifically a pair of 2,4,5-triphenylimidazolyl radicals. These radicals are stable in oxygen-rich environments and exhibit slow recombination rates.[45] This project utilizes HABI's slow recombination rate for photomechanical motion.

HABI on its own is a fine powder, so we needed a way to embed it a polymer for use in photochemical motion. Similarly to the TEMPO experiments, we decided on polymethyl methacrylate (PMMA) because it is clear, commercially available, and unreactive to the ambient atmosphere.

1.3 Pyrolytic Graphite

Working with HABI gave us the motivation to explore other methods to change χ, which is why we then began working with magnetic levitation (maglev). Pyrolytic graphite is one of the most diamagnetic materials with χ on the order of -1.0×10^{-4},[55] while other materials are on the order of -1.0×10^{-6}.[56] PG's diamagnetic susceptibility is strong enough to utilize its diamagnetism for maglev. As an alternative to HABI to change a material from diamagnetic to paramagnetic, we explored PG because of its strong diamagnetic susceptibility.

1.3.1 Magnetic Levitation

Stable maglev was considered physically impossible from Earnshaw's theorem[57], which states that it is impossible for "a stationary object made out of magnets in a fixed configuration to be held in stable equilibrium by any combination of static magnetic or gravitational forces". However, it was achieved by Braunbek in 1939.[58] Induced magnetism is not affected by Earnshaw's theorem, and it is possible to have a minimum total energy, which is necessary for reaching stable equilibrium. Since then, we have utilized magnetic levitation for different applications such as maglev trains. These maglev trains use electromagnets and superconducting magnets.[59] Electromagnetic levitation relies on a control system[60] to adjust the magnetic current to maintain clearance between the train and railing, and superconducting levitation requires intricate cooling systems for superconducting coils.[61] Diamagnetic levitation, on the other hand, simply requires the balance between the repulsive force of the material with the magnetic field and the force of gravity.[62]

1.3.2 Photothermal Magnetic Levitation

The χ of PG can be changed photothermally. Jiro Abe was one of the leading scientists to perform macroscale displacement of PG photothermally using a 405 nm laser.[63] Abe presents a method to control the motion of magnetically levitating pyrolytic graphite using photoirradiation. The optical movement of the graphite is driven by photothermally induced changes in its magnetic susceptibility. They also demonstrate that light energy can be converted into rotational kinetic energy using the photothermal property of graphite.

In 2022, Huang et. al. created stable magnetic levitation of PG using circular magnetic arrays.[64] In their system as shown in **Figure 1.4**, they used circular magnets embedded in one another with alternating poles to manipulate the magnetic field above the magnets. They also created a method to investigate position stability of PG. The proposed analytical method provides a comprehensive approach to study the position stability of PG disks. It offers insights into the local forces within the disk, which can help in optimizing the shape design of PG disks for better stability. This method is the first of its kind to study the position stability of PG disks and fills a gap in the theoretical model of the mechanism of stable levitation.

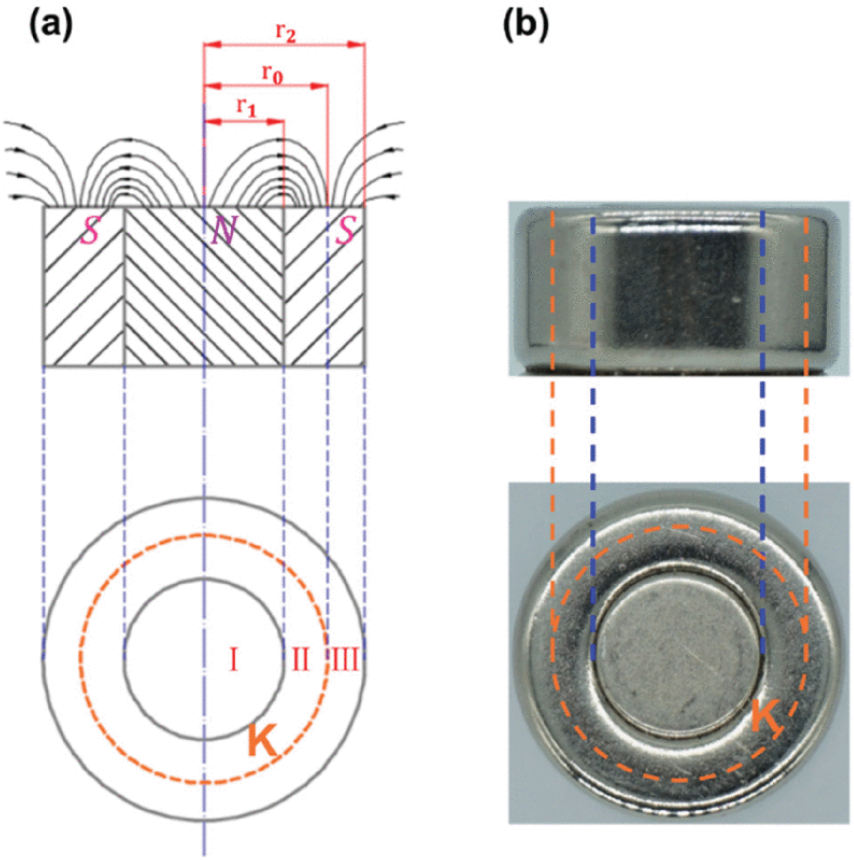

Figure 1.4. Region division of magnetic field generated by circular magnetic array: **(a)** schematics of magnet setup, and **(b)** pictures of the magnets. Copyright 2022 IEEE[66]

Kang et. al. introduced a method for trajectory control of levitated diamagnetic graphite using a unique permanent magnet rail (**Figure 1.5)**.[65] This rail is constructed using a Halbach 1D magnet array combined with non-magnetic spacers. The spacers play a pivotal role in controlling the trajectory by adjusting the magnetic force field. As the magnetic force field weakens due to the spacers, the levitated PG slides towards areas of weaker magnetic force. Additionally, they introduce a photo-gated motion control technique. This method uses a laser beam to create an equilibrium state for the levitated PG disk. When the laser is turned off or moved away from the PG disk, the equilibrium breaks, causing the PG disk to slide due to the magnetic potential gradient force.

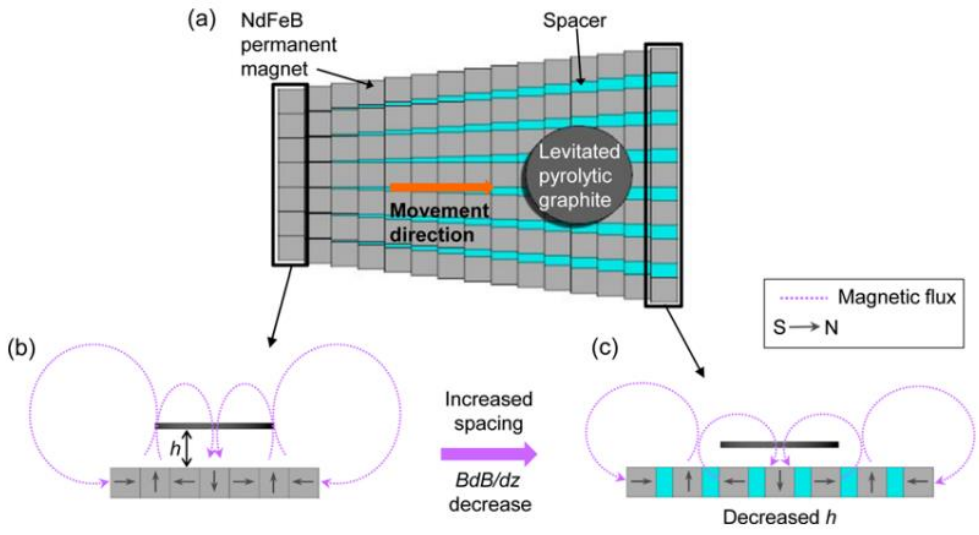

Figure 1.5. Schematic of the permanent magnet rail for trajectory control of diamagnetic substances: (**a**) top view of rail; (**b**) cross-section view of the Halbach 1D magnet array without spacer and its magnetic flux: both sides of the Halbach 1D array have stronger magnetic flux than the center; and (**c**) cross-section view of the magnets with spacers; this array has a weaker *BdB/dz* than an array without spacers superconducting. Copyright © 2018, Korean Society for Precision Engineering[65]

1.4 Photomechanical Motion Using an External Magnetic Field (This Work)

In the pursuit of understanding and harnessing photomechanical motion using an external magnetic field, our exploration started with TEMPO as a preliminary case and

then led us to the realm of photochemical reactions, particularly focusing on HABI. This will be the topic of chapter 4. The objective was to leverage HABI's properties, specifically its magnetic susceptibility, through photoexcitation for controlled photomechanical motion.

In chapter 5, we discuss the concept of using photothermal heating to control the magnetic susceptibility of the graphite plate. By altering the magnetic susceptibility through laser-induced heating, we can tilt a graphite plate that is placed on the surface of a magnet. This novel approach to magnetic levitation could be used in applications like beam steering, where a laser beam’s direction can be controlled.

1.5 References

(1) Hoorens, M. W. H.; Szymanski, W. Reversible, Spatial and Temporal Control over Protein Activity Using Light. *Trends Biochem Sci* **2018**, *43* (8), 567–575. https://doi.org/10.1016/j.tibs.2018.05.004.

(2) Zhu, L.; Al-Kaysi, R. O.; Dillon, R. J.; Tham, F. S.; Bardeen, C. J. Crystal Structures and Photophysical Properties of 9-Anthracene Carboxylic Acid Derivatives for Photomechanical Applications. *Cryst Growth Des* **2011**, *11* (11), 4975–4983. https://doi.org/10.1021/cg200883b.

(3) Weissleder, R.; Nahrendorf, M. Advancing Biomedical Imaging. *Proceedings of the National Academy of Sciences* **2015**, *112* (47), 14424–14428. https://doi.org/10.1073/pnas.1508524112.

(4) Fujimoto, J. G.; Pitris, C.; Boppart, S. A.; Brezinski, M. E. Optical Coherence Tomography: An Emerging Technology for Biomedical Imaging and Optical Biopsy. *Neoplasia* **2000**, *2* (1–2), 9–25. https://doi.org/10.1038/sj.neo.7900071.

(5) Kuniyil Ajith Singh, M.; Steenbergen, W.; Manohar, S. Handheld Probe-Based Dual Mode Ultrasound/Photoacoustics for Biomedical Imaging. In *Frontiers in Biophotonics for Translational Medicine: In the Celebration of Year of Light (2015)*; 2016; pp 209–247. https://doi.org/10.1007/978-981-287-627-0_7.

(6) Schuocker, D. Laser Cutting. *Materials and Manufacturing Processes* **2007**, *4* (3), 311–330. https://doi.org/10.1080/10426918908956297.

(7) Niziev, V. G.; Nesterov, A. V. Influence of Beam Polarization on Laser Cutting Efficiency. *J Phys D Appl Phys* **1999**, *32* (13), 1455–1461. https://doi.org/10.1088/0022-3727/32/13/304.

(8) Martinez, V. M.; Edgar, T. F. Control of Lithography in Semiconductor Manufacturing. *IEEE Control Syst* **2006**, *26* (6), 46–55. https://doi.org/10.1109/MCS.2006.252811.

(9) Zhu, L.; Tong, F.; Al-Kaysi, R. O.; Bardeen, C. J. Photomechanical Effects in Photochromic Crystals. In *Photomechanical Materials, Composites, and Systems*; Wiley, 2017; pp 233–274. https://doi.org/10.1002/9781119123279.ch7.

(10) Tong, F.; Liu, M.; Al-Kaysi, R. O.; Bardeen, C. J. Surfactant-Enhanced Photoisomerization and Photomechanical Response in Molecular Crystal Nanowires. *Langmuir* **2018**, *34* (4), 1627–1634. https://doi.org/10.1021/acs.langmuir.7b03848.

(11) Kitagawa, D.; Tsujioka, H.; Tong, F.; Dong, X.; Bardeen, C. J.; Kobatake, S. Control of Photomechanical Crystal Twisting by Illumination Direction. *J Am Chem Soc* **2018**, *140* (12), 4208–4212. https://doi.org/10.1021/jacs.7b13605.

(12) Uchida, E.; Azumi, R.; Norikane, Y. Light-Induced Crawling of Crystals on a Glass Surface. *Nat Commun* **2015**, *6* (1), 7310. https://doi.org/10.1038/ncomms8310.

(13) Wang, H.; Chen, P.; Wu, Z.; Zhao, J.; Sun, J.; Lu, R. Bending, Curling, Rolling, and Salient Behavior of Molecular Crystals Driven by [2+2] Cycloaddition of a Styrylbenzoxazole Derivative. *Angewandte Chemie International Edition* **2017**, *56* (32), 9463–9467. https://doi.org/10.1002/anie.201705325.

(14) Nath, N. K.; Runčevski, T.; Lai, C.-Y.; Chiesa, M.; Dinnebier, R. E.; Naumov, P. Surface and Bulk Effects in Photochemical Reactions and Photomechanical Effects in Dynamic Molecular Crystals. *J Am Chem Soc* **2015**, *137* (43), 13866–13875. https://doi.org/10.1021/jacs.5b07806.

(15) Krauss, J. M.; Puliafito, C. A. Lasers in Ophthalmology. *Lasers Surg Med* **1995**, *17* (2), 102–159. https://doi.org/https://doi.org/10.1002/lsm.1900170203.

(16) Regar, E.; Schaar, J. A.; Mont, E.; Virmani, R.; Serruys, P. W. Optical Coherence Tomography. *Cardiovasc Radiat Med* **2003**, *4* (4), 198–204. https://doi.org/10.1016/j.carrad.2003.12.003.

(17) Chen, Q.; Lu, H.; Zhang, Z.; Du, B.; Liu, M.; Zhao, G. Visible-Light-Driven Molecularly Imprinted Self-Powered Sensor for Atrazine with High Sensitivity and Selectivity by Separating Photoanode from Recognition Element. *Sens Actuators B Chem* **2022**, *360* (December 2021), 131670. https://doi.org/10.1016/j.snb.2022.131670.

(18) Kim, T.; Zhu, L.; Al-Kaysi, R. O.; Bardeen, C. J. Organic Photomechanical Materials. *ChemPhysChem* **2014**, *15* (3), 400–414. https://doi.org/10.1002/cphc.201300906.

(19) Dasgupta, J.; Frontiera, R. R.; Taylor, K. C.; Lagarias, J. C.; Mathies, R. A. Ultrafast Excited-State Isomerization in Phytochrome Revealed by Femtosecond Stimulated Raman Spectroscopy. *Proceedings of the National Academy of Sciences* **2009**, *106* (6), 1784–1789. https://doi.org/10.1073/pnas.0812056106.

(20) GOODEVE, C. F. Photochemical Reactions in the Gaseous, Liquid and Solid States. *Nature* **1939**, *143* (3633), 1007–1011. https://doi.org/10.1038/1431007a0.

(21) Anderson, B. R.; Kuzyk, M. G. Imaging Studies of Photodegradation and Self-Healing in Anthraquinone Derivative Dye-Doped PMMA. *Physical Chemistry Chemical Physics* **2020**, *22* (48), 28154–28164. https://doi.org/10.1039/D0CP05426G.

(22) Ashkin, A. Acceleration and Trapping of Particles by Radiation Pressure. *Phys Rev Lett* **1970**, *24* (4), 156–159. https://doi.org/10.1103/PhysRevLett.24.156.

(23) Sun, F.; Shasho, R. T.; Crescimanno, M.; Dawson, N. J. All-Optical Method of Determining Laser Power from the Photomechanical Effect. *Applied Sciences* **2022**, *12* (21), 10708. https://doi.org/10.3390/app122110708.

(24) Lewis, G. N.; Calvin, M.; Kasha, M. Photomagnetism. Determination of the Paramagnetic Susceptibility of a Dye in Its Phosphorescent State. *J Chem Phys* **1949**, *17* (9), 804–812. https://doi.org/10.1063/1.1747403.

(25) Mugiraneza, S.; Hallas, A. M. Tutorial: A Beginner's Guide to Interpreting Magnetic Susceptibility Data with the Curie-Weiss Law. *Commun Phys* **2022**, *5* (1), 1–12. https://doi.org/10.1038/s42005-022-00853-y.

(26) Neelakanta, P. S. *Handbook of Electromagnetic Materials : Monolithic and Composite Versions and Their Applications*; CRC Press: Boca Raton, 1995.

(27) Rozantzev, E. G.; Neiman, M. B. Organic Radical Reactions Involving No Free Valence. *Tetrahedron* **1964**, *20* (1), 131–137. https://doi.org/10.1016/S0040-4020(01)98404-2.

(28) Pyror, W. A. Free Radicals in Biological Systems. *Sci Am* **1970**, *223* (2), 70–83.

(29) Adam, W.; Saha-Möller, C. R.; Ganeshpure, P. A. Synthetic Applications of Nonmetal Catalysts for Homogeneous Oxidations. *Chem Rev* **2001**, *101* (11), 3499–3548. https://doi.org/10.1021/cr000019k.

(30) Lucio Anelli, P.; Biffi, C.; Montanari, F.; Quici, S. Fast and Selective Oxidation of Primary Alcohols to Aldehydes or to Carboxylic Acids and of Secondary Alcohols to Ketones Mediated by Oxoammonium Salts under Two-Phase Conditions. *J Org Chem* **1987**, *52* (12), 2559–2562. https://doi.org/10.1021/jo00388a038.

(31) Bowry, V. W.; Ingold, K. U. Kinetics of Nitroxide Radical Trapping. 2. Structural Effects. *J Am Chem Soc* **1992**, *114* (13), 4992–4996. https://doi.org/10.1021/ja00039a006.

(32) Ottaviani, M. F.; Cossu, E.; Turro, N. J.; Tomalia, D. A. Characterization of Starburst Dendrimers by Electron Paramagnetic Resonance. 2. Positively Charged Nitroxide Radicals of Variable Chain Length Used as Spin Probes. *J Am Chem Soc* **1995**, *117* (15), 4387–4398. https://doi.org/10.1021/ja00120a022.

(33) Qu, J.; Morita, R.; Satoh, M.; Wada, J.; Terakura, F.; Mizoguchi, K.; Ogata, N.; Masuda, T. Synthesis and Properties of DNA Complexes Containing 2,2,6,6-Tetramethyl-1-piperidinoxy (TEMPO) Moieties as Organic Radical Battery Materials. *Chemistry – A European Journal* **2008**, *14* (11), 3250–3259. https://doi.org/10.1002/chem.200800021.

(34) Iwamoto, T.; Masuda, H.; Ishida, S.; Kabuto, C.; Kira, M. Addition of Stable Nitroxide Radical to Stable Divalent Compounds of Heavier Group 14 Elements. *J Am Chem Soc* **2003**, *125* (31), 9300–9301. https://doi.org/10.1021/ja0356784.

(35) Murphy, D. M.; Koop, T. Review of the Vapour Pressures of Ice and Supercooled Water for Atmospheric Applications. *Quarterly Journal of the Royal Meteorological Society* **2005**, *131* (608), 1539–1565. https://doi.org/10.1256/qj.04.94.

(36) Ediger, M. D.; Angell, C. A.; Nagel, S. R. Supercooled Liquids and Glasses. *J Phys Chem* **1996**, *100* (31), 13200–13212. https://doi.org/10.1021/jp953538d.

(37) Turnbull, D. Under What Conditions Can A Glass Be Formed? *Contemp Phys* **1969**, *10* (5), 473–488. https://doi.org/10.1080/00107516908204405.

(38) Levi, A. C.; Kotrla, M. Theory and Simulation of Crystal Growth. *Journal of Physics: Condensed Matter* **1997**, *9* (2), 299–344. https://doi.org/10.1088/0953-8984/9/2/001.

(39) Menczel, J. D.; Judovits, L.; Prime, R. B.; Bair, H. E.; Reading, M.; Swier, S. Differential Scanning Calorimetry (DSC). In *Thermal Analysis of Polymers*; 2009; pp 7–239. https://doi.org/https://doi.org/10.1002/9780470423837.ch2.

(40) Kishimoto, Y.; Abe, J. A Fast Photochromic Molecule That Colors Only under UV Light. *J Am Chem Soc* **2009**, *131* (12), 4227–4229. https://doi.org/10.1021/ja810032t.

(41) Ooyama, Y.; Yagi, S. *Progress in the Science of Functional Dyes*; Ooyama, Y., Yagi, S., Eds.; Springer Singapore: Singapore, 2021. https://doi.org/10.1007/978-981-33-4392-4.

(42) Abe, J.; Yamashita, H.; Mutoh, K. Photochromism. In *Encyclopedia of Polymeric Nanomaterials*; Springer Berlin Heidelberg: Berlin, Heidelberg, 2015; pp 1572–1579. https://doi.org/10.1007/978-3-642-29648-2_119.

(43) Irie, M. Photochromism: Memories and SwitchesIntroduction. *Chem Rev* **2000**, *100* (5), 1683–1684. https://doi.org/10.1021/cr980068l.

(44) Maeda, K.; Hayashi, T. The Mechanism of Photochromism, Thermochromism and Piezochromism of Dimers of Triarylimidazolyl. *Bulletin of the Chemical Society of Japan*. 1970, pp 429–438. https://doi.org/10.1246/bcsj.43.429.

(45) Bagheri, M.; Mirzaee, M.; Hosseini, S.; Gholamzadeh, P. The Photochromic Switchable Imidazoles: Their Genesis, Development, Synthesis, and Characterization. *Dyes and Pigments* **2022**, *203* (April), 110322. https://doi.org/10.1016/j.dyepig.2022.110322.

(46) Maeda, K.; Hayashi, T. Photochromic Color Change of the Dimer of Triphenylimidazolyl at Low Temperatures. *Bull Chem Soc Jpn* **1969**, *42* (12), 3509–3514. https://doi.org/10.1246/bcsj.42.3509.

(47) Irie, M.; Fukaminato, T.; Matsuda, K.; Kobatake, S. Photochromism of Diarylethene Molecules and Crystals: Memories, Switches, and Actuators. *Chem Rev* **2014**, *114* (24), 12174–12277. https://doi.org/10.1021/cr500249p.

(48) Ito, H.; Tanaka, S.; Mutoh, K.; Abe, J. Fast Photochromism of the Imidazole Dimers Bridged by Group 14 Atoms. *Org Lett* **2020**, *22* (14), 5680–5684. https://doi.org/10.1021/acs.orglett.0c02072.

(49) Fujita, K.; Hatano, S.; Kato, D.; Abe, J. Photochromism of a Radical Diffusion-Inhibited Hexaarylbiimidazole Derivative with Intense Coloration and Fast Decoloration Performance. *Org Lett* **2008**, *10* (14), 3105–3108. https://doi.org/10.1021/ol801135g.

(50) Kataoka, K.; Kobayashi, T.; Arai, T. *Photochromism of Organic Compounds Undergoing Isomerization Around the C═C Double Bond and/or Intramolecular Hydrogen Atom Transfer: Small and Large Structural Change*; 2013. https://doi.org/10.1007/978-4-431-54291-9_13.

(51) Lvov, A. G.; Khusniyarov, M. M.; Shirinian, V. Z. Azole-Based Diarylethenes as the next Step towards Advanced Photochromic Materials. *Journal of Photochemistry and Photobiology C: Photochemistry Reviews* **2018**, *36*, 1–23. https://doi.org/10.1016/j.jphotochemrev.2018.04.002.

(52) Ahn, D.; Sathe, S. S.; Clarkson, B. H.; Scott, T. F. Hexaarylbiimidazoles as Visible Light Thiol–Ene Photoinitiators. *Dental Materials* **2015**, *31* (9), 1075–1089. https://doi.org/10.1016/j.dental.2015.06.005.

(53) Chen, Y.-C.; Kuo, Y.-T.; Ho, T.-H. Photo-Polymerization Properties of Type-II Photoinitiator Systems Based on 2-Chlorohexaaryl Biimidazole (o-Cl-HABI) and Various N-Phenylglycine (NPG) Derivatives! *Photochemical & Photobiological Sciences* **2019**, *18* (1), 190–197. https://doi.org/10.1039/c8pp00300a.

(54) Sun, Y.; Weng, Y.; Chen, G.; Zhang, W. Switchable RAFT Polymerization Employing Photoresponsive HABI as a Mediator. *Macromol Rapid Commun* **2023**, *44* (3), 1–6. https://doi.org/10.1002/marc.202200664.

(55) Magnetic and Other Properties of the Free Electrons in Graphite. *Proc R Soc Lond A Math Phys Sci* **1941**, *177* (969), 168–182. https://doi.org/10.1098/rspa.1941.0002.

(56) G. P. ARRIGHINI, M. MAESTRO, A. R. M. Magnetic Properties of Polyatomic Molecules. I. Magnetic Susceptibility of H2O, NH3, CH4, H2O2. *J. Phys. Chem* **1968**, *49* (2), 882–889. https://doi.org/https://doi.org/10.1063/1.1670155.

(57) S. Earnshaw. On the Nature of the Molecular Forces Which Regulate the Constitution of the Luminiferous Ether. *Trans. Cambridge Philos. Soc.* **1842**, *7*, 97–112.

(58) Braunbek, W. Die Erzeugung Weitgehend Homogener Magnetfelder Durch Kreisströme. *Zeitschrift für Physik* **1934**, *88* (5–6), 399–402. https://doi.org/10.1007/BF01343500.

(59) Ono, M.; Koga, S.; Ohtsuki, H. Japan's Superconducting Maglev Train. *IEEE Instrum Meas Mag* **2002**, *5* (1), 9–15. https://doi.org/10.1109/5289.988732.

(60) Vigoureux, P. Electromagnetic Levitation Forces. *British Journal of Applied Physics* **1965**, *16* (5), 757–757. https://doi.org/10.1088/0508-3443/16/5/135.

(61) Ma, K. B.; Postrekhin, Y. V.; Chu, W. K. Superconductor and Magnet Levitation Devices. *Review of Scientific Instruments* **2003**, *74* (12), 4989–5017. https://doi.org/10.1063/1.1622973.

(62) Waldron, R. D. Diamagnetic Levitation Using Pyrolytic Graphite. *Review of Scientific Instruments* **1966**, *37* (1), 29–35. https://doi.org/10.1063/1.1719946.

(63) Kobayashi, M.; Abe, J. Optical Motion Control of Maglev Graphite. *J Am Chem Soc* **2012**, *134* (51), 20593–20596. https://doi.org/10.1021/ja310365k.

(64) Huang, J.; Zhao, P.; Zhang, C.; Xie, J.; Xia, N.; Fu, J. Stable Levitation of Pyrolytic Graphite Above Circular Magnet Arrays. *IEEE Trans Magn* **2022**, *58* (8), 1–11. https://doi.org/10.1109/TMAG.2022.3182214.

(65) Kang, S.; Kim, J.; Pyo, J.-B.; Cho, J. H.; Kim, T.-S. Design of Magnetic Force Field for Trajectory Control of Levitated Diamagnetic Graphite. *International Journal of Precision Engineering and Manufacturing-Green Technology* **2018**, *5* (2), 341–347. https://doi.org/10.1007/s40684-018-0036-3.

(66) Huang, J.; Zhao, P.; Zhang, C.; Xie, J.; Xia, N.; Fu, J. Stable Levitation of Pyrolytic Graphite Above Circular Magnet Arrays. *IEEE Trans Magn* **2022**, *58* (8), 1–11. https://doi.org/10.1109/TMAG.2022.3182214.

Chapter 2. Experimental Methods

This chapter is divided into three parts that correlate with the three projects worked on during my PhD.

2.1 Supercooled TEMPO

2.1.1 Sample Preparation

2,2,6,6-tetramethyl-1-piperidine-1-oxyl (TEMPO, Sigma-Aldrich, 98% purity) and 4-hydroxy-2,2,6,6-tetramethyl-1-piperidine-1-oxyl (TEMPOL, Tokyo Chemical Industry) were used as received. To prepare a typical SCL sample, 1.2 ± 0.20 g of TEMPO was loaded into a 20 mL glass scintillation vial with a polyethylene-lined screw cap (VWR, part number 66022-128). Lower mass samples could also be prepared in 2 mL autosampler vials (Fisher, part number 03-391-8), NMR tubes, plastic vials, and 1 mm diameter capillary tubing. The glass containers were either used as received or cleaned using different solvents (acetone, MeOH, and HCl). Glass vials were also cleaned by soaking them in room temperature Piranha solution (a 3:1 v/v mixture of concentrated sulfuric acid and 30% hydrogen peroxide) for 40 minutes. Thermal melting was achieved in a Barnstead Thermolyne 1400 furnace set to 41°C, and samples were immediately removed from the oven and allowed to cool undisturbed on a benchtop to reach room temperature.

2.1.2 UV-Visible Spectroscopy (UV-Vis)

All UV-Vis measurements were performed using a Cary 60 UV-Vis Spectrophotometer. TEMPO solutions in chloroform were analyzed in a 1 cm path length quartz cuvette, while the TEMPO SCL absorption was measured using a 1 mm path length quartz cuvette. For solid TEMPO measurements, a few drops of liquid TEMPO were cast

onto a microscope slide (Eisco 1” x 3”, 1.1 mm thick) under a coverslip (Fisherbrand Microscope Cover Glass 25 x 25 mm). Solidification was induced by gently tapping the slide after cooling to room temperature.

2.1.3 Electron Paramagnetic Resonance (EPR)

EPR measurements were conducted using a Bruker Magnettech ESR5000. Samples were run with a center field of 338 mT, sweep width of 50 mT, modulation of 0.2, frequency of 100 KHz, and a power of 10.0 mW.

2.1.4 Differential Scanning Calorimetry (DSC)

DSC scans were performed using a Netzsch 214 Polyma differential scanning calorimeter. Measurements were done with variable heating and cooling rates, ranging from 0.2-5.0 °C min^{-1}, over a total range of 5-60 °C. After melting and cooling, the samples were held at 20 °C for 30 minutes to confirm that no solidification occurred in the metal sample holder.

2.1.5 Optical Melting and Solidification

Optical melting was achieved by exposing 200 mg of solid TEMPO to a 532 nm continuous wave (cw) laser for 5 minutes at a power of 2 W. After the sample melted, supercooling was confirmed by observing the liquid for up to 1 hour at room temperature. Solidification of the SCL was triggered by a single 532 nm pulse, with an energy of 270 mJ and a duration of 10 ns, generated using a Continuum Surelight SLII-10 laser.

2.1.6 Powder X-Ray Diffraction (PXRD)

TEMPO was crushed into a fine powder using a mortar and pestle. PXRD was performed using a Panalytical Empyrean Series 2 diffractometer with CuKα radiation (λ =

1.5418 Å, 45 kV/40 mA power). The following slit sizes were used: incident divergence (1/2º), incident anti-scatter (1º), and diffracted anti-scatter (P8.0). The sample stage was set to spin with a revolution time of 2 seconds and step size of 0.0131 degrees.

2.1.7 Polarized Optical Microscopy

A few drops of liquid TEMPO were cast onto a microscope slide (Eisco 1" x 3", 1.1 mm thick) under a coverslip (Fisherbrand Microscope Cover Glass 25 x 25 mm). The sample was allowed to cool to room temperature before capturing unpolarized and polarized images using a Leica MC120 HD 2.5 Megapixel Microscope Camera. Solidification of SCL TEMPO was induced by gently tapping the microscope slide, and images of the solid sample were subsequently acquired.

2.1.8 Viscosity Measurements

To assess the viscosity of SCL TEMPO in comparison to melted TEMPO, a 3.18 mm OD ball bearing was dropped into a 17.78 mm long NMR tube filled with TEMPO. Videos were recorded at 60 frames per second (0.016 second accuracy) using a Google Pixel 6 phone. For liquid TEMPO, NMR tubes were heated to 45 °C, followed by immediate use. In the case of SCL TEMPO, the filled tubes were heated to 45 °C and allowed to cool before performing the experiment. Water (viscosity = 0.89 cP at 25°C) was used as a standard.

2.2 HABI

2.2.1 Sample Preparation

HABI/PMMA Solution: Ortho-chloro-hexaarylbiimidazole (HABI), dichloromethane (DCM), polymethyl methacrylate (PMMA), and polyvinyl alcohol (PVA) were all used by

the manufacturer without any modifications. To make a HABI in PMMA film, we first start off with making 1:1 HABI to PMMA solution. 5.0 g of DCM is dispensed using a glass pipette in a 20 mL scintillation vial, 0.5 g of HABI and 0.5 g of PMMA were weighed in corresponding weigh boats. A stir bar was placed in the vial and then put on a stir plate at 700 rpm. PMMA is gradually added into the vial. Once the solution becomes viscous, the stir plate is raised to 1000 rpm. After all the PMMA is dissolved, the HABI is gradually dispensed into the vial and should dissolve almost immediately. The solution is stirred for another 5 minutes after HABI is dissolved.

Substrate: PVA coated glass slides are used as the film substrate. The glass slides themselves cannot be used as a substrate because HABI/PMMA films cannot de-adhere from glass. The PVA is water soluble, so the PVA substrate is dissolved to remove the HABI/PMMA films. First, cut 3" glass slides into three parts. Clean slides with acetone. Place the slides into a petri dish. Using a pre-made 4 % PVA/water solution, coat the glass slides with two drops of the solution using a plastic pipette. The entire glass slides are coated by using the tip of the plastic pipette to spread the PVA solution. Let the solution dry on the glass slides overnight. The substrates are then ready to be used.

HABI/PMMA Film: Use a glass pipette to dispense the HABI/PMMA solution onto the dried PVA substrates. A single drop is used for small, round films, and multiple drops are used for larger films. Film sizes vary depending on the experiment. Immediately cover the petri dish with a second petri dish. If the films are left out in the open air, the films will dry heterogeneously, causing haziness in the films. The second petri dish allows for a DCM

atmosphere, allowing for homogeneous drying. Let films dry over night to ensure complete drying.

De-adhesion of PMMA Films: Once the HABI/PMMA films are completely dry, the PVA on the glass slides needs to be dissolved for proper film de-adhesion. Remove the second petri dish, and then fill the first petri dish with Millipore water until films are fully submerged. Add a small stir bar, place the petri dish on a stir plate at 300, cover with aluminum foil, and then stir at 300 rpm for about 15 minutes. Remove the de-adhered films using a small spatula, and then let dry on a Kimwipe. Films are kept in a closed cardboard box until used for experiments.

HABI solution: A 1 mM solution of HABI in toluene was used for experiments.

2.2.2 Spectroscopic Characterization

UV-Vis: Liquid samples were placed in a clean 1 cm UV-grade fused-silica cuvette and measured at room temperature. An Agilent Cary 60 was used for the measurements, with a setting of 0.5 nm intervals and an integration time of 0.0125 seconds. Solid samples were measured using an Ocean Optics USB4000 using a 50 ms integration time, two scans to average, and a boxcar width of one.

EPR: A Bruker EMX EPR was used to examine the EPR spectra of HABI films and HABI solutions. A generic 405 nm 500 mW CW laser was used to irradiate samples. For films, EPR measurements were taken for 24 hours. For solutions, measurements were taken for 25 minutes.

2.2.3 Experimental Setup

HABI films were placed in a petri dish with water to analyze the movement near a strong magnetic field (**Figure 2.1**). To overcome the fact that HABI thin films have a weak magnetic susceptibility, we used Millipore water as a surface contact to minimize friction.

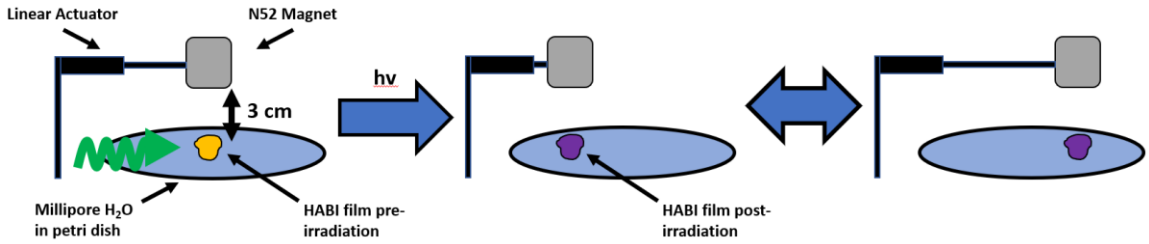

Figure 2.1. Schematic of HABI experiment

With the sample floating in a petri dish, a magnet with 8000 G at its poles was 3 cm from the sample. Before irradiation, there was no reaction between the HABI film and the magnet hanging above it. After irradiation, the sample was attracted to the high field of the magnet, and the sample would follow the high field as the magnet actuates back and forth. As shown in Fig. 5, we were able to move the sample with ease on the surface of the water. Over time, the rate which it took for the sample to move from one position to another decreased. We ran into an unexpected phenomenon during one of the experiments; even without irradiation, the sample would react with the magnetic field if the magnet were close enough to it. As per Geim, if a magnetic field is strong enough, there could be a noticeable repulsive force even with diamagnetic materials that have very low χ[10].[1] We tried other materials such as plain PMMA films, aluminum foil, a small piece of wood, and everything reacted to the magnetic field. Once the magnet was 3 cm from the HABI films, the diamagnetism was too weak for the sample to move without any irradiation. With that

distance, we were able to continue our experiment to demonstrate the change in magnetic susceptibility of our HABI film samples.

2.3 Pyrolytic Graphite (PG)

2.3.1 Sample Preparation

Pyrolytic graphite (PG) was purchased by K&J Magnetics. Highly oriented pyrolytic graphite was purchased from Structure Probe, Inc. Graphite plates were created by milling as-received graphite pieces to dimensions of 5×5×0.83 mm. Fisherbrand 22x22 mm microscope cover slips with a thickness of 0.18 ± 0.02 mm were cut to the same area using a diamond saw and then glued to one side of the graphite plates using Gorilla clear epoxy (part number 42001). These glass surfaces provided a specular reflection that could be used to monitor changes in the reflection angle. The total mass of these samples was 54.6±0.1 mg.

2.3.2 Experimental Setup

A 3” diameter, 1.5” thick cylinder N52 neodymium iron boron magnet (DZ0X8) was purchased from K&J Magnetics. The maximum surface field of the magnet was measured to be 5000 +/- 200 G. To ensure that the magnet stayed safely attached to the laser table, a custom aluminum stand was built to hold it. A 2 W 532 nm CW laser was used to heat the PG samples, and neutral density filters were used to modify the laser power. A 633 nm continuous wave HeNe laser was used as a probe laser whose reflection from the PG sample allowed us to obtain the tilt angle (θ) with respect to the magnet surface. A Google Pixel 3 camera was used to take images and record videos of the PG motion and the probe beam displacement. Magnetic field strengths were measured with an Alpha Lab

Inc. Gaussmeter model GM-1-ST. Temperature measurements were taken with an HTI HT-18 Thermal Imager.

2.3.3 Tilt Angle Measurement

When the PG was exposed to the 532 nm laser, there was a tilt angle change ($\Delta\theta$) that took place over several seconds until a new stationary angle was reached. This angle change generated a displacement of the probe beam spot on a distant surface. We were able to quantify θ using Equations (2.1)-(2.2) and the geometry from **Figure 2.2**. The horizontal probe beam made an angle ϕ with the surface normal of the tilted PG plate.

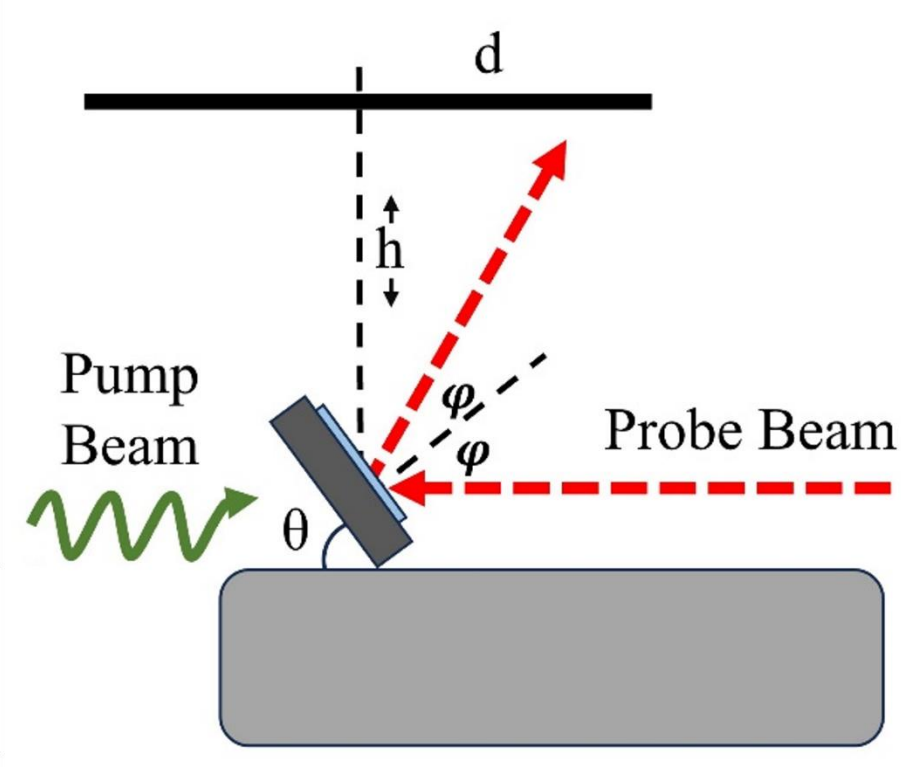

Figure 2.2. Schematic of tilt angle (θ) changes.

ϕ can be related to the probe spot displacement d with respect to the fixed height h of the surface above the magnet using the trigonometric relation:

$$tan(90° - 2\varphi) = d/h \quad (2.1)$$

Once ϕ is found, the tilt angle θ is given by

$$\theta = 90° - \varphi \quad (2.2)$$

Given *h*=79.5 cm and a millimeter resolution in the *d* measurement, this optical lever set-up allowed us to detect θ with an accuracy of 0.1°.

2.3.4 COMSOL Simulation Settings

The magnetic levitation force was calculated based on finite element method using the commercial software, COMSOL Multiphysics. The built-in material sintered NdFeB (N54, remanent flux density norm of 1.48 T) was assigned to the cylindrical magnet with a radius of 3.81 cm and a height of 3.81 cm. The graphite plate (5 mm×5 mm×0.83 mm) with an isotropic magnetic susceptibility of -6.1×10^{-4} was placed on top of the magnet at a position 3.5 cm away from the magnet center with varying tilt angles. An infinite element domain enclosing the whole structure was chosen as the boundary condition. Volumetric force integration was applied to the graphite plate to calculate the magnetic levitation force exerted on it.

2.4 References

(1) Simon, M. D.; Geim, A. K. Diamagnetic Levitation: Flying Frogs and Floating Magnets (Invited). *J Appl Phys* **2000**, *87* (9 III), 6200–6204. https://doi.org/10.1063/1.372654.

Chapter 3. TEMPO Supercooling

3.1 Introduction

Solid glasses[1] and crystals[2, 3] composed of small organic molecules have attracted attention as functional materials. Recently, molecular liquids have begun to receive interest as functional materials as well.[4-6] There are two ways in which a molecule can exist in the liquid phase at room temperature. First, it can exist as a thermodynamically stable liquid with its melting temperature T_m<25°C. Alternatively, it can exist as a supercooled liquid (SCL) when its T_m>25°C. Supercooling occurs when a liquid is cooled below its T_m but is unable to reach the thermodynamic minimum solid-state due to kinetic barriers.[7, 8] This metastable liquid can undergo sudden crystallization when a perturbation is applied. The liquid-to-solid transformation usually involves dramatic changes in optical properties (scattering, luminescence output) as well as physical properties like viscosity and compressibility. Although supercooling can complicate the search for thermodynamically stable functional molecular liquids[9] and on-demand energy release from heat storage media[10, 11], it also presents opportunities to create new types of stimuli-responsive functional materials. Examples include mechanically-induced crystallization of an SCL that can be used for rewritable inks[12-15], as well as phase change materials that store heat that can be released when solidification is induced.[16] The ability of SCLs to undergo solidification when exposed to a specific stimulus is the key to their utility. Ideally, an SCL should be kinetically stable in the absence of this stimulus so it can be stored indefinitely until solidification is desired.

While studying the magnetic properties of the stable free radical 2,2,6,6-tetramethyl-1-piperidine-1-oxyl (TEMPO) (structure shown in **Scheme 3.1**, melting point T_m=38°), we found that it remained liquid after cooling back down to room temperature.

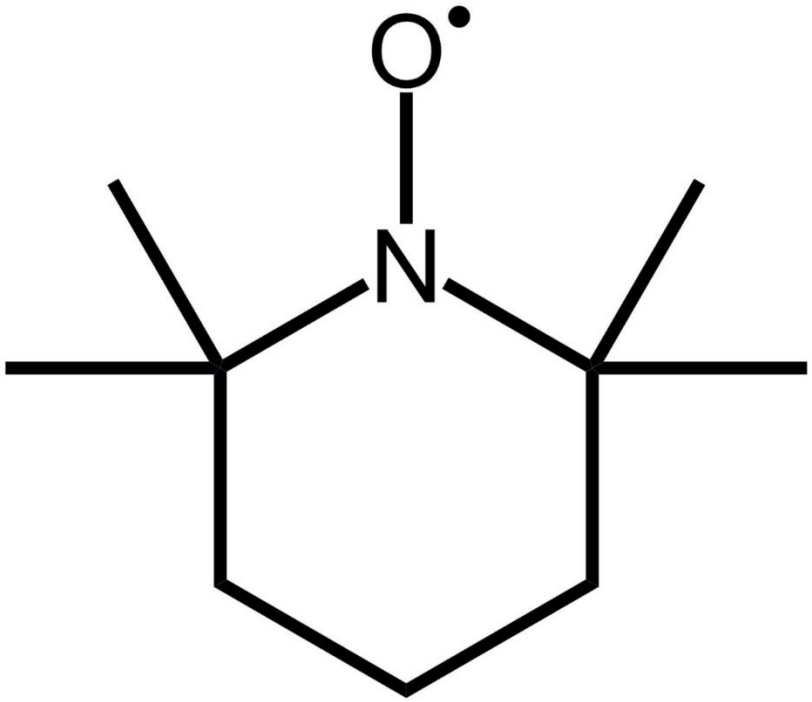

Scheme 3.1. Chemical structure of 2,2,6,6-tetramethyl-1-piperidinyloxy (TEMPO)

We were surprised that this commonly used, commercially available molecule could persist as a stable SCL over months, comparable to the best reported lifetimes of synthetic organic SCLs.[17, 18] Spectroscopic studies revealed no indication of significant differences between TEMPO molecules isolated in solution and those in the neat solid and liquid phases. The radical nature of TEMPO gives rise to an absorption feature that extends out past 600 nm. We took advantage of this absorption to demonstrate laser induced melting to form the SCL followed by impulsive laser heating to induce crystallization. There have been multiple demonstrations of optical control of solid→liquid phase transitions (melting)[19-26]

as well as liquid→solid transitions.[27, 28] The results in this chapter demonstrate that the optical control of an SCL solid→liquid→solid phase change sequence is also possible. Furthermore, spin active liquids like the TEMPO SCL are fundamentally interesting from a materials standpoint.[29] The physical origin of TEMPO's remarkable stability as an SCL remains an open question, but our results suggest that small molecule free radicals may be worth considering as a design motif for this class of materials.

3.2 Results and Discussion

When the heating curve of TEMPO was measured in a differential scanning calorimetry (DSC) experiment, a pronounced endothermic peak at 38°C was observed, corresponding to the reported melting transition (**Figure 3.1**). DSC is a thermoanalytical technique that measures the amount of energy absorbed or released by a sample as it is heated, cooled, or held at a constant temperature. Integration of this peak allowed us to calculate an enthalpy of fusion of 13.8 ± 0.4 kJ/mol (88.3 ± 2.5 kJ/kg). This value is

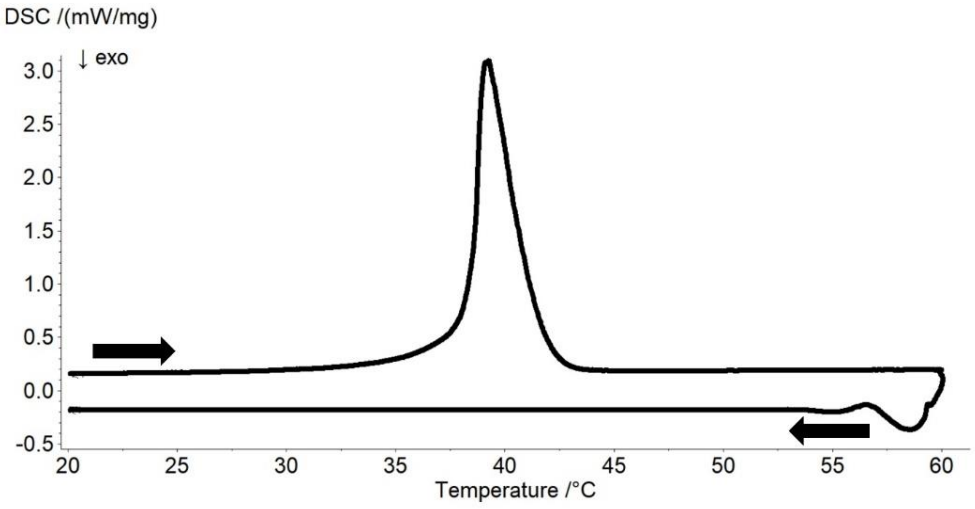

Figure 3.1. DSC thermogram for TEMPO with a heating/cooling rate of 5 °C min^{-1} illustrating an endothermic melting peak at 38°C upon heating but no exothermic peak upon cooling, which is an indication of supercooling behavior.

comparable to that of benzene[30] but well below that of typical phase change materials used for thermal storage.[31] After the temperature ramp was reversed and the sample was cooled, no corresponding exothermic peak due to re-solidification was observed in the DSC curve. Varying the heating and cooling rates from 0.2-5.0 °C min^{-1} had no effect on the shape of the DSC curves (**Supporting Information, Figure S3.1**). Subsequent heating of the SCL did not lead to crystallization, suggesting that the TEMPO SCL was relatively stable to temperature perturbations.

The DSC results were confirmed by visible inspection of TEMPO samples that were melted in an oven and then cooled back to room temperature. The presence of the liquid phase could be easily determined by eye, since crystallization of the SCL led to a large increase in the sample's light scattering. Polarized light microscopy gave no indication of any residual birefringence in the SCL (**Supporting Information, Figure S3.2**). PXRD measurements showed sharp peaks from the solid that could be assigned to orthorhombic and monoclinic polymorphs, but the SCL exhibited only a single very broad peak at $2\theta=15.3°$ (**Supporting Information, Figures S3.3-S3.5**). The broad peak is characteristic of organic molecular liquids and reflects the nearest neighbor scattering in the liquid.[32-34] No sharp peaks were observed that would indicate the presence of a partially ordered or liquid crystal phase. Using the falling ball method and water as a standard, we measured the viscosity of the SCL to be 1.2 cP at 25°C. This value was approximately 10% greater than the value measured for the melt at 44°C. The increased viscosity of the room temperature SCL is consistent with the expected change in liquid viscosity due to the lower temperature, which is in the range for a structurally similar liquid like methylcyclohexane

(Supporting Information).[35] None of these measurements provided evidence for significant structural differences between the SCL and the pure liquid in a high temperature melt. It is possible, however, that more sophisticated rheology measurements could provide evidence for the existence of cooperative regions or longer relaxation times in the SCL.[36]

Supercooling was observed for TEMPO as received (reported as 98% pure) and for TEMPO purified by sublimation, suggesting that the supercooling was not an artifact of chemical impurities. Furthermore, SCL formation was observed in a wide variety of glass containers, including 20 mL vials, NMR tubes, and 1 mm diameter glass capillaries. Within a set of 20 mL vials containing ~1 g of TEMPO, the longevity of the SCL depended on which vial was used. Some vials would only support the SCL for a few hours, while others could maintain the SCL for weeks or months. If one of these long-lived vials was emptied and re-filled with fresh TEMPO, the long-lived SCL was still observed, whereas a short-lived vial was never observed to support a long-lived SCL. We suspected this variation might be due to chemical impurities or solid residue inside the vial. But the use of various cleaning protocols, ranging from acetone rinsing to Piranha acid cleaning, had no measurable effect on the ability of a specific vial to support a long-lived SCL. Based on these observations, we hypothesize that the solidification of the SCL in a stationary container is induced by the presence of microscale structural defects on the container walls, rather than by chemical impurities or intrinsic nucleation events within the melt itself.

Some TEMPO SCL samples persisted for up to 6 months with no sign of crystallization, even after swirling or gentle shaking (**Figure 3.2**). In order to check whether these samples could still crystallize, we used two methods. First, if the cap was

removed and the vial left open to the air for several minutes, solidification typically occurred within 10 min. We suspect that the impact of microscopic dust particles from the ambient air induced crystallization. If the SCL was vented through a small opening that prevented dust entry, it would survive for hours while slowly evaporating. The second method involved direct mechanical perturbation by dipping a pipette tip into the SCL and withdrawing some liquid, which induced crystallization within a few. Note that simply contacting the SCL with a clean pipette tip was not sufficient to induce immediate crystallization. A full characterization of the mechanical conditions under which crystallization can be induced would be desirable but is left for future work.

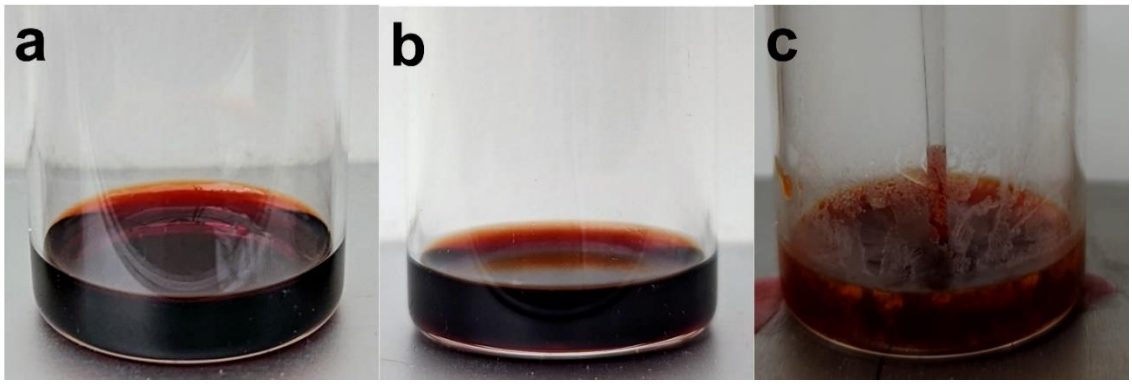

Figure 3.2. Observation of a TEMPO SCL sample at the following time points: **(a)** immediately after removal from oven, **(b)** after 5 months sitting undisturbed, and **(c)** after nucleation is induced by insertion of a glass pipette tip.

For the long-lived (>1 week) samples, the most common mode of crystallization in a closed vial involved growth of a seed crystal separated from the liquid. Over the course of days, a TEMPO crystal would nucleate and grow on the walls or cap of the vial. As the crystal extended from the nucleation point, sometimes up to several centimeters in length, parts of it could break off and drop into the SCL. These fragments acted as seed crystals

for solidification. In some cases, the crystal would actually grow all the way down to the SCL to seed crystallization (**Figure 3.3**). The stability of the TEMPO SCL, combined with

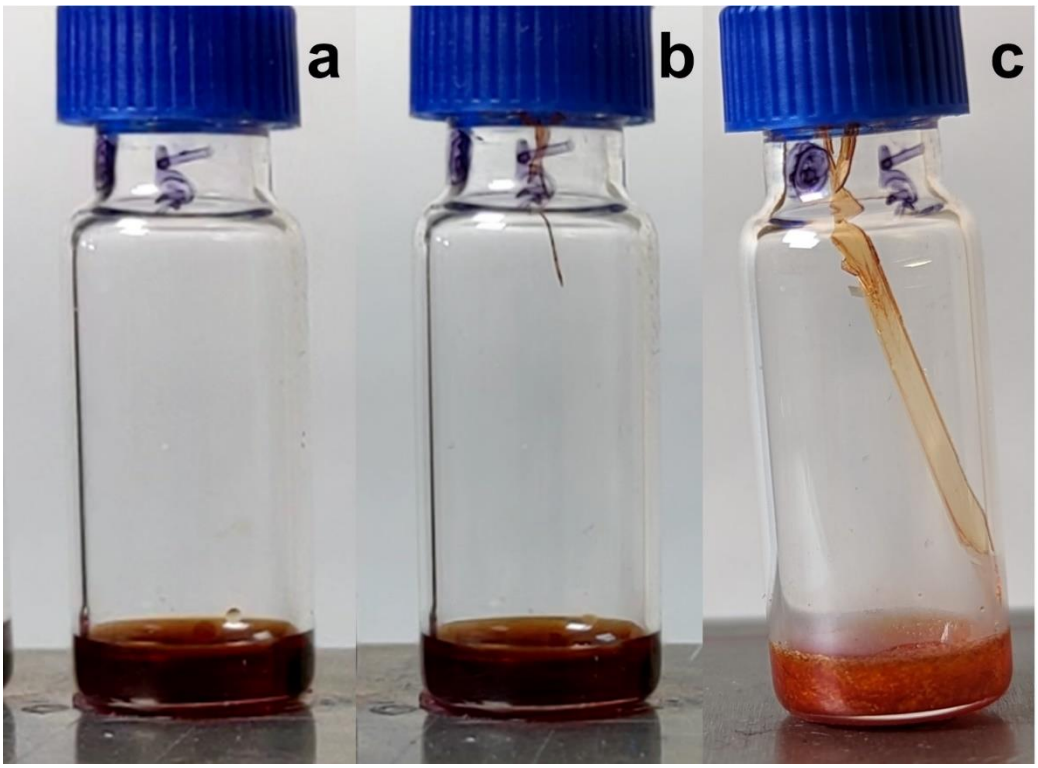

Figure 3.3. Remote crystal growth from a TEMPO SCL observed at different time intervals: (**a**) SCL after 1 hour, (**b**) SCL after 12 days with incipient crystal needle growing from top, and (**c**) after 16 days the crystal needle reaches the SCL and induces crystallization.

its higher vapor pressure, enabled crystal growth via evaporation of the SCL and recondensation of the vapor as a solid at a distant location within the container. This type of secondary crystal growth was never observed for a solid TEMPO sample held under the same conditions (**Supporting Information, Figure S3.6**). Sublimation from the solid was apparently negligible over the same time frame. This observation is consistent with previous studies on water[37] and organic molecules[38] that have shown the SCLs have significantly higher vapor pressures than their solids. New crystal growth could be initiated at a specific location within a few hours by placing a small amount of solid TEMPO in a

capillary in the desired location above the SCL, although the resulting crystal needles typically grew in random directions from the seed (**Supporting Information, Figure S3.7**). These observations show that the TEMPO SCL can be used as a reservoir to supply molecules for crystal growth at a remote location in a sealed system.

To actively induce crystallization of the SCL in a closed system, we utilized the visible absorption of the nitroxide radical that provides a way to heat the sample using light instead. We previously used TEMPO as a photothermal agent for wax melting[39], but in this work we used a 532 nm laser to melt solid TEMPO itself. **Figure 3.4** shows a 100 mg mass of TEMPO being melted by a cw 532 nm laser beam. Using 2 W of laser power, the TEMPO melted completely within 2 minutes. The laser melted TEMPO persisted as an SCL for at least one hour after the laser was turned off. As observed for thermal heating in an oven, solidification could not be induced using the cw laser to slowly reheat the SCL.

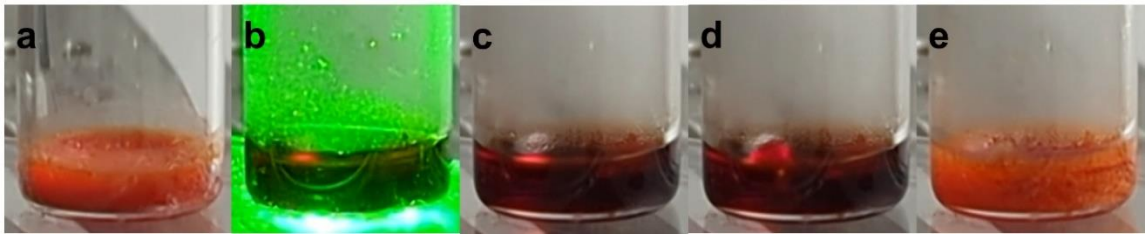

Figure 3.4. Optically induced melting of TEMPO and solidification of SCL TEMPO in a 2 mL glass vial: **(a)** initial solid state, **(b)** melting process using a 2W cw 532 nm laser, **(c)** stable SCL formed after laser melting, (**d**) impact of the single nanosecond 532 nm laser pulse laser indicated by the splash mark formed towards the left of the vial, and **(e)** solid TEMPO formed after the single nanosecond pulse impacts the SCL.

In order to trigger crystallization, we used a pulsed 532 nm laser to impulsively heat the sample. A single 10 ns, 270 mJ laser pulse could vaporize part of the liquid, and the resultant bursting gas bubble provided enough mechanical perturbation to trigger solidification, which occurred within 200 ms of laser impact (**Figure 3.4**). We suspected

that the laser melting might have been incomplete, leaving some residual crystals on the sides of the vial that could act as seeds when the laser pulse perturbed the SCL. To eliminate this possibility, we confirmed that the same laser pulse could also trigger recrystallization of an SCL generated by oven melting, where no residual seed crystals could exist. We also confirmed that laser melting and recrystallization did not affect a sample's ability to form an SCL afterward, which suggests that the 532 nm laser exposure did not generate new chemical species that changed the SCL properties.

To fully characterize the laser induced solid→liquid→solid process, we would ideally measure the wavelength dependence for both melting and solidification, but we were limited by the availability of suitable laser sources to 532 nm. Given the strong overlap of 532 nm with the TEMPO absorption, we assume that direct absorption of the laser light and photothermal vaporization provides the mechanical perturbation to trigger crystallization. Similar mechanical perturbation of an SCL using ultrasonication[40] or laser cavitation[41] have both been shown to be capable of triggering crystallization. These mechanical methods are distinct from other laser-induced crystallization phenomena that rely on high fields to align and trap molecules in solution[28, 42], or on nonlinear laser breakdown to produce chemical defects in the liquid that act as nucleation sites.[43] The optically induced thermal-mechanical method used here to induce a solid→liquid→solid cyclic transformation complements earlier work that relied on photochemistry to accomplish a similar cycle.[27]

The chemical origin of TEMPO's ability to form an SCLs is not obvious. One possible explanation for the stability of the SCL would be formation of a new chemical

species in the liquid phase that inhibits crystallization. UV-Vis absorption measurements on TEMPO in dilute solution, in the solid-state, and in the SCL phase (**Figure 3.5**) all showed the same broad, featureless peak due to the nitroxide radical n→π* transition[44], albeit shifted to slightly longer wavelengths in the solid and SCL. The absorption red-shift and broadening are consistent with the higher dielectric and polarizability of the neat TEMPO samples as compared to liquid $CHCl_3$.[45] The EPR lineshapes of the solid and the

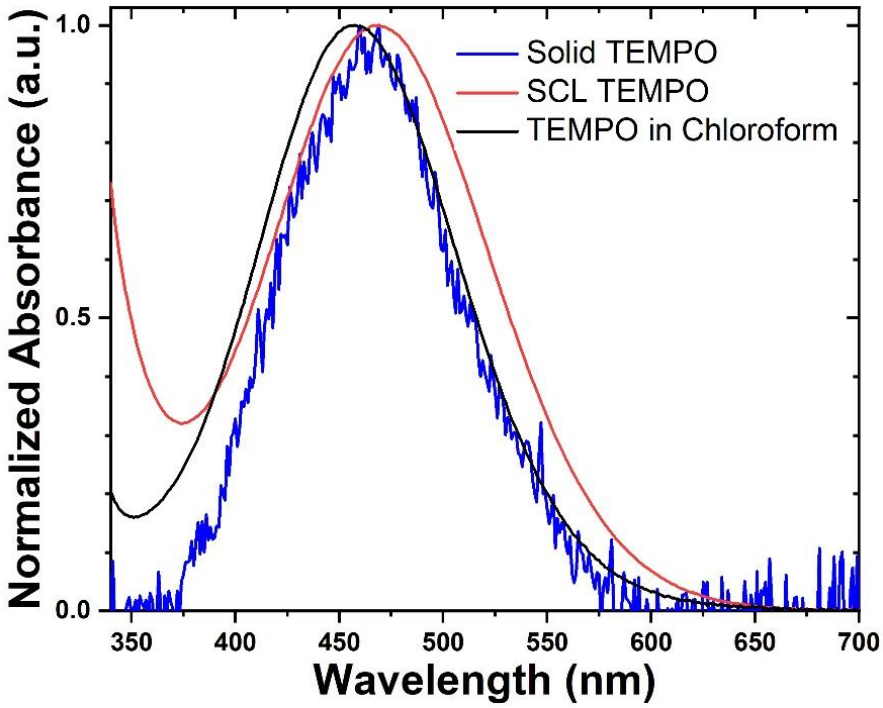

Figure 3.5. UV-Vis absorption spectra of solid TEMPO (blue), TEMPO SCL (red), and dilute TEMPO in chloroform solution (black) at 293 K.

SCL were quite similar except for some additional broadening in the solid (**Figure 3.6a**). We confirmed that isolated TEMPO molecules in liquid solution exhibited the expected hyperfine splitting due to the spin=1 nitrogen atom (**Figure 3.6b**) that collapsed to a single derivative feature in the neat solid and liquid due to enhanced exchange interactions.[46] Previous work has shown that nitroxide radicals can form head-to-head dimers or

oligomers in solution with distinct EPR signatures[47, 48], but these splittings would likely be swamped by the broadening due to rapid exchange in the dense liquid. However, the similar EPR intensities for solid and SCL samples suggested that the spin densities of both phases were within 10% of each other, so there was no indication of extensive spin pairing. Neither UV-Vis nor EPR measurements provided clear evidence for new chemical species that could explain the SCL stability.

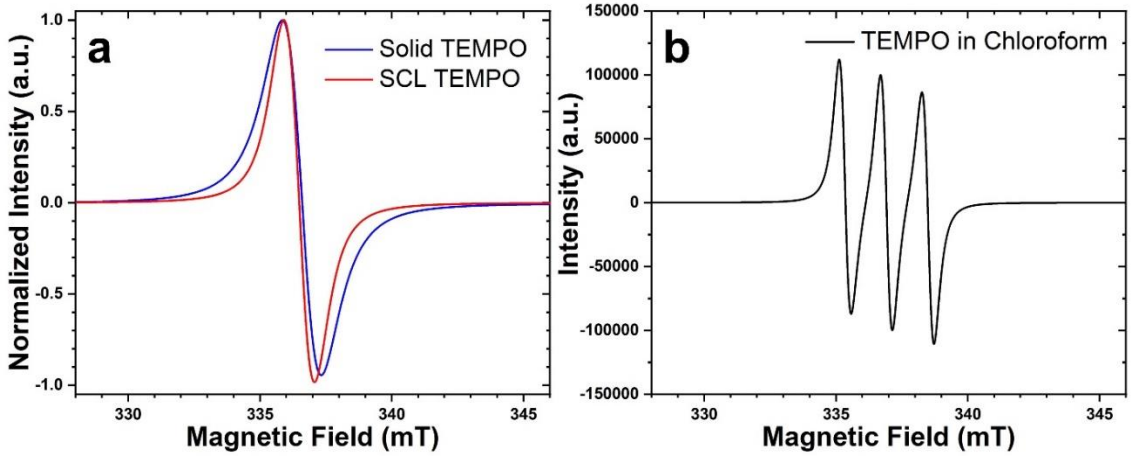

Figure 3.6. EPR spectra of **(a)** TEMPO solid and SCL and **(b)** TEMPO in chloroform solution at 293 K.

If extraneous chemical species do not stabilize the liquid, then the molecular structure itself must play a role. In general, the use of strategic alkyl substitution to decrease molecular symmetry has been successfully used to inhibit crystal growth[9, 49], although exceptions to this rule have also been found.[50] The low ΔH_{fus} of TEMPO indicates that there is not a strong thermodynamic driving force for crystal formation. If the intermolecular interactions are enhanced by adding a hydrogen bonding group, we expect there will be a stronger driving force for crystallization and no SCL formation. This hypothesis was tested using 4-hydroxy-2,2,6,6-tetramethyl-1-piperidine-1-oxyl (TEMPOL), in which an OH group is added to the 6-membered ring opposite to the NO

group. This derivative crystallized immediately after being removed from the oven with no sign of supercooling, suggesting that the presence of a strong directing group can overcome the thermodynamic factors that give rise to the stable SCL for TEMPO.

Finally, we examined whether TEMPO's solid-state structure could provide clues for the SCL stability. TEMPO exhibits three different crystal phases[51], two of which have been fully characterized by single crystal x-ray diffraction. In the monoclinic form, the TEMPO molecules align themselves in head-to-tail rows with the nitroxide substituents pointing in the same direction.[52, 53] The orthorhombic form exhibits very different packing without well-defined layers or orientational ordering.[54] PXRD measurements showed that solid TEMPO is composed of a mixture of the monoclinic and orthorhombic forms. The starting crystal mixture had no effect on formation of the SCL. Resolidification from both the melt and SCL regenerated a monoclinic/orthorhombic mixture, although the relative weighting of the two forms can change (**Supporting Information, Figure S3.5**). Recent work has suggested that solid-state polymorphism can translate to polyamorphism in supercooled liquids.[55] Because sustained crystal growth requires the formation of a nucleus above a critical size[56], one possible explanation for the stability of the TEMPO SCL is that very different microscopic arrangements coexist within the liquid and frustrate largescale crystal growth of either phase. Additional measurements that quantitatively characterize the physical properties of the SCL (vapor pressure, rheology, nucleation kinetics) will be required to evaluate this speculative mechanism.

3.3 Conclusion

In this chapter we characterized the remarkably robust SCL phase of the stable free radical TEMPO. Upon melting and cooling back to room temperature, the SCL can persist for months even after mild physical agitation. The SCL's high vapor pressure can enable crystal growth at remote locations within the sample container. TEMPO's free radical character permits absorption of visible light for melting, while a nanosecond pulse of light can induce recrystallization from the SCL. The capability of cycling between solid and liquid phases using only light as a stimulus may be useful for applications like controllable adhesion or modifying light transmission properties. Although the exact mechanism of the SCL stability is a subject for future investigation, the discovery of TEMPO's supercooling abilities opens up a new class of materials for potential applications as SCLs.

3.4 Supporting Information

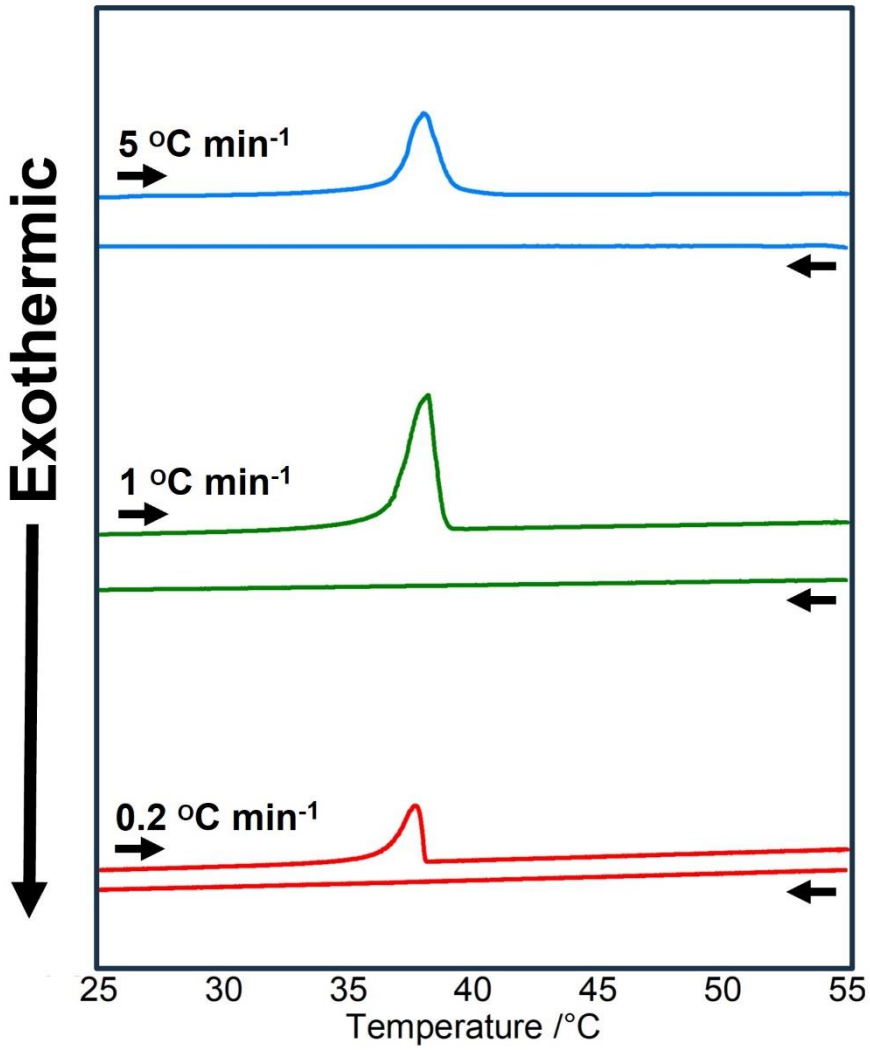

Figure S3.1. DSC thermograms of SCL TEMPO, illustrating an endothermic peak with the absence of an exothermic peak at various heating/cooling rates: 5 °C min^{-1} (blue), 1 °C min^{-1} (green), and 0.2 °C min^{-1} (red)

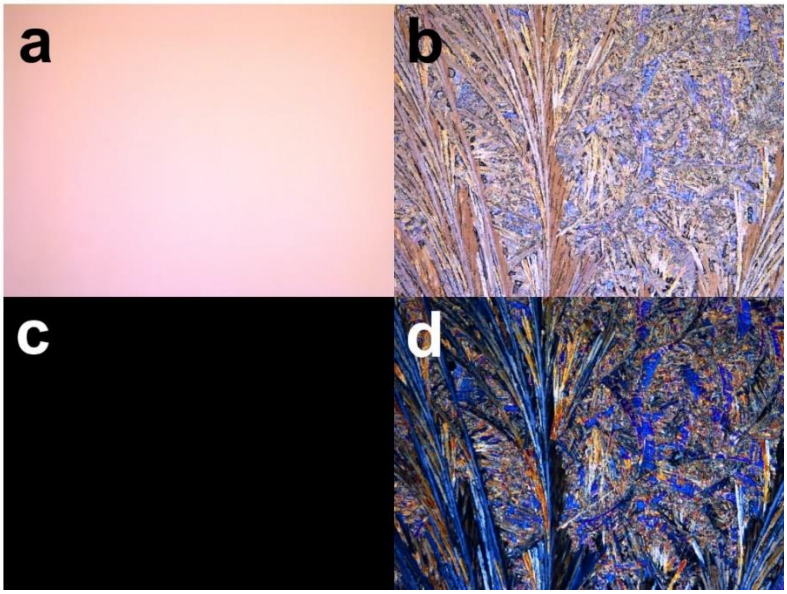

Figure S3.2. Polarized light microscopy of SCL and solid TEMPO. (**a, b**) Unpolarized images of SCL and solid TEMPO. (**c, d**) Corresponding polarized images. No residual birefringence is observed in TEMPO SCL.

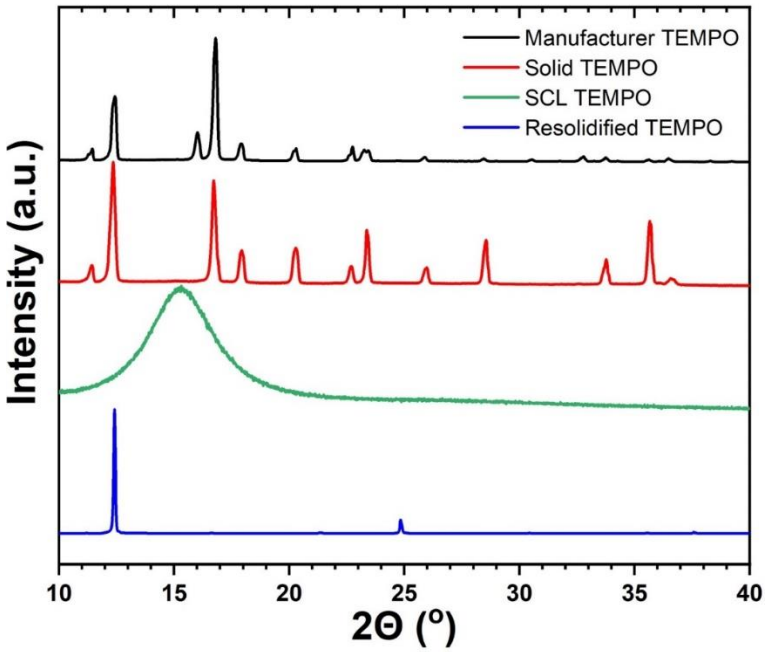

Figure S3.3. Powder X-Ray Diffraction measurements of different TEMPO phases: out of the bottle from the manufacture, ground into a powder (black), melted and then solidified (red), SCL TEMPO (green), and resolidified after becoming a SCL (blue). The broad diffraction peak in the SCL pattern at $2\theta=15.3°$ is typical of organic molecular liquids like benzene and represents the average intermolecular spacing in the liquid. The change in diffraction intensities for the resolidified SCL (blue) reflects increased crystal alignment due to their growth on top of the glass plate.

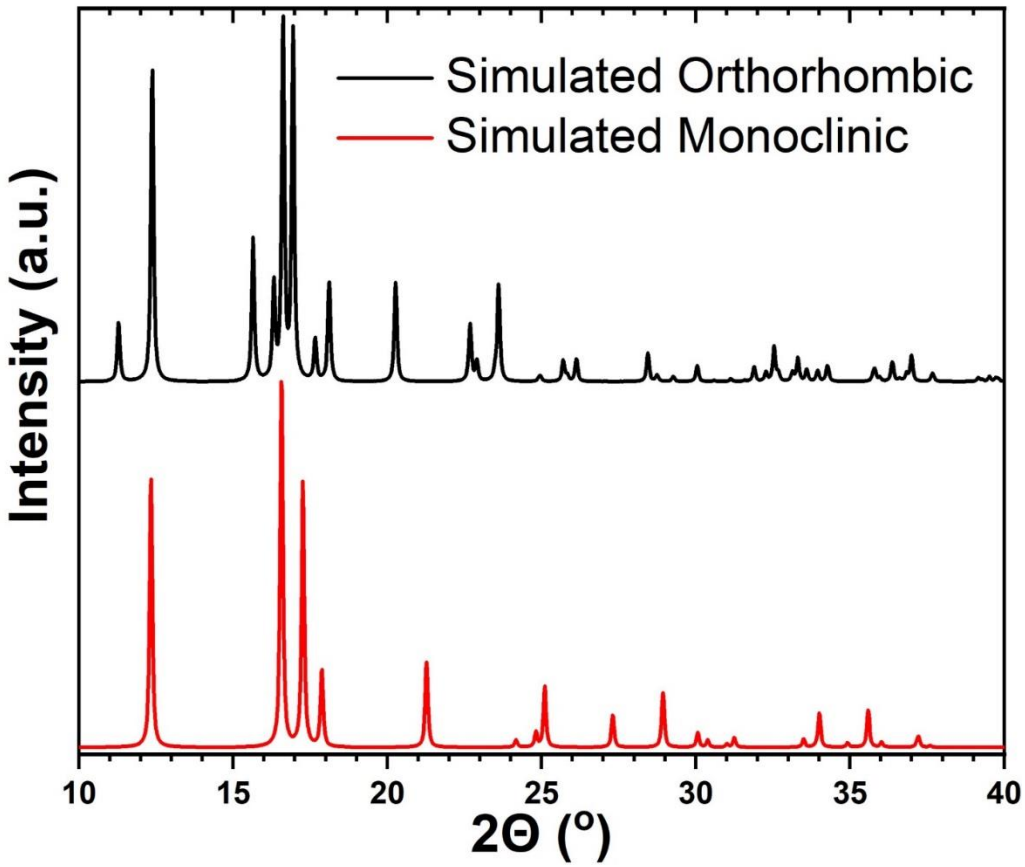

Figure S3.4. Simulated Powder X-Ray Diffraction measurements from the CCDC database of the orthorhombic (black) and monoclinic (red) polymorphs of TEMPO. The orthorhombic polymorph is from CCDC submission 1272628 and the monoclinic polymorph is from CCDC submission 2113192. The orthorhombic peak at 11.2° and the monoclinic peak at 21.4° are diagnostic for the presence of the respective polymorph.

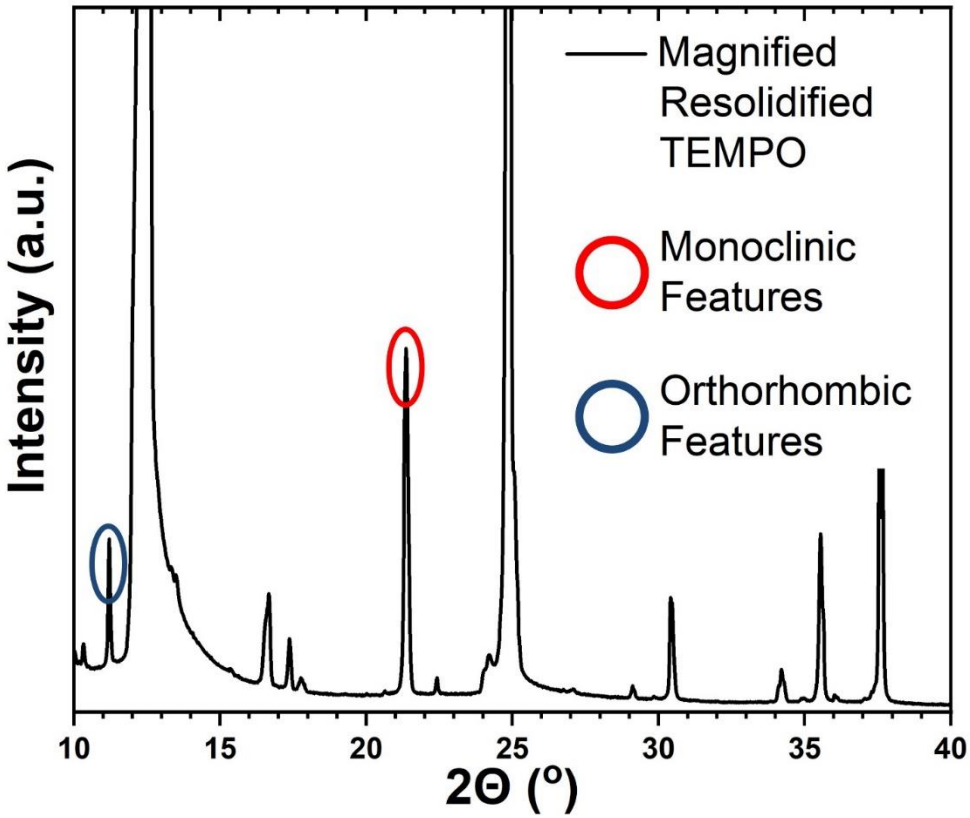

Figure S3.5. Powder X-Ray Diffraction measurement of re-solidified TEMPO SCL (lowest panel of Figure S3), magnified by 80x. The measurement shows a distinct monoclinic peak (circled red) at 21.4° and a distinct orthorhombic peak at 11.2° (circled blue), indicating the presence of both polymorphs. Note that in other regions the peaks of the two polymorphs overlap with varying intensities, making it difficult to unambiguously assign them to the different polymorphs.

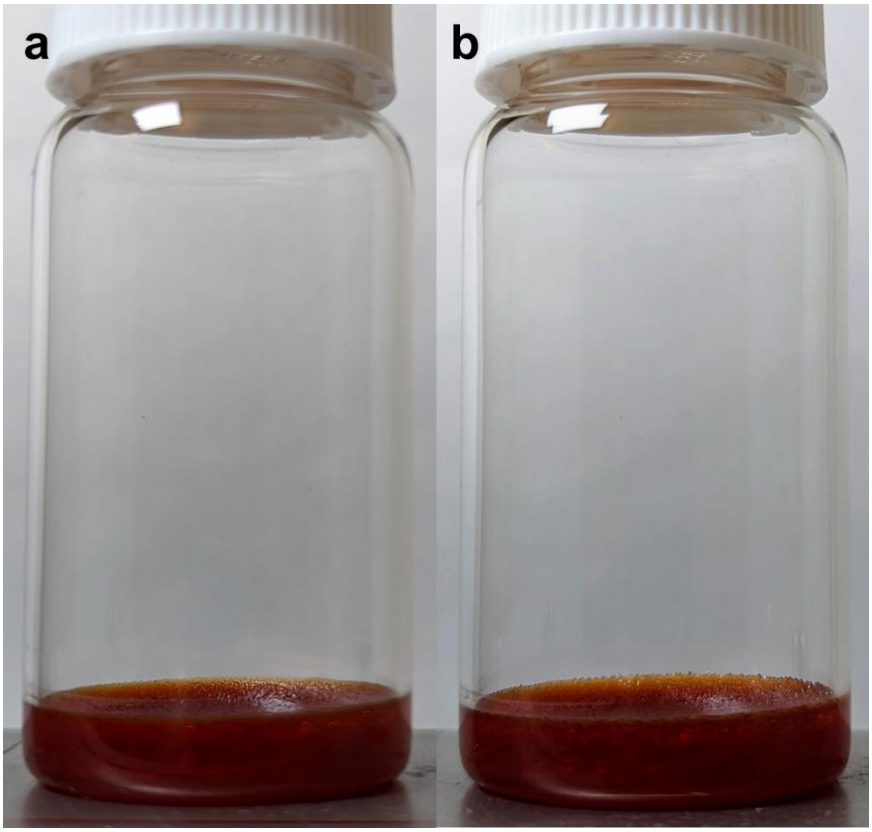

Figure S3.6. No separate crystal growth is observed in the solid TEMPO sample under identical conditions to SCL at the following intervals: (a) initial and (b) after 12 days.

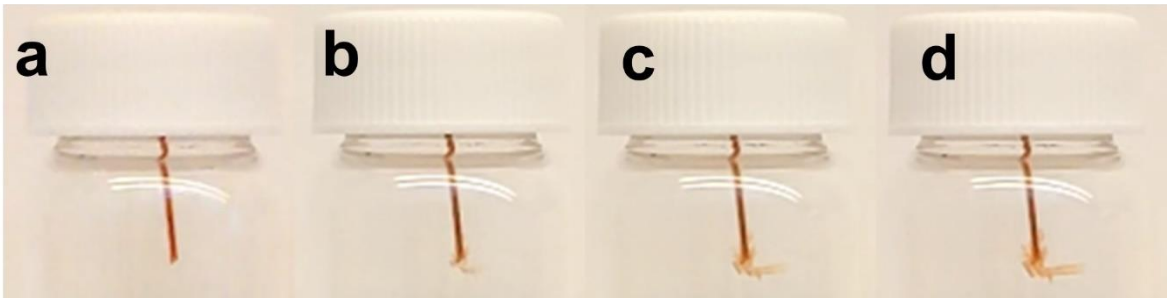

Figure S3.7. Crystal growth at the tip of a TEMPO-filled capillary tube suspended over an SCL sample. The capillary is imaged at different time intervals: **(a)** initial state, **(b)** crystal growth evident after 4 hours, **(c)** after 8 hours, and **(d)** additional crystal growth after 11 hours. The tip of the tube acted as a nucleation site for rapid crystal growth at a remote location.

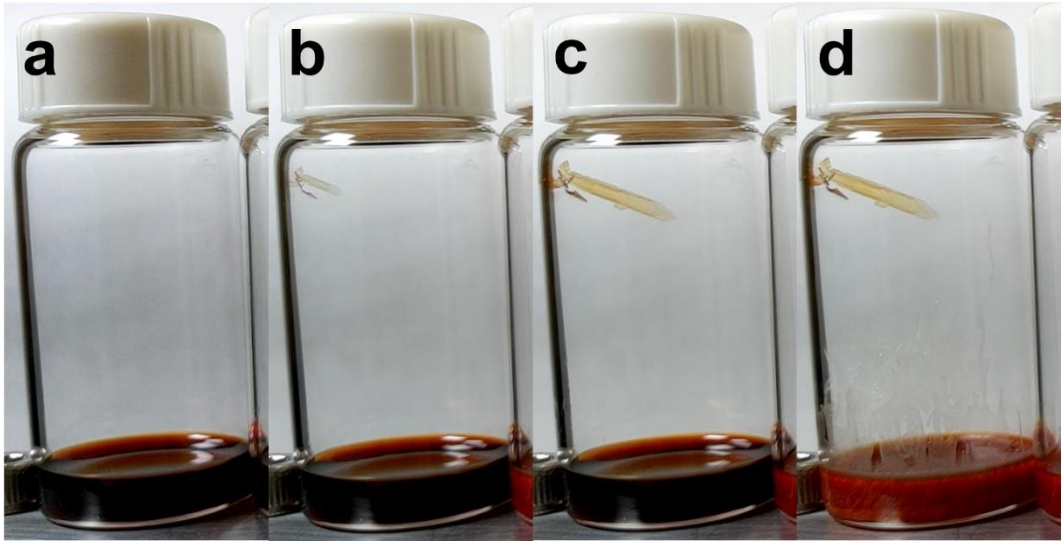

Figure S3.8. Crystal growth of TEMPO by SCL evaporation observed at different time intervals: (**a**) initial state, (**b**) crystal growth evident after 24 hours, (**c**) additional crystal growth after 48 hours, and (**d**) SCL solidification after 50 hours, likely due to a crystal fragment from the top dropping into the liquid.

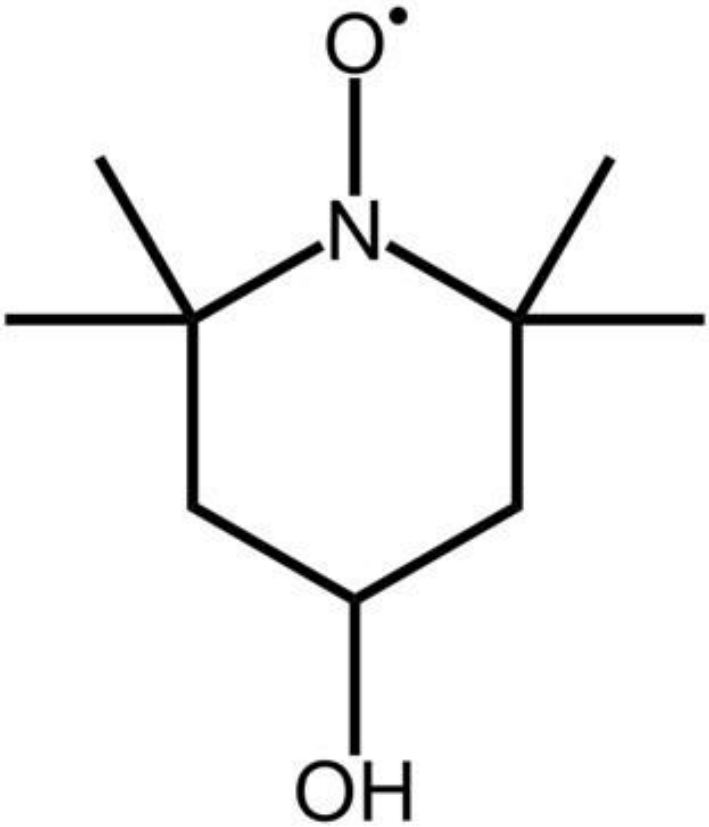

Scheme S3.1. Chemical structure of 4-hydroxy-2,2,6,6-tetramethyl-1-piperidinyloxy (TEMPOL)

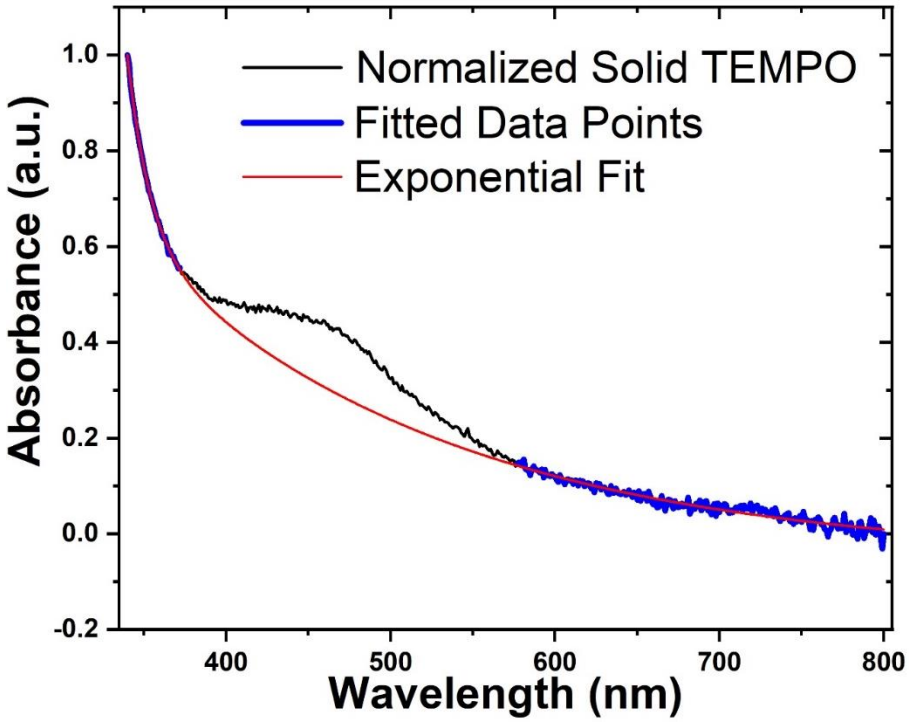

Figure S3.9. Fitting for the solid TEMPO absorption plot in Figure 5. The blue data points were assumed to reflect the scattering background and were fit using a biexponential function of the form $y = A_1*\exp(-x/t_1) + A_2*\exp(-x/t_2) + y_0$, where A_1= 2.814E10, t_1= 13.587, A_2= 3.968, t_2= 190.971, and y_0 = -0.051. The values from the exponential fit were subtracted from the normalized solid TEMPO (black) absorption data, resulting in the peak at 464 nm in Figure 5.

3.5 References

(1) Ediger, M. D.; Pablo, J. d.; Yu, L., Anisotropic Vapor-Deposited Glasses: Hybrid Organic Solids. *Acc. Chem. Res.* **2019,** *52*, 407–414. **doi:** 10.1021/acs.accounts.8b00513

(2) Podzorov, V., Organic single crystals: Addressing the fundamentals of organic electronics. *MRS Bulletin* **2013,** *38*, 15-24. **doi:** 10.1557/mrs.2012.306

(3) Naumov, P.; Chizhik, S.; Panda, M. K.; Nath, N. K.; Boldyreva, E., Mechanically Responsive Molecular Crystals. *Chem. Rev.* **2015,** *115*, 12440–12490. **doi:** 10.1021/acs.chemrev.5b00398

(4) Babu, S. S.; Nakanishi, T., Nonvolatile functional molecular liquids. *Chem. Commun.* **2013,** *49*, 9373-9382. **doi:** 10.1039/c3cc45192e

(5) Ghosh, A.; Nakanishi, T., Frontiers of solvent-free functional molecular liquids. *Chem. Commun.* **2017,** *53*, 10344-10357. **doi:** 10.1039/c7cc05883g

(6) Tateyama, A.; Nakanishi, T., Responsive molecular liquid materials. *Respons. Mater.* **2023,** *1*, e20230001. **doi:** 10.1002/rpm.20230001

(7) Ediger, M. D.; Angell, C. A.; Nagel, S. R., Supercooled Liquids and Glasses. *J. Phys. Chem.* **1996,** *100*, 13200-13212. **doi:** 10.1021/jp953538d

(8) Cavagna, A., Supercooled liquids for pedestrians. *Phys. Rep.* **2009,** *476*, 51-124. **doi:** 10.1016/j.physrep.2009.03.003

(9) Lu, F.; Jang, K.; Osica, I.; Hagiwara, K.; Yoshizawa, M.; Ishii, M.; Chino, Y.; Ohta, K.; Ludwichowska, K.; Kurzydłowski, K. J.; Ishihara, S.; Nakanishi, T., Supercooling of functional alkyl-p molecular liquids. *Chem. Sci.* **2018,** *9*, 6774–6778. **doi:** 10.1039/c8sc02723d

(10) Ryu, H. W.; Woo, S. W.; Shin, B. C.; Kim, S. D., Prevention of supercooling and stabilization of inorganic salt hydrates as latent heat storage materials. *Sol. Energy Mater. Sol. Cells* **1992,** *27*, 161-172. **doi:** 10.1016/0927-0248(92)90117-8

(11) Lane, G. A., Phase change materials for energy storage nucleation to prevent supercooling. *Sol. Energy Mater. Sol. Cells* **1992,** *27*, 135-160. **doi:** 10.1016/0927-0248(92)90116-7

(12) Chung, K.; Kwon, M. S.; Leung, B. M.; Wong-Foy, A. G.; Kim, M. S.; Kim, J.; Takayama, S.; Gierschner, J.; Matzger, A. J.; Kim, J., Shear-Triggered Crystallization and Light Emission of a Thermally Stable Organic Supercooled Liquid. *ACS Cent. Sci.* **2015,** *1*, 94−102. **doi:** 10.1021/acscentsci.5b00091

(13) Hariharan, P. S.; Moon, D.; Anthony, S. P., Crystallization-induced reversible fluorescence switching of alkyl chain length dependent thermally stable

supercooled organic fluorescent liquids. *CrystEngComm* **2017,** *19*, 6489–6497. **doi:** 10.1039/c7ce01650f

(14) Butler, T.; Wang, F.; Daly, M. L.; DeRosa, C. A.; Dickie, D. A.; Sabat, M.; Fraser, C. L., Supercooled Liquid β-Diketones with Mechanoresponsive Emission. *J. Phys. Chem. C* **2019,** *123*, 25788−25800. **doi:** 10.1021/acs.jpcc.9b05948

(15) Sato, Y.; Mutoh, Y.; Morishita, S.; Tsurumachi, N.; Isoda, K., Stimulus-Responsive Supercooled π-Conjugated Liquid and Its Application in Rewritable Media. *J. Phys. Chem. Lett.* **2021,** *12*, 3014−3018. **doi:** 10.1021/acs.jpclett.1c00247

(16) Kutlu, C.; Su, Y.; Lyu, Q.; Riffat, S., Thermal management of using crystallization-controllable supercooled PCM in space heating applications for different heating profiles in the UK. *Renew. Energy* **2023,** *206*, 848-857. **doi:** 10.1016/j.renene.2023.02.077

(17) Yin, Z.; Zhao, Y.; Wan, S.; Yang, J.; Shi, Z.; Peng, S.-X.; Chen, M.-Z.; Xie, T.-Y.; Zeng, T.-W.; Yamamuro, O.; Nirei, M.; Akiba, H.; Zhang, Y.-B.; Yu, H.-B.; Zeng*, M.-H., Synergistic Stimulation of Metal−Organic Frameworks for Stable Super-cooled Liquid and Quenched Glass. *J. Am. Chem. Soc.* **2022,** *144*, 13021−13025. **doi:** 10.1021/jacs.2c04532

(18) Komura, M.; Ogawa, T.; Tani, Y., Room-temperature phosphorescence of a supercooled liquid: kinetic stabilisation by desymmetrisation. *Chem. Sci.* **2021,** *12*, 14363–14368. **doi:** 10.1039/d1sc03800a

(19) Norikane, Y.; Hirai, Y.; Yoshida, M., Photoinduced isothermal phase transitions of liquid-crystalline macrocyclic azobenzenes. *Chem. Commun.* **2011,** *47*, 1770-1772. **doi:** 10.1039/C0CC04052E

(20) Hoshino, M.; Uchida, E.; Norikane, Y.; Azumi, R.; Nozawa, S.; Tomita, A.; Sato, T.; Adachi, S.-i.; Koshihara, S.-y., Crystal Melting by Light: X-ray Crystal Structure Analysis of an Azo Crystal Showing Photoinduced Crystal-Melt Transition. *J. Am. Chem. Soc.* **2014,** *136*, 9158–9164. **doi:** 10.1021/ja503652c

(21) Ishiba, K.; Morikawa, M.-a.; Chikara, C.; Yamada, T.; Iwase, K.; Kawakita, M.; Kimizuka, N., Photoliquefiable Ionic Crystals: A Phase Crossover Approach for Photon Energy Storage Materials with Functional Multiplicity. *Angew. Chem. Int. Ed.* **2015,** *54*, 1532 –1536. **doi:** 10.1002/anie.201410184

(22) Saito, S.; Nobusue, S.; Tsuzaka, E.; Yuan, C.; Mori, C.; Hara, M.; Seki, T.; Camacho, C.; Irle, S.; Yamaguchi, S., Light-Melt Adhesive Based on Dynamic Carbon Frameworks in a Columnar Liquid-Crystal Phase. *Nat. Comm.* **2016,** *7*, 12094/12091-12097. **doi:** 10.1038/ncomms12094

(23) Xu, W.-C.; Sun, S.; Wu, S., Photoinduced Reversible Solid-to-Liquid Transitions for Photoswitchable Materials. *Angew. Chem. Int. Ed.* **2019,** *58*, 9712 –9740. **doi:** 10.1002/anie.201814441

(24) Gerkman, M. A.; Gibson, R. S. L.; Calbo, J.; Shi, Y.; Fuchter, M. J.; Han, G. G. D., Arylazopyrazoles for Long-Term Thermal Energy Storage and Optically Triggered Heat Release below 0 °C. *J. Am. Chem. Soc.* **2020,** *142*, 8688−8695. **doi:** 10.1021/jacs.0c00374

(25) Kuenstler, A. S.; Clark, K. D.; Alaniz, J. R. d.; Hayward, R. C., Reversible Actuation via Photoisomerization-Induced Melting of a Semicrystalline Poly(Azobenzene). *ACS Macro Lett.* **2020,** *9*, 902−909. **doi:** 10.1021/acsmacrolett.0c00328

(26) Komura, M.; Sotome, H.; Miyasaka, H.; Ogawa, T.; Tani, Y., Photoinduced crystal melting with luminescence evolution based on conformational isomerisation. *Chem. Sci.* **2023,** *14*, 5302-5308. **doi:** 10.1039/D3SC00838J

(27) Haruhisa Akiyama; Kanazawa, S.; Okuyama, Y.; Yoshida, M.; Kihara, H.; Nagai, H.; Norikane, Y.; Azumi, R., Photochemically Reversible Liquefaction and Solidification of Multiazobenzene Sugar-Alcohol Derivatives and Application to Reworkable Adhesives. *ACS Appl. Mater. Interfaces* **2014,** *6*, 7933−7941. **doi:** 10.1021/am501227y

(28) Alexander, A. J.; Camp, P. J., Non-photochemical laser-induced nucleation. *J. Chem. Phys.* **2019,** *150*, 040901. **doi:** 10.1063/1.5079328

(29) Zielinska, A.; Takai, A.; Sakurai, H.; Saeki, A.; Leonowicz, M.; Nakanishi, T., A Spin-Active, Electrochromic, Solvent-Free Molecular Liquid Based on Double-Decker Lutetium Phthalocyanine Bearing Long Branched Alkyl Chains. *Chem. Asian J.* **2018,** *13*, 770-774. **doi:** 10.1002/asia.201800175

(30) Xu, W.; Zhu, R.; Tian, Y.; Li, H.; Li, H., Fusion Curves and Enthalpy and Internal Energy Changes of Benzene, Nitrobenzene, Bromobenzene, and Chlorobenzene at Pressures up to 3500 MPa. *J. Chem. Eng. Data* **2007,** *52*, 1975-1978. **doi:** 10.1021/je700276z

(31) Patil, J. R.; Mahanwar, P. A.; Sundaramoorthy, E.; Mundhe, G. S., A review of the thermal storage of phase change material, morphology, synthesis methods, characterization, and applications of microencapsulated phase change material. *J. Polym. Eng.* **2023,** *43*, 354–375. **doi:** 10.1515/polyeng-2022-0254

(32) Stewart, G. W., X-Ray Diffraction in Liquid Normal Paraffins. *Phys. Rev.* **1928,** *31*, 174-179. **doi:** 10.1103/PhysRev.31.174

(33) Stewart, G. W., Diffraction of X-Rays in Liquids: Benzene, Cyclohexane and Certain of Their Derivatives. *Phys. Rev.* **1929,** *33*, 889-899. **doi:** 10.1103/PhysRev.33.889

(34) Tohji, K.; Murata, Y., X-Ray Diffraction Study of the Melting of Benzene. *Jpn. J. Appl. Phys.* **1982,** *21*, 1199-1204. **doi:** 10.1143/JJAP.21.1199

(35) Reid, R. C.; Prausnitz, J. M.; Poling, B. E., *The Properties of Gases and Liquids*. 4 ed.; McGraw-Hill: New York, 1987.

(36) Sen, S.; Zhu, W.; Aitken, B. G., Behavior of a supercooled chalcogenide liquid in the non-Newtonian regime under steady vs. oscillatory shear *J. Chem. Phys.* **2017,** *147*, 034503. **doi:** 10.1063/1.4993780

(37) Murphy, D. M.; Koop, T., Review of the vapour pressures of ice and supercooled water for atmospheric applications. *Q. J. R. Meteorol. Soc.* **2005,** *131*, 1539–1565. **doi:** 10.1256/qj.04.94

(38) Lei, Y. D.; Chankalal, R.; Chan, A.; Wania, F., Supercooled Liquid Vapor Pressures of the Polycyclic Aromatic Hydrocarbons. *J. Chem. Eng. Data* **2002,** *47*, 801-806. **doi:** 10.1021/je0155148

(39) Lui, B. F.; Bardeen, C. J., Using Small Molecule Absorbers to Create a Photothermal Wax Motor. *Small* **2022,** *18*, 2105356. **doi:** 10.1002/smll.202105356

(40) Inada, T.; Zhang, X.; Yabe, A.; Kozawa, Y., Active control of phase change from supercooled water to ice by ultrasonic vibration 1. Control of freezing temperature. *Int. J. Heat Mass Trans.* **2001,** *44*, 4523-4531. **doi:** 10.1016/S0017-9310(01)00057-6

(41) Beaupere, N.; Soupremanien, U.; Zalewski, L., Nucleation triggering methods in supercooled phase change materials (PCM), a review. *Thermochim. Acta* **2018,** *670*, 184–201. **doi:** 10.1016/j.tca.2018.10.009

(42) Garetz, B. A.; Matic, J.; Myerson, A. S., Polarization Switching of Crystal Structure in the Nonphotochemical Light-Induced Nucleation of Supersaturated Aqueous Glycine Solution. *Phys. Rev. Lett.* **2002,** *89*, 175501. **doi:** 10.1103/PhysRevLett.89.175501

(43) Lindinger, B.; Mettin, R.; Chow, R.; Lauterborn, W., Ice Crystallization Induced by Optical Breakdown. *Phys. Rev. Lett.* **2007,** *99*, 045701. **doi:** 10.1103/PhysRevLett.99.045701

(44) Falbo, E.; Fusè, M.; Lazzari, F.; Mancini, G.; Barone, V., Integration of Quantum Chemistry, Statistical Mechanics, and Artificial Intelligence for Computational Spectroscopy: The UV−Vis Spectrum of TEMPO Radical in Different Solvents. *J. Chem. Theory Comput.* **2022,** *18*, 6203−6216. **doi:** 10.1021/acs.jctc.2c00654

(45) Bardeen, C. J., The Structure and Dynamics of Molecular Excitons. *Ann. Rev. Phys. Chem.* **2013,** *65*, 127-148. **doi:** 10.1146/annurev-physchem-040513-103654

(46) Capiomont, A.; Chion, B.; Lajzerowicz-Bonneteau, J.; Lemaire, H., Interpretation and utilization for crystal stucture determination of ESR spectra of single crystals of nitroxide free radicals. *J. Chem. Phys.* **1974,** *60*, 2530–2535. **doi:** 10.1063/1.1681393

(47) Kooser, R. G., Nitroxide Spin Label Dimer Pairing: A Cautionary Note. *Macromolecules* **1987,** *20*, 435–436. **doi:** 10.1021/ma00168a037

(48) Kanzaki, Y.; Shiomi, D.; Sato, K.; Takui, T., Biradical Paradox Revisited Quantitatively: A Theoretical Model for Self-Associated Biradical Molecules as Antiferromagnetically Exchange Coupled Spin Chains in Solution. *J. Phys. Chem. B* **2012,** *116*, 1053-1059. **doi:** 10.1021/jp211391x

(49) Zheng, X.; Nagura, K.; Takaya, T.; Hashi, K.; Nakanishi, T., Quest for a Rational Molecular Design of Alkyl-Distyrylbenzene Liquid by Substitution Pattern Modulation. *Chem. Eur. J.* **2023,** *29*, e202203775. **doi:** 10.1002/chem.202203775

(50) Lu, F.; Shinohara, A.; Kawamura, I.; Saeki, A.; Takaya, T.; Iwata, K.; Nakanishi, T., Room-Temperature Alkyl-Diphenylpyrene Liquefication by Molecular Desymmetrization. *Helv. Chim. Acta* **2023,** *106*, e202300050. **doi:** 10.1002/hlca.202300050

(51) Bordeaux, D.; Bornarel, J.; Capiomont, A.; Lajzerowicz-Bonneteau, J.; Lajzerowicz, J.; Legrand, J. F., New Ferroelastic-Ferroelectric Compound: Tanane. *Phys. Rev. Lett.* **1973,** *31*, 314-317. **doi:** 10.1103/PhysRevLett.31.314

(52) Stefan, S.; Belaj, F.; Madl, T.; Pietschnig, R., A Radical Approach to Hydroxylaminotrichlorosilanes: Synthesis, Reactivity, and Crystal Structure of TEMPO-$SiCl_3$ (TEMPO = 2,2,6,6-Tetramethylpiperidine-N-oxyl). *Eur. J. Inorg. Chem.* **2010**, 289-297. **doi:** 10.1002/ejic.200900969

(53) Ranjan, S.; Takamizawa, S., Characterization of Organoferroelasticity in a TEMPO Crystal. *Cryst. Growth Des.* **2022,** *22*, 585−589. **doi:** 10.1021/acs.cgd.1c01141

(54) Yasunori, Y.; Kenichi, O.; Hiroyuki, N., Structural Implication of Oxoammonium Cations for Reversible Organic One-electron Redox Reaction to Nitroxide Radicals. *Chem. Lett.* **2007,** *36*, 866-867. **doi:** 10.1246/cl.2007.866

(55) Walton, F.; Bolling, J.; Farrell, A.; MacEwen, J.; Christopher D. Syme; Jiménez, M. G. l.; Senn, H. M.; Wilson, C.; Cinque, G.; Wynne, K., Polyamorphism Mirrors Polymorphism in the Liquid–Liquid Transition of a Molecular Liquid. *J. Am. Chem. Soc.* **2020,** *142*, 7591–7597. **doi:** 10.1021/jacs.0c01712

(56) Chung, K.; Yang, D. S.; Kim, J., Functional Organic Supercooled Liquids. In *Functional Organic Liquids*, Nakanishi, T., Ed. Weinheim, Germany: New York, 2019.

Chapter 4. Photoinduced Paramagnetism in HABI

We turn our attention to working with photochromic HABI that can generate free radicals when irradiated with light.

4.1 Introduction

Photochromic compounds, those which exhibit changes in color when irradiated with light, have been studied extensively.[1–13] These changes occur because photochromic molecules react and transform when irradiated, most commonly through cycloaddition[14], isomerization[12], and cyclization[13]. This change in structure is accompanied by a change in the absorption spectra which can indicate the amount of conversion. These changes can be initiated with either infrared, visible, or UV light and are reversible with radiation, time, or heating.[4] The functional groups present on photochromic compounds affect which light is absorbed and consequently determine the reaction pathway that leads to molecular transformation and change in color.

Ortho-chloro-hexaarylbiimidazole, otherwise known as o-Cl-HABI but will be referred to as HABI for ease, is a photochromic molecule that was discovered in the 1960s by Hayashi and Maeda[8], changing from yellow to violet when irradiated as shown in **Figure 4.1**. HABI can be homolytically cleaved via the C-N bonds to form 2 geminate triphenylimidazolyl radicals (TPIRs) (**Figure 4.2**).[1] The HABI molecules are cleaved both thermally and photochemically to generate the radicals.

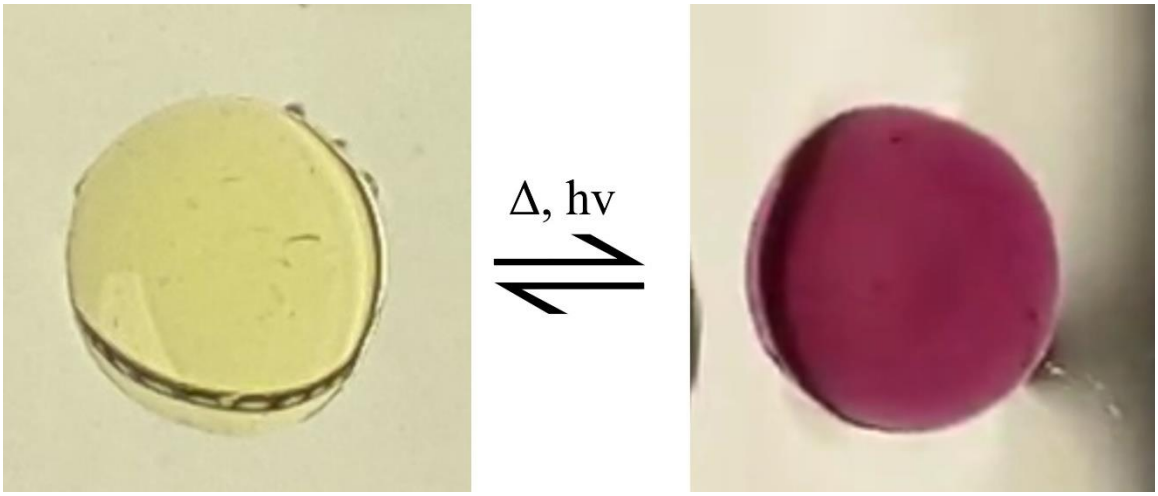

Figure 4.1: (Left) HABI/PMMA film without irradiation and **(Right)** HABI/PMMA film after irradiation.

In solution, the dimerization of TPIR to HABI typically takes several minutes due to the diffusion of radical isomers. Abe et al. implemented molecular design strategies, such as using bridge moieties like naphthalene[15], paracyclophane[1], ortho-position phenyl[16], and other linkers, accelerating the dimerization process to the microsecond scale. The selected bridge moieties shorten the dimerization half-life time to 260 ms[11], 35 μs[17], and 3.5 μs[16] at 298 K, respectively. TPIR/HABI has been utilized to create multi-responsive

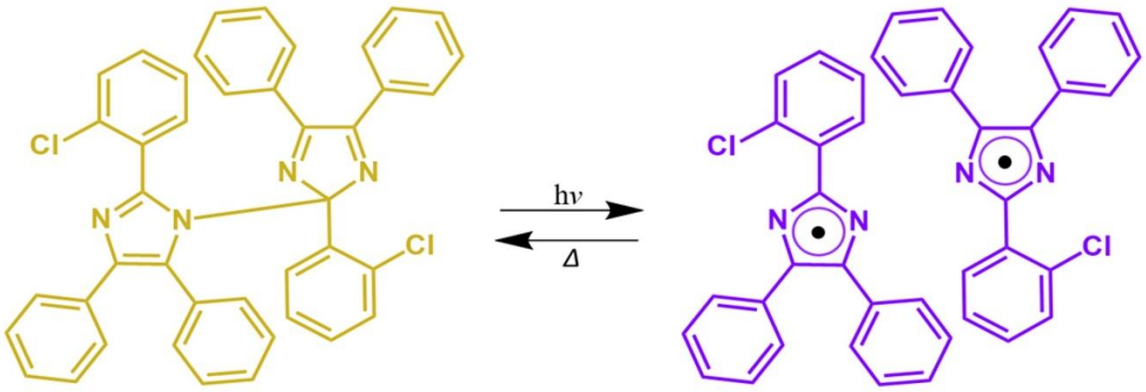

o-Cl-HABI triphenylimidazolyl radical (TPIRs)

Figure 4.2. HABI molecule. (**Left**) The monomer, o-Cl-HABI and (**Right**) triphenylimidazolyl radicals (TPIRs)

devices and materials. Liu et al. designed field-effect transistors (FETs) with blended thin films of two HABI derivatives and polymer PDPP4T, demonstrating tunable semiconductor performance through light irradiation and heating[18]. Ahn et al. explored the application of the photoresponsive properties of triphenyl imidazolyl radicals/hexaarylbiimidazole (TPIR/HABI) for designing cross-polymeric matrices with reversible "healing" capabilities.[19] They developed covalently cross-linked gels by incorporating HABI groups into the polymer backbone, resulting in a novel and highly dynamic healable polymer gel.[19] Xiang et al. developed a 2-glycol-HABI based light-responsive smart polymer material HABI-PU, demonstrating rapid self-healing within seconds through light-induced mechanisms.[20]

We explored HABI due to its long-lived free radical states. Having a recombination rate on the order of minutes enables its use before the reverse reaction takes place.

HABI, without any intervention is a diamagnetic compound[1].The presence of free radicals introduces paramagnetic properties to this photogenerated species, expanding its potential applications. With HABI, we can use optical excitation to switch its magnetic properties from diamagnetic to paramagnetic (or less diamagnetic) to create localized motion using an external magnetic field.

Herein we present a method to produce magnetic films using HABI with PMMA as a scaffold. We are determined to use photoexcitation to generate unpaired electrons in a HABI PMMA matrix, transforming its magnetic susceptibility (χ).

4.2 Results and Discussion

In our quest for a deeper understanding of the dynamics governing HABI radical recovery at room temperature, we employed a dual methodology involving UV-Vis and EPR techniques. Our first objective was to unravel the kinetics of the HABI radical recovery process in both solution and in polymer, both of which are shown in **Figure 4.3a** and **Figure 4.3b** respectively.

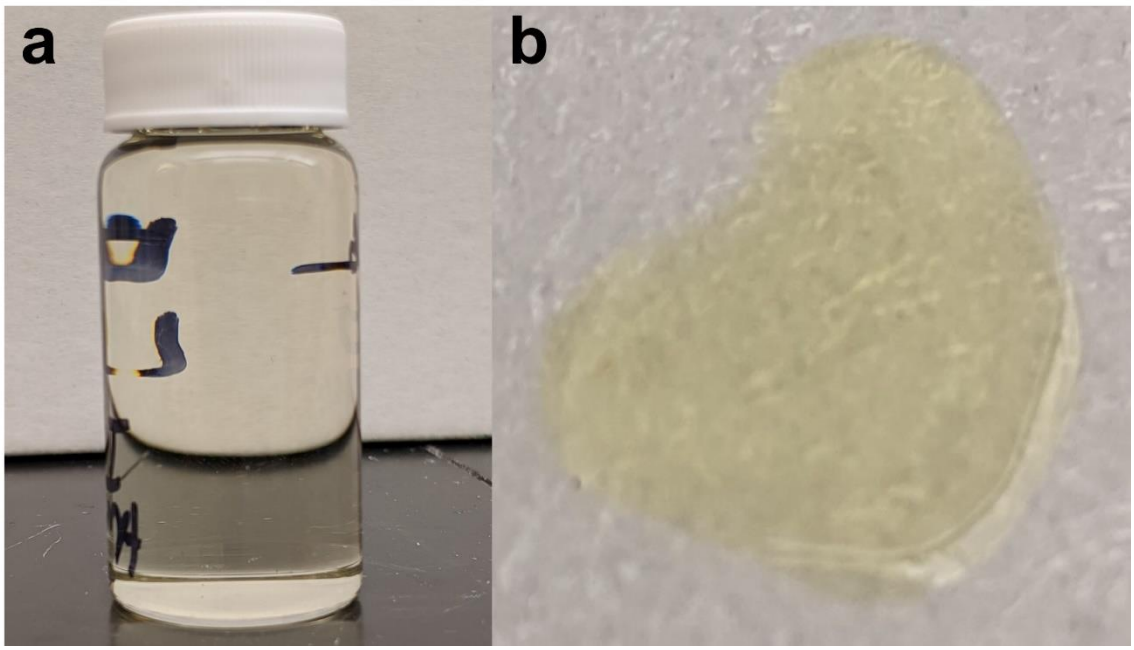

Figure 4.3. **a)** 1.0 mM HABI in toluene solution and **b)** 1:1 HABI in PMMA film

4.2.1 HABI in Solution

We started with HABI in solution, and then went onto HABI in polymer. UV-Vis absorption of 1.0 mM HABI in toluene solution was obtained (**Figure 4.4**). As depicted in the representation within **Figure 4.5**, the graph spotlighting the behavior of the HABI solution in toluene unveiled a linear correlation between radical recovery and 1/absorbance against time. This linear relationship offers a telling clue that the kinetics of the radical

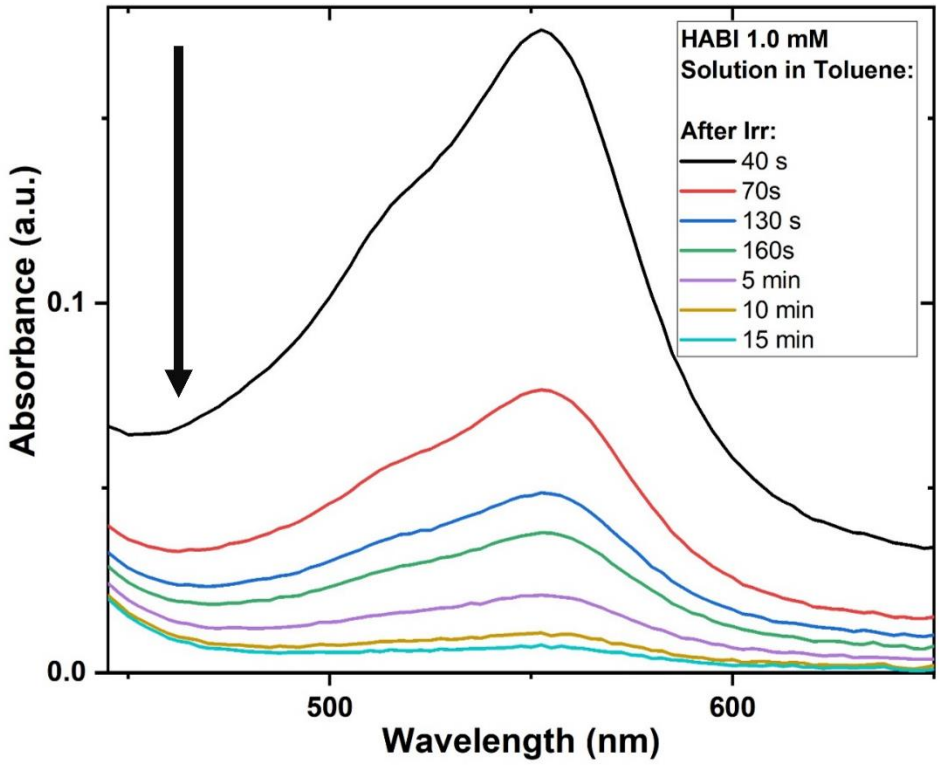

Figure 4.4. UV-Vis spectra of HABI in Toluene solution. There is 99 % recovery within 15 minutes.

recovery conform to the characteristics of a second-order process[21], encapsulated in the following equation:

$$rate = -\frac{\Delta[A]}{2\Delta t} = k[A]^2 \tag{4.1}$$

Here, the symbol *A* signifies absorbance, *t* represents time, and *k* stands as the rate constant. We can integrate (4.1) to obtain:

$$\frac{1}{[A]} = kt + \frac{1}{[A_0]} \tag{4.2}$$

The resulting equation creates a linear trend when plotted that matches with the data in **Figure 4.5**, thus confirming second-order kinetics. The second-order rate law suggests that the reaction rate is more sensitive to concentration changes than a first-order reaction. By overlaying peak absorbance from UV-Vis and peak field from EPR at different TPIR

recover intervals shown in **Figure 4.6**, it is confirmed that the TPIRs recover at least 99 % within 15 minutes.

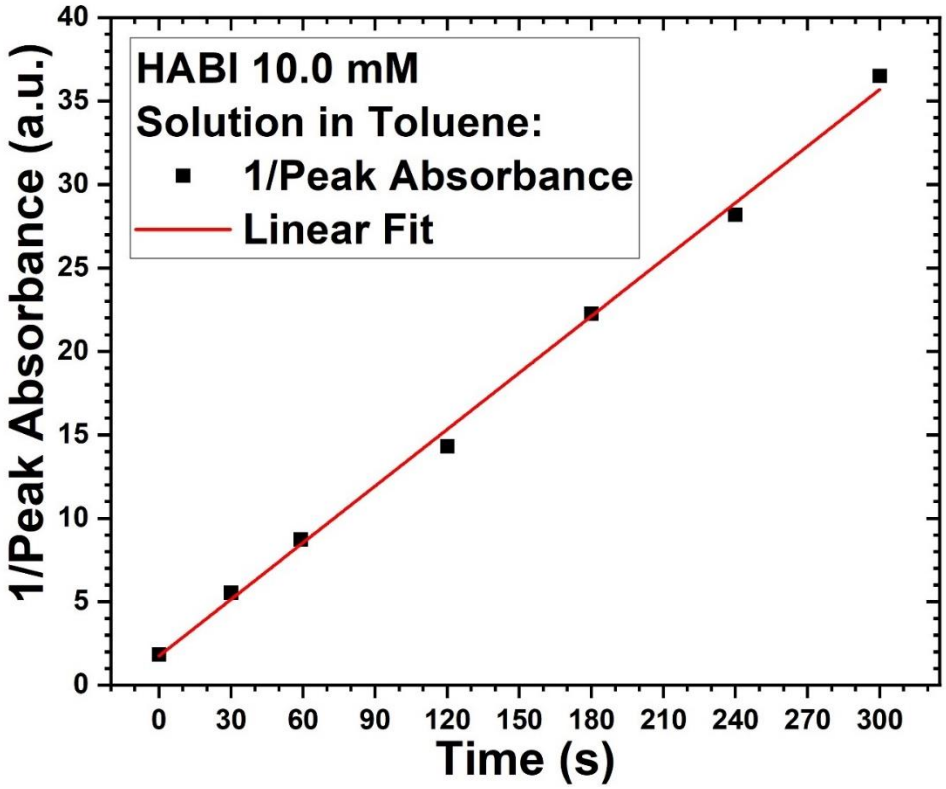

Figure 4.5. Plot of 1/peak absorbance over time for 10.0 mM HABI solution in toluene showing 2nd order kinetics of TPIR dimerization.

4.2.2 HABI in Polymer Films

Film Prep: HABI presented many challenges to overcome. We first began by drop casting roughly 3 cm diameter non-uniform circular 1:1 HABI films onto glass slides (substrates). Spin coating was an option, however, even at slow speeds, the films would dry too thin. Once the HABI films were dried overnight, they needed to be removed from the substrates. However, PMMA adheres very well to glass, so we needed to use a razor blade to take the HABI films off. Unfortunately, the films would fracture most of the time since PMMA

becomes very brittle when mixed with HABI, and only randomly sized pieces were left to use for experiments.

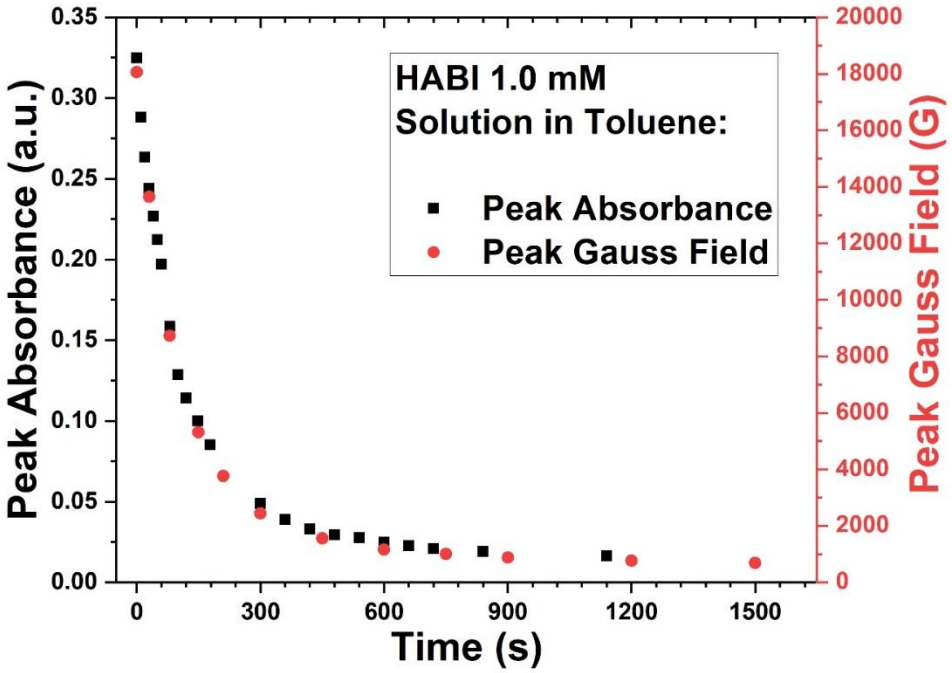

Figure 4.6. Overlaid plot of peak absorbance from UV-Vis and peak Gauss field from EPR over time. Both UV-Vis and EPR radical recovery data overlap.

Deadhesion was the first of many pitfalls. To rectify the deadhesion issue, there needed to be a way to separate the HABI films from the substrates. The solution was simple, yet effective: coat the substrates with a material that could dissolve off without affecting the integrity of the samples. That would allow the HABI films to cleanly come off the substrate. The candidate that worked for this was polyvinyl alcohol (PVA). PVA is a water-soluble material that does not react with the HABI films. A 4% PVA/water solution was used to first coat all the substrates. They were dried overnight and were ready for use as PVA substrates. Once HABI films were drop casted onto the PVA substrates and dried,

they could be submerged in water. Over some time, usually about 15 minutes, the HABI films would then pop off the PVA substrates and were ready to be used.

The second challenge was film clarity; films would sometimes dry hazily instead of transparent. It was imperative the films were clear so that light could pass through the entire sample, allowing the whole sample to be irradiated when the time came. Our sample preparation began on the benchtop. Substrates would be placed in a glass petri dish on the benchtop, and samples were drop casted in the open air. At the time, we were unaware that the drying rate of the dichloromethane (DCM) solution, the solution used to make the HABI film solution, was nonuniform when drying in the open air. Depending on the rate of evaporation from sample to sample, haziness sometimes formed. The first course of action was covering the petri dish with a cardboard box to eliminate the flow of ambient air. While haziness appeared less often with this method, it was still very much apparent. It was then hypothesized that the variations with room temperature day to day may be the culprit. Instead of drying on the benchtop, they were placed in an insulated furnace that was left off. The temperature of the inside the furnace should not fluctuate compared to the ambient air in the lab. This method, however, still left some samples to be hazy. The next technique did work. It was determined that the DCM that was evaporating needed a small, closed environment to create a saturated DCM environment above the HABI films to allow uniform evaporation. To do this, a second, slightly larger, petri dish was placed upside down on top of the petri dish holding the samples. This allowed for the creation of the closed DCM environment needed for uniform evaporation. After switching over to using two petri dishes, there was no more haziness.

Kinetics: Our attention also turned to the kinetics governing HABI/PMMA polymer films (referred to as HABI films) under ambient conditions, and it was observed that HABI films follow different kinetics than HABI in solution[21]. From the UV-Vis spectra shown in **Figure 4.7**, 80+/-2% of the TPIRs recover within an hour, however, the time it takes for the rest of the radicals to recover can be many hours. **Figure 4.8** shows that there is a strong

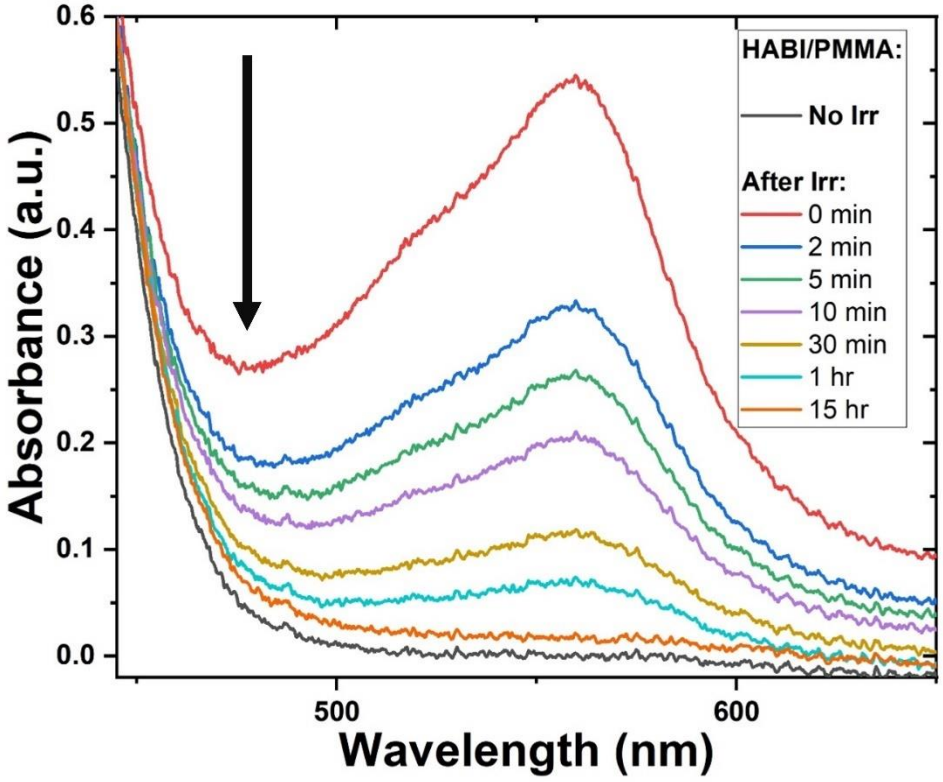

Figure 4.7. UV-Vis spectra of HABI/PMMA films.

EPR signal with 40% of radicals still present in the sample after 24 hours, which is in agreement to Morita et. al.[22] We first hypothesized that the radicals are stuck in the polymer matrix and cannot move as freely as they would in a liquid to recombine. However, if that were the case, we should have still seen a strong UV-Vis absorption at 550 nm which

indicates TPIR. As it turns out, PMMA radicals were being formed upon HABI film irradiation.[23]

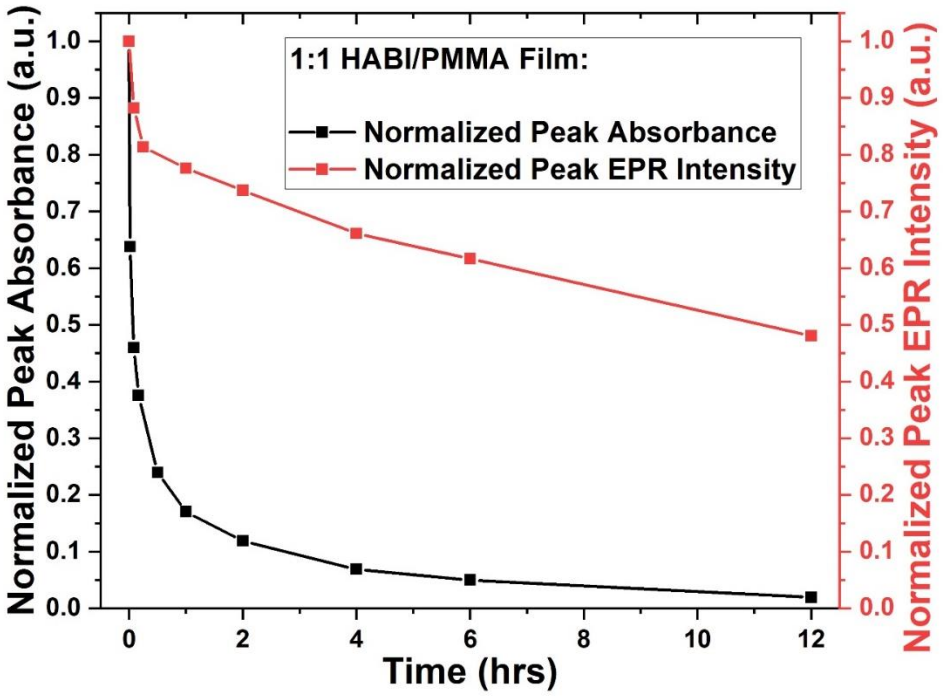

Figure 4.8. Overlaid plot of normalized peak absorbance from UV-Vis and normalized peak intensity from EPR over time for HABI films. While there is almost full recovery via UV-Vis, there are still 40 % radicals left via EPR.

Photoinduced Motion: It was impossible to show photomechanical motion on any surface other than water due to excess surface friction, so water was decided as the experiments' interface. But while it was possible for HABI films to float and move on the surface of a water using a magnetic field, it was determined that even without an irradiation source, HABI films could also move without any irradiation.

Since HABI films are slightly diamagnetic[3], they were expected to be repelled and to move away when presented near a magnet. However, sometimes the HABI films were attracted to the magnet. This not only happened to HABI films, but any floatable material

we tried moved as well such as wood, Styrofoam, and aluminum foil. Well, it turns out the χ of the water has a role to play in how materials move on the surface of water when in the presence of a magnetic field. Water has a volume χ of -9.035×10^{-6} and PMMA has a χ of -9.06×10^{-6}.[24,25] If a material is more diamagnetic (bigger negative value), than water, it should be repelled by a magnetic field when floating on water, and if a material is less diamagnetic (lower negative value), than water, it should be attracted by a magnetic field when floating on water.

Since the HABI films are more diamagnetic than water, they should always be repelled but that was shown to not always be the case. To rectify this issue, the χ needed to be controlled, and the easiest way to do that was to dope the water with a material that is unnreactive. We tried ethanol, but samples sank to the bottom of the water dish. This is because there was not enough surface tension. The material chosen was copper sulfate, which has been used to adjsust the χ of water.[26] We made a 38.47% saturated solution with Millipore water, which had a χ of 0. This allowed for the samples to always be more diamagnetic to the water, allowing to see repulsion when in the presence of a magnet every time.

With irradiation, the TPIRs are formed within the HABI films, changing the film's χ to paramagnetic. After irradiating some of our samples, we were able to successfully demonstrate photomechanical motion using a magnet to move HABI films (**Figure 4.9**). However, even with the χ of water being controlled, HABI occasionally displayed unusual behavior once irradiated. It was expected that every irradiated HABI film sample would become attracted to the magnet; however, some samples were unresponsive. Possible

reasons for this lack of photomechanical motion could include inconsistencies in film composition, variability in film thickness, and inhomogeneous irradiation. Despite efforts to control these parameters, further experiments are necessary to fully explain the observed results.

4.3 Conclusion

In this chapter, our focus centered on the photochemical exploration of HABI, a photochromic compound capable of generating free radicals upon light irradiation. The results and discussions presented in this chapter shed light on the kinetics of HABI radical recovery, both in solution and in polymer films. Our dual methodology, combining UV-Vis and EPR techniques, provided valuable insights into the recovery processes. In solution, the second-order kinetics of radical recovery were confirmed, while the formation of PMMA radicals upon HABI film irradiation made the HABI radicals difficult to isolate.

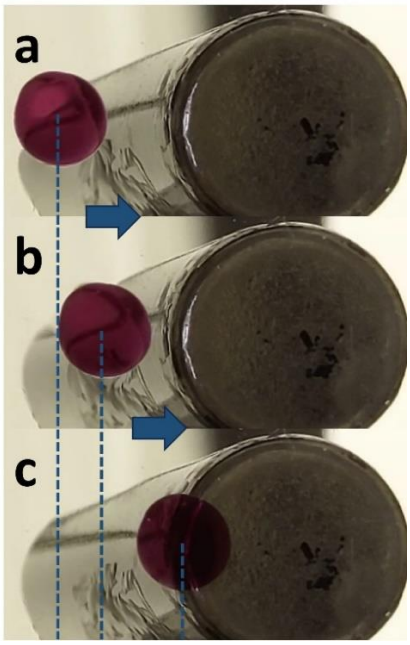

Figure 4.9. Irradiated HABI/PMMA film moving towards a cylindrical N52 magnet at different time intervals: **a)** 0 seconds, **b)** 2 seconds, and **c)** 4 seconds.

Overcoming obstacles in sample preparation, such as deadhesion and haziness, was crucial for the success of our experiments. The use of PVA as a substrate coating proved effective in facilitating the removal of HABI films without compromising sample integrity. Additionally, controlling film clarity through optimized drying methods ensured the transparency necessary for effective light irradiation.

As shown in **Figure 4.9**, photomechanical motion is indeed possible, but despite the efforts of attempting to show photomechanical motion of HABI films, we were unable to reliably observe this behavior, which is why we moved on to studying the photothermal properties of pyrolytic graphite to induce photomechanical motion.

4.4 References

(1) Kishimoto, Y.; Abe, J. A Fast Photochromic Molecule That Colors Only under UV Light. *J Am Chem Soc* **2009**, *131* (12), 4227–4229. https://doi.org/10.1021/ja810032t.

(2) Ooyama, Y.; Yagi, S. *Progress in the Science of Functional Dyes*; Ooyama, Y., Yagi, S., Eds.; Springer Singapore: Singapore, 2021. https://doi.org/10.1007/978-981-33-4392-4.

(3) Abe, J.; Yamashita, H.; Mutoh, K. Photochromism. In *Encyclopedia of Polymeric Nanomaterials*; Springer Berlin Heidelberg: Berlin, Heidelberg, 2015; pp 1572–1579. https://doi.org/10.1007/978-3-642-29648-2_119.

(4) Irie, M. Photochromism: Memories and SwitchesIntroduction. *Chem Rev* **2000**, *100* (5), 1683–1684. https://doi.org/10.1021/cr980068l.

(5) Maeda, K.; Hayashi, T. The Mechanism of Photochromism, Thermochromism and Piezochromism of Dimers of Triarylimidazolyl. *Bulletin of the Chemical Society of Japan*. 1970, pp 429–438. https://doi.org/10.1246/bcsj.43.429.

(6) Bagheri, M.; Mirzaee, M.; Hosseini, S.; Gholamzadeh, P. The Photochromic Switchable Imidazoles: Their Genesis, Development, Synthesis, and Characterization. *Dyes and Pigments* **2022**, *203* (April), 110322. https://doi.org/10.1016/j.dyepig.2022.110322.

(7) Nath, N. K.; Runčevski, T.; Lai, C.-Y.; Chiesa, M.; Dinnebier, R. E.; Naumov, P. Surface and Bulk Effects in Photochemical Reactions and Photomechanical Effects in Dynamic Molecular Crystals. *J Am Chem Soc* **2015**, *137* (43), 13866–13875. https://doi.org/10.1021/jacs.5b07806.

(8) Maeda, K.; Hayashi, T. Photochromic Color Change of the Dimer of Triphenylimidazolyl at Low Temperatures. *Bull Chem Soc Jpn* **1969**, *42* (12), 3509–3514. https://doi.org/10.1246/bcsj.42.3509.

(9) Irie, M.; Fukaminato, T.; Matsuda, K.; Kobatake, S. Photochromism of Diarylethene Molecules and Crystals: Memories, Switches, and Actuators. *Chem Rev* **2014**, *114* (24), 12174–12277. https://doi.org/10.1021/cr500249p.

(10) Ito, H.; Tanaka, S.; Mutoh, K.; Abe, J. Fast Photochromism of the Imidazole Dimers Bridged by Group 14 Atoms. *Org Lett* **2020**, *22* (14), 5680–5684. https://doi.org/10.1021/acs.orglett.0c02072.

(11) Fujita, K.; Hatano, S.; Kato, D.; Abe, J. Photochromism of a Radical Diffusion-Inhibited Hexaarylbiimidazole Derivative with Intense Coloration and Fast Decoloration Performance. *Org Lett* **2008**, *10* (14), 3105–3108. https://doi.org/10.1021/ol801135g.

(12) Kataoka, K.; Kobayashi, T.; Arai, T. *Photochromism of Organic Compounds Undergoing Isomerization Around the C═C Double Bond and/or Intramolecular Hydrogen Atom Transfer: Small and Large Structural Change*; 2013. https://doi.org/10.1007/978-4-431-54291-9_13.

(13) Lvov, A. G.; Khusniyarov, M. M.; Shirinian, V. Z. Azole-Based Diarylethenes as the next Step towards Advanced Photochromic Materials. *Journal of Photochemistry and Photobiology C: Photochemistry Reviews* **2018**, *36*, 1–23. https://doi.org/10.1016/j.jphotochemrev.2018.04.002.

(14) Wang, H.; Chen, P.; Wu, Z.; Zhao, J.; Sun, J.; Lu, R. Bending, Curling, Rolling, and Salient Behavior of Molecular Crystals Driven by [2+2] Cycloaddition of a Styrylbenzoxazole Derivative. *Angewandte Chemie International Edition* **2017**, *56* (32), 9463–9467. https://doi.org/10.1002/anie.201705325.

(15) Iwahori, F.; Hatano, S.; Abe, J. Rational Design of a New Class of Diffusion-inhibited HABI with Fast Back-reaction. *J Phys Org Chem* **2007**, *20* (11), 857–863. https://doi.org/10.1002/poc.1183.

(16) Yamashita, H.; Abe, J. Pentaarylbiimidazole, PABI: An Easily Synthesized Fast Photochromic Molecule with Superior Durability. *Chem. Commun.* **2014**, *50* (62), 8468–8471. https://doi.org/10.1039/C4CC03137G.

(17) Harada, Y.; Hatano, S.; Kimoto, A.; Abe, J. Remarkable Acceleration for Back-Reaction of a Fast Photochromic Molecule. *J Phys Chem Lett* **2010**, *1* (7), 1112–1115. https://doi.org/10.1021/jz100228w.

(18) Liu, Y.; Yang, Y.; Shi, D.; Xiao, M.; Jiang, L.; Tian, J.; Zhang, G.; Liu, Z.; Zhang, X.; Zhang, D. Photo-/Thermal-Responsive Field-Effect Transistor upon Blending Polymeric Semiconductor with Hexaarylbiimidazole toward Photonically Programmable and Thermally Erasable Memory Device. *Advanced Materials* **2019**, *31* (44), 1–7. https://doi.org/10.1002/adma.201902576.

(19) Ahn, D.; Zavada, S. R.; Scott, T. F. Rapid, Photomediated Healing of Hexaarylbiimidazole-Based Covalently Cross-Linked Gels. *Chemistry of Materials* **2017**, *29* (16), 7023–7031. https://doi.org/10.1021/acs.chemmater.7b02640.

(20) Xiang, S. L.; Su, Y. X.; Zhao, P. J.; Li, C.; Zhu, M. Q. Visible-Light-Induced Scission and Rapid Healing of Polyurethane Elastomers Based on Photoswitchable Hexaarylbiimidazole Units. *Mater Chem Front* **2021**, *5* (3), 1364–1372. https://doi.org/10.1039/d0qm00857e.

(21) Sathe, S. S.; Ahn, D.; Scott, T. F. Re-Examining the Photomediated Dissociation and Recombination Kinetics of Hexaarylbiimidazoles. *Ind Eng Chem Res* **2015**, *54* (16), 4203–4212. https://doi.org/10.1021/ie504230c.

(22) Kosanke, R. M. PHOTOCHEMICAL BEHAVIOR OF HEXAARYLBIIMThAZOLE IN SOLID POLYMER MATRICE. *Https://Medium.Com/* **1992**, *5* (3), 551–556.

(23) MORITA, H.; KANAZAWA, K.; HASHIMOTO, K.; TSUBAME, T. Magnetic Field and Polymer Matrix Effects on Photochemical Reactions of Hexaarylbiimidazole in Solid Polymer Matrices. *Journal of Photopolymer Science and Technology* **1996**, *9* (1), 65–71. https://doi.org/10.2494/photopolymer.9.65.

(24) G. P. ARRIGHINI, M. MAESTRO, A. R. M. Magnetic Properties of Polyatomic Molecules. I. Magnetic Susceptibility of H2O, NH3, CH4, H2O2. *J. Phys. Chem* **1968**, *49* (2), 882–889. https://doi.org/https://doi.org/10.1063/1.1670155.

(25) Wapler, M. C.; Leupold, J.; Dragonu, I.; Von Elverfeld, D.; Zaitsev, M.; Wallrabe, U. Magnetic Properties of Materials for MR Engineering, Micro-MR and Beyond. *Journal of Magnetic Resonance* **2014**, *242*, 233–242. https://doi.org/10.1016/j.jmr.2014.02.005.

(26) Chen, Z.; Ellis, J.; Dahlberg, E. D. A Simple Technique to Measure the Magnetic Susceptibility of Liquids. *Review of Scientific Instruments*. 2012. https://doi.org/10.1063/1.4749847.

Chapter 5. Photoactuation of Pyrolytic Graphite Using an External Magnetic Field

5.1. Introduction

Most mechanical systems are powered by electricity (motors, piezoelectric actuators) or chemical fuels (engines, muscles). Light provides an alternative way to generate motion that does not require physical contact with the mechanical object and possesses multiple control parameters (wavelength, polarization, intensity). The challenge is to identify useful strategies that can transform photons into mechanical work. One common approach is to harness photochemical reactions in organized media like polymers or crystals to generate directional material deformations like bending and expansion.[1-4] Chemical reactions can be avoided if photothermal expansion is harnessed in a bimorph or piston type structure to generate similar types of motion.[5, 6] These approaches both rely on the incoming light field to supply the energy required to perform mechanical work. But if the sample is placed in a static field, then we can envision an alternative approach that uses light to switch the material's susceptibility to this field. Changing the material's susceptibility will change the object's potential energy in the applied field, and this change in potential is converted to mechanical motion as the object moves to a new potential energy minimum.

There are many types of potential energy fields that can be used to induce mechanical motion, including gravitational, electric, and magnetic. However, it is challenging for light to reversibly modulate an object's mass or net charge because these

changes would require the physical loss or rearrangement of particles. It is easier to envision how light could modify an object's magnetic susceptibility χ_{mag} by changing its internal electron configuration. In the simplest case, the creation of unpaired electrons would make an object paramagnetic, causing it to be attracted to a nearby magnet. This effect was originally used to prove the nature of the molecular triplet state by measuring the light-induced rotation or attraction of molecular crystals in a strong magnetic field.[7, 8] In the case of triplet detection, the creation of long-lived triplet states changed the sample from weakly diamagnetic to weakly paramagnetic, and the attraction of the paramagnetic object in a magnetic field gradient could be detected. Alternatively, photothermal heating of a ferromagnetic object above its Curie temperature can dramatically reduce its magnetic susceptibility. Omenetto and coworkers have taken advantage of the relatively low Curie temperature of CrO_2 to demonstrate various types of light-induced motion in polymer composites containing CrO_2 nanoparticles. [9-11] In principle, more long-lived spin-state isomers, spin cross-over states, or free radical states could also be used to change a material's magnetic susceptibility[12-14], although we could not find examples of these photophysical spin processes being harnessed to generate a mechanical response. Note that photothermal modification of χ_{mag} is distinct from the use of photothermal heating to soften a polymer matrix containing magnetic particles, which can also lead to mechanical motion.[15]

If an object is placed in a static magnetic field *B(z)*, the overall magnetic force experienced by an object with volume *V* is given by the expression[16]

$$F_{mag} = \frac{\chi_{mag} V}{\mu_0} \frac{\partial B(z)}{\partial z} B(z) \tag{5.1}$$

where μ_0 is the vacuum permittivity. Note that the sign of the force is determined by the sign of χ_{mag}: a diamagnetic material (χ_{mag}<0) will be repelled by the magnet, while a paramagnetic material (χ_{mag}>0) will be attracted, assuming that the gradient $\frac{\partial B(z)}{\partial z}$ <0 near the, i.e. *B(z)* decays away from the magnet surface, as is usually the case. For a diamagnetic object, the magnetic repulsive force can be balanced by its gravitational force, allowing it to find a mechanical equilibrium position where all or part of it levitates above the magnet.[17, 18] Using permanent magnets, a strongly diamagnetic material like graphite is required to observe this effect.[19-21] Levitation of an object makes it easier to use light to control its motion because friction becomes negligible, and small changes in χ_{mag} can more easily change the object's position or orientation.[22] It is possible to use photothermal heating to modify the field *B(z)* experienced by the graphite to induce motion[23] More commonly, χ_{mag} is modified by photothermal heating of the graphite itself. Previous workers have shown that using a laser to heat one section of a graphite disk causes it to shift position or even rotate.[16, 24, 25] In these experiments, the asymmetric irradiation induces local changes χ_{mag} via either purely thermal[26] or thermoelectric effects[27], and the anisotropy with respect to the vertical magnetic field that can be exploited to move the graphite In these experiments the main observable being the position of a horizontal piece of graphite suspended above a magnet array designed to maintain the horizontal orientation of the graphite.

In three dimensions, the situation is more complicated. The magnetic field induces a magnetic dipole within the object, which then tends to align itself in the applied field.[28] This magnetic torque acts to align both paramagnetic and diamagnetic objects parallel to the flux density vector[29] and depends on the shape of the object.[30] Of course, if a paramagnetic object is brought close to a magnet, the attractive force will overcome the alignment force and the object will adhere to the magnet. But a strongly diamagnetic material experiences both alignment and repulsive forces, which can combine with the gravitational force to create interesting levitation phenomena. In this chapter, we investigate whether photothermal heating can be used to control the angular deviation of levitated graphite. In **Figure 5.1**, we outline an experimental set-up in which a graphite plate is placed on top of a strong permanent magnet. There is a torque that works to align the plate parallel to the B-field lines, while the gravitational force pulling it down to the magnet

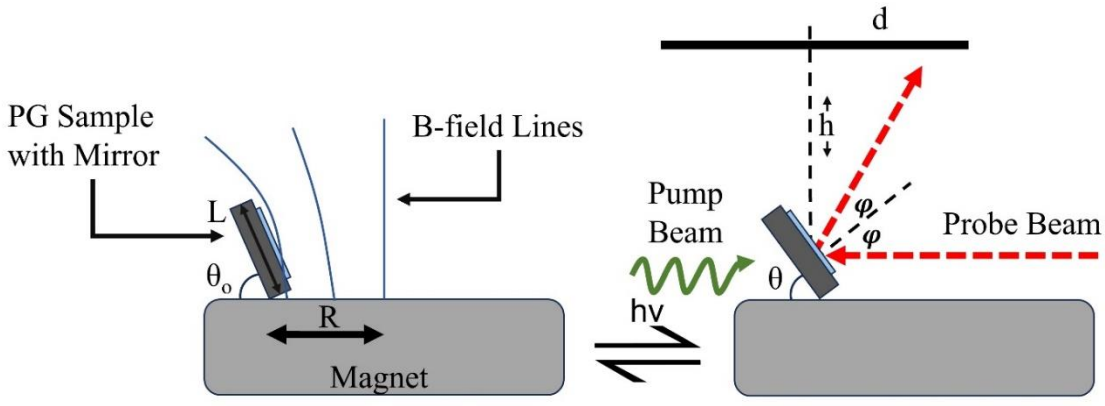

Figure 5.1. Schematic of tilt angle (θ) changes. A graphite plate with length L is placed at a distance R from the magnet center. An incoming pump beam heats the sample and lowering the tilt angle from θ_{eq} to θ. A probe beam reflection from the plate surface is used to monitor the tilt angle.

surface is counteracted by the levitation force. In Section III, we use computational modeling to demonstrate that this balance of forces can allow a stable equilibrium tilt angle to be attained for a graphite plate. We show that changing χ_{mag}, for example by changing its temperature by an amount ΔT, should change in the tilt angle θ by an amount $\Delta\theta$, with a linear relation between $\Delta\theta$ and ΔT. In Section IV we experimentally confirm that the tilt angle θ can be controlled by using laser irradiation to change the temperature of the graphite. Using this geometry, we have an object whose angular orientation can be controlled by an external light field, which is effectively a photomechanical object that does not rely on photochemical or photothermal expansion. We characterize the performance of this opto-magnetic mechanical system in terms of its response time, angular deviation, and intensity dependence. We show that it provides a stable, reproducible way to achieve large angular deviations that are controlled by an external light source. It is possible that this geometry could be adopted for light-controlled beam steering applications.

5.2. Calculated Response

In order to understand the origin of the laser-induced tilting of the graphite plate, we first analyze the forces acting on it. If the plate is placed on top of the magnet, the gravitational force acts on its center-of-mass to produce a torque that acts to rotate it downward to the magnet surface. This gravitational torque τ_g is given by

$$\tau_g = \frac{L}{2}\rho V g \cos(\theta) \tag{5.2}$$

where L is the length of the plate, V is the volume, ρ is the density, and g is the gravitation constant of 9.8 m/s^2. τ_g causes the plate to fall toward the surface, as usually observed when there is no other attractive or repulsive force between the tilted object and the surface. When the surface emits a strong magnetic field, however, it induces a magnetic dipole moment in the material that tends to align it parallel to the filed lines. The interaction of this induced dipole with the magnetic flux density vector produces a magnetic torque τ_{mag} which we calculate numerically using COMSOL. τ_{mag} gives rise to the well-known phenomenon of iron filings that align along the field lines when a magnet is placed on a sheet of paper. τ_{mag} causes both diamagnetic and paramagnetic objects to align parallel to the flux vector[29], but there is also a repulsive or attractive component that depends on the sign of the magnetic susceptibility χ_{mag}. For iron filings, the friction of the paper prevents these $\chi_{mag}>0$ objects from being drawn to the magnet surface, where they would collect into a dense clump. But if $\chi_{mag}<0$, then the repulsive force serves the same purpose as the frictional force for the iron filings and can keep the aligned object suspended above the magnet surface. By varying θ, both τ_g and τ_{mag} can be calculated and if there exists an angle θ_{eq} where the total torque $\tau_{tot}=\tau_{mag}+\tau_g=0$, then θ_{eq} corresponds to a stable equilibrium position.

In **Figure 5.2**, we show the calculated torques acting on a 5×5×0.83 mm plate located at R=3.25 cm from the magnet center. The torques for both $\chi_{mag}=-6.1\text{x}10^{-4}$ (corresponding to diamagnetic graphite) and for $\chi_{mag}=+6.1\text{x}10^{-4}$ (corresponding to a paramagnetic material) are plotted. The calculated data in **Figure 5.2a** show that the

paramagnetic solid has no stable θ_{eq} value where τ_{tot}=0. Both τ_g and τ_{mag} are negative except when τ_{mag} becomes slightly positive close to θ=90°. Since both torques are negative, τ_{tot}<0 for all θ values and the paramagnetic plate always falls to the surface. In order to counteract τ_g, we need a diamagnetic material like graphite that experiences a τ_{mag}>0 for all angles. For this situation, **Figure 5.2b** shows that τ_{mag} exactly cancels out τ_g at θ=29°. Furthermore,

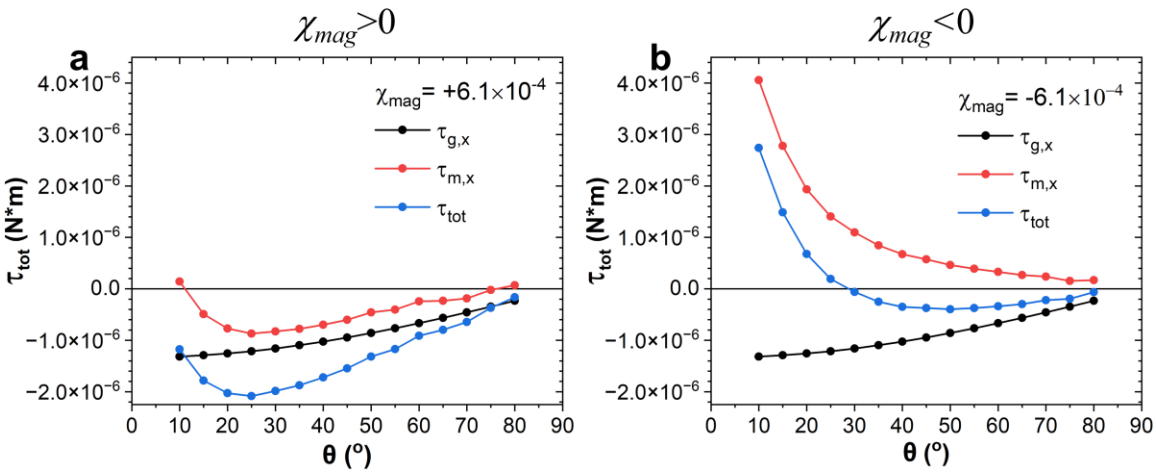

Figure 5.2. Calculated torque components τ_g (black), τ_{mag} (red) and $\tau_{tot}=\tau_{mag}+\tau_g$ (blue) for **a)** positive χ_{mag} (paramagnetic); and **b)** negative χ_{mag} (diamagnetic). There is a stable θ_{eq} = 29° for χ_{mag}<0 but no stable θ_{eq} for χ_{mag}>0.

the total torque τ_{tot} is positive for θ<29°, which means that if the plate is physically pushed down to $\theta<\theta_{eq}$, there is a restoring torque that will tilt it back up to θ_{eq}. Similarly, if the plate is pushed up to $\theta>\theta_{eq}$, τ_{tot} is negative, and the plate reduces its tilt back to θ_{eq}. Thus the θ_{eq}=29° angle corresponds to a stable equilibrium position.

The next question is how to control θ using an external light source. We first investigated the dependence of θ_{eq} on χ_{mag}. The calculated θ_{eq} values in **Figure 5.3** for different χ_{mag} values show that the tilt angle θ_{eq} has a roughly linear dependence on χ_{mag} for changes on the order of 10%. For larger changes, there is some indication that this

dependence deviates from linear, but we did not investigate this behavior in detail. In order to change χ_{mag} without perturbing the sample or magnetic field, we can utilize laser-induced heating. The dependence of graphite's magnetic susceptibility on temperature T takes the form,

$$\chi_{mag}(T) = \chi_0\left(1-\exp\left[-\frac{T_0}{T}\right]\right) \tag{5.3}$$

where χ_0=29×10^{-6} cgs and T_0=350 K.[31, 32] For temperatures T near T_0, this dependence can be approximated as

$$\chi_{mag}(\Delta T) \cong \chi_0\left(1-\frac{1}{e}-\frac{1}{e}\frac{\Delta T}{T_0}\right) \qquad \Delta T = T - T_0 \tag{5.4}$$

From the computational results in **Figure 5.3** and **Equation (5.4)**, we expect the change in tilt angle $\Delta\theta$ to depend linearly on the temperature change ΔT, and thus also on the laser power as long as $\Delta T << T$.

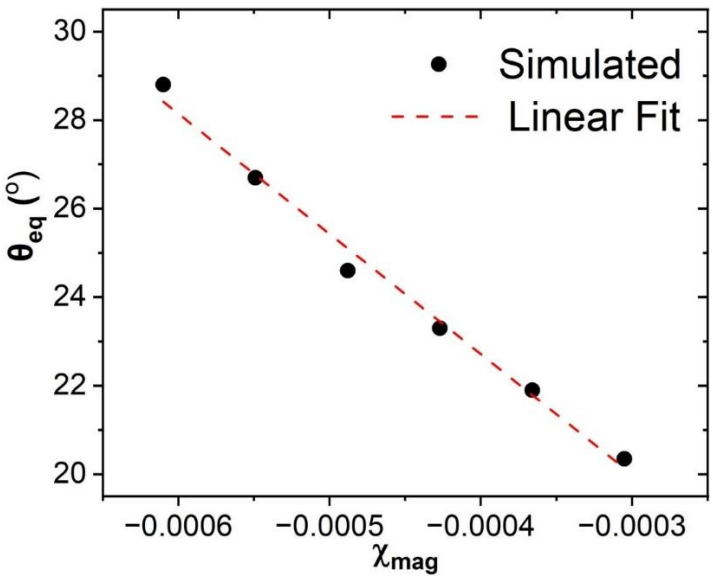

Figure 5.3. Linear dependence of θ_{eq} on χ_{mag} calculated using COMSOL (black points) and linear fit (red dashed line). The slope of the line is -2.7± 0.2 ×10^4.

The COMSOL calculations show that the laser-induced tilting of the graphite plate in an inhomogeneous magnetic field is possible for reasonable physical parameter values. However, it should be emphasized that these calculations did not quantitatively reproduce the experimental results in the following section. In particular, they did not exactly match the observed θ_{eq} *til*t angles, nor did they predict the existence of stable equilibrium angles at all values of R where stable tilting was experimentally observed. This lack of exact quantitative agreement is expected given the limitations of the calculations, including the neglect of graphite's anisotropic χ_{mag}, frictional forces, and the discrete nature of the simulations. But although precise calculation of tilt angles will require more sophisticated numerical approaches, the results in the following Section IV show that the COMSOL calculations qualitatively capture the experimental behavior of the laser-induced graphite tilting.

5.3. Experimental Results

The experimental set-up for the laser-controlled graphite tilting is pictured in **Figure 5.4**, along with the beam path for heating and angle measurement. A stable graphite plate tilt angle θ_{eq} could be found when the graphite contact point was located at 1 cm<R<3.7 cm on the top of the magnet, where R is the radial distance from the magnet center. If the plate was perturbed in either direction from its equilibrium position, it would return to the original position after it was released. When the plate was located at R<1 cm, near the center of the magnet, it was oriented close to θ_{eq}=90°. However, in this case, it could not recover when pushed flat against the magnet surface but remained lying flat. When the graphite plate was placed at R>3.7 cm, it flew off the side of the magnet,

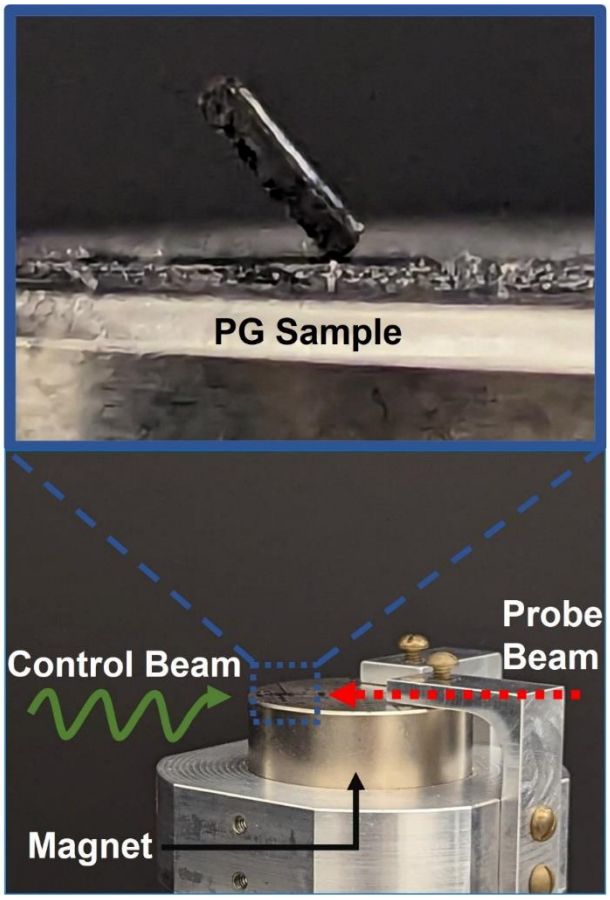

Figure 5.4. *Top*: Photograph of a 5×5×0.83 mm PG plate tilted on the magnet surface at R=2.5 cm in the absence of laser exposure. *Bottom*: Photograph of the entire experimental set-up, showing beam paths for pump and probe laser beams.

presumably because the large gradient force near the edge could overcome the gravitational force. θ_{eq} decreased as R increased, closely following the calculated flux density direction, as shown in **Figure 5.5**. These same calculations reproduced the z-dependent B-field strength at different R values (**Supporting Information, Figure S5.1**), providing evidence that the flux direction calculations were reasonably accurate. The graphite tilt angle was always less than that of the flux density vector angle, as expected due to gravity pulling the plate downward. The amount of deviation increased at larger R values (smaller θ_{eq} values), consistent with a larger gravitational torque on the graphite "lever".

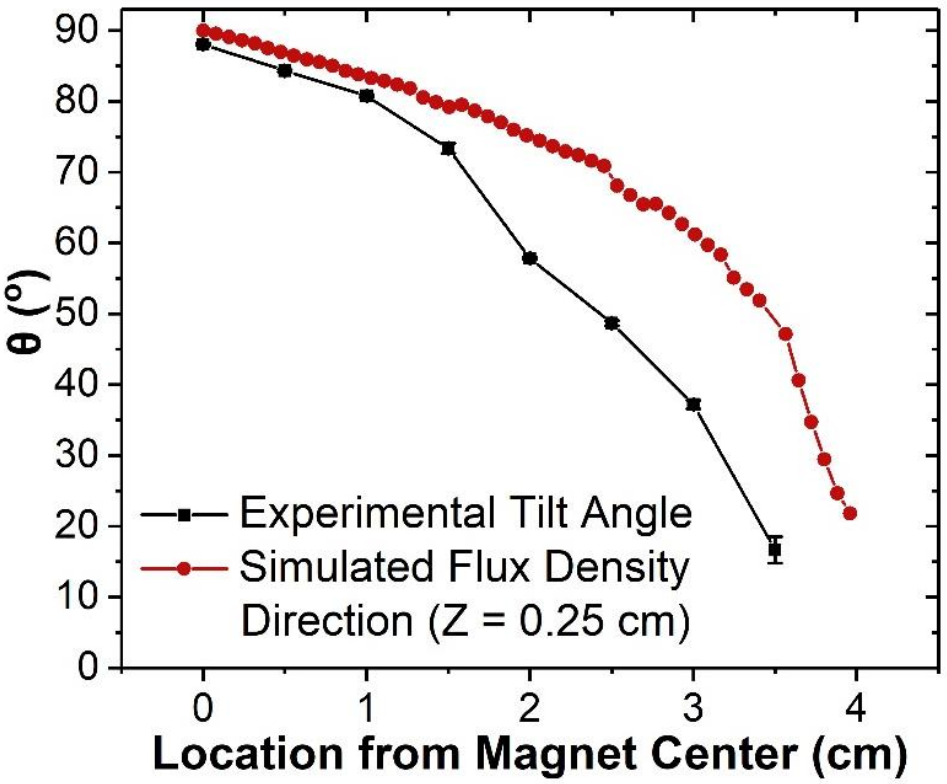

Figure 5.5. Flux density vector angle (red points) calculated at a vertical distance of 0.25 cm above the magnet, and the experimental PG tilt angle θ_{eq} measured at different distances R from the magnet center.

When the tilted graphite was exposed to a 532 nm cw laser beam, θ decreased until a new equilibrium position was achieved within about 60 seconds. When the laser was blocked, the plate returned to its original position on a similar timescale. The images in **Figure 5.6** show this sequence of events for a plate located at R=2.5 cm and an incident laser power of 400 mW. We note that identical tilting behavior was observed for inexpensive pyrolytic graphite and for a highly oriented pyrolytic graphite sample that had been machined to the same dimensions. This suggests that the observed behavior does not result from impurities or defects within the graphite, but instead arises from its intrinsic electronic properties. Abe and coworkers showed previously that heating leads to an increase in the density of unpaired spins in graphite[16], although it is possible that hot carrier

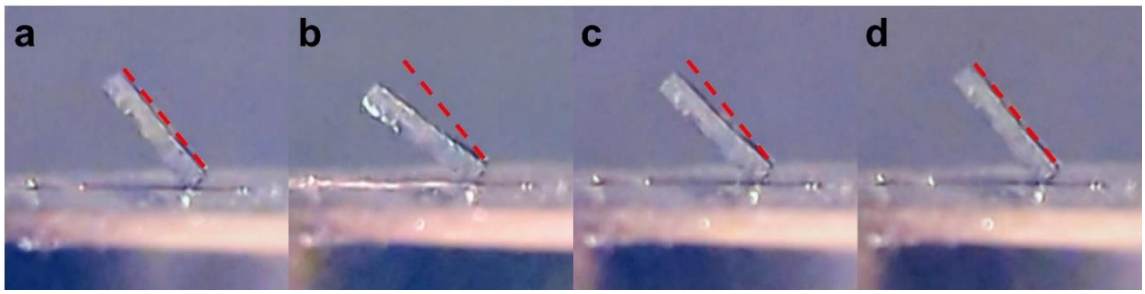

Figure 5.6. Photographs of the PG plate at *R*=2.5 cm during irradiation by a 400 mW 532 nm laser beam: **a)** Initial position marked by a red dashed bar before laser exposure, **b)** after one minute of laser exposure, **c)** 10 seconds after 1 minute laser exposure is ended, and **d)** one minute after laser exposure is ended.

redistribution after photoexcitation enhances the spin population even further.[27] This paramagnetic contribution partially cancels out the diamagnetic term, reducing τ_{mag} and leading to a smaller θ tilt angle.

In **Figure 5.7a**, we show $\theta(t)$ obtained by measuring the probe beam deflection angle for a series of these experiments. The temporal on and off deflection profiles can be fit to exponential functions of the form

$$\text{Laser on: } \theta(t) = \theta_{eq} - \Delta\theta\left(1 - \exp\left[-\frac{t}{\tau_{on}}\right]\right) \tag{5.5a}$$

$$\text{Laser off: } \theta(t) = \theta_{eq} - \Delta\theta \exp\left[-\frac{t}{\tau_{off}}\right] \tag{5.5b}$$

Interestingly, the τ_{on} and τ_{off} response times did not depend strongly on the laser power, always hovering around τ_{on}~15 s after the laser was turned on and τ_{off}~12 s after it is blocked (**Supporting Information, Figure S5.2 and Table S5.1**). In order to quantitatively analyze the origin of these time constants, we would have to analyze heat transfer and loss in the graphite plate, taking into account both radiative and convective mechanisms, but such an analysis is beyond the scope of the present chapter. Once the new

equilibrium angle is reached by the heated graphite, it is stable while the laser remains on. The net angle change $\Delta\theta$ depends on laser power, and the final temperature change ΔT exhibits a parallel dependence on laser power (**Figure 5.7b**), as predicted in Section III. This data establishes the photothermal mechanism as the origin of the angle change.

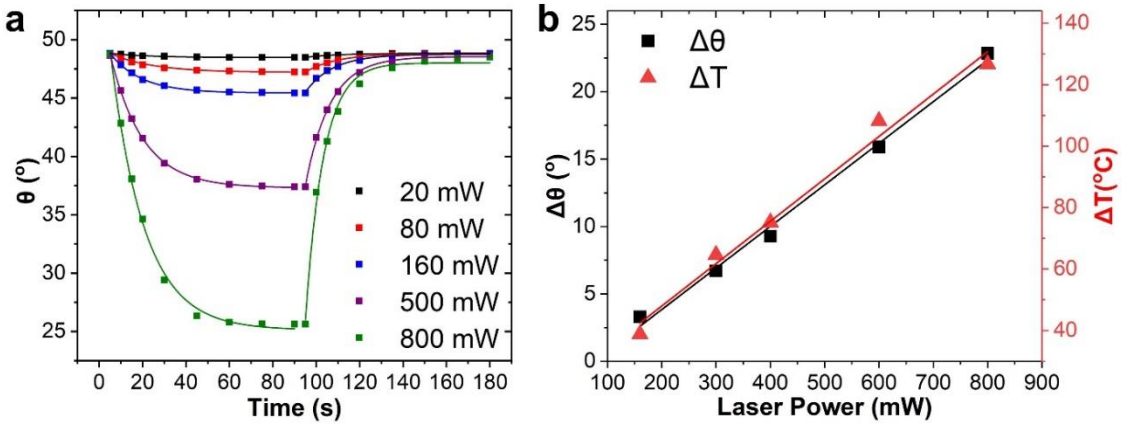

Figure 5.7. a) Time dependence of tilt angle θ for a pyrolytic graphite plate located at R=2.5 cm and measured with different laser powers: 20 mW (black), 80 mW (red), 160 mW (blue), 600 mW (purple), 800 mW (green). Laser exposure begins at 5 seconds and ends at 95 seconds. The solid lines are exponential fits to the data using Equations (5.5a) and (5.5b); **b)** Linear dependence of $\Delta\theta$ and ΔT on laser power, consistent with predictions of Equations (5.3) and (5.4).

One concern is that repeated heating may affect the reversibility of the laser-induced tilting. To assess this possibility, cycling behaviors for 160 mW and 500 mW laser exposure are shown in **Figure 5.8a**. At both powers, we detected a slight 3-5% drop in the $\Delta\theta$ value over the first 2-3 cycles, after which it stabilized. Higher laser powers resulted in a larger initial decrease in $\Delta\theta$. The decrease in the normalized $\Delta\theta$, plotted in **Figure 5.8b**, is consistent with a brief "burn in" period. The magnetic and electronic properties of graphite are sensitive to thermal annealing[33, 34], so it is possible that even the relatively low temperature changes achieved with our laser can affect unstable regions in the graphite

microstructure. After these regions are annealed, the material becomes robust with respect to additional laser exposure.

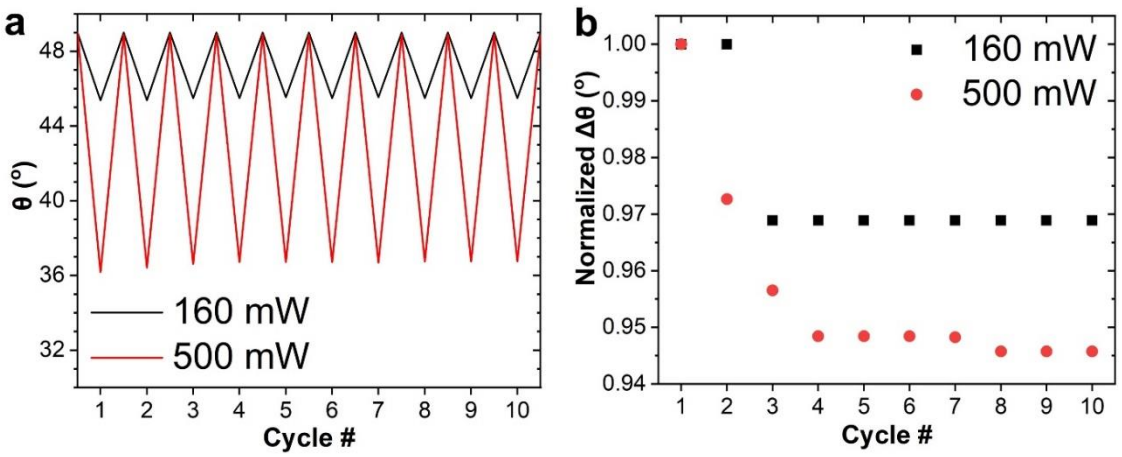

Figure 5.8. **a)** Cycling of PG tilt angle, recorded for a plate at R=2.5 cm, for 1 minute laser exposures followed by 1 minute recover for 160 mW and 500 mW laser powers; **b)** Change in normalized Δθ value during laser cycling, showing a slight decrease during the first 10 cycles.

When the incident laser power was increased beyond 800 mW, the response of $\Delta\theta$ became highly nonlinear. For example, when 1.2 W of laser power was used, θ would decrease gradually, then the plate would suddenly drop flat against the magnet surface. It would spring back to its original position once the laser was blocked. In **Figure 5.9**, we plot $\Delta\theta(t)$ for P=1.2 W, which led to a maximum temperature increase of 162°C. Both the drop (10 s) and recovery (2 s) times are faster than for P<500 mW. This large $\Delta\theta$ was stable over 10 irradiation cycles (**Figure 5.8b**). If the laser was left on, the graphite plate would oscillate up and down as it moved in and out of the beam path. The nonlinear change in θ *at h*igher temperatures cannot be explained by the simple theory presented in Section III. We hypothesize that the lower χ_{mag} at the higher temperatures allows the levitation force to be overcome by gravity, leaving no stable θ_{eq}. When the plate cools out of the laser beam

path, the levitation force recovers and allows the plate to return to its original tilt. Again, a full understanding of these dynamics would require detailed modeling of heat transfer and forces, which is beyond the scope of this chapter. We present it here as an interesting observation that may spur more sophisticated theoretical treatments of this phenomenon.

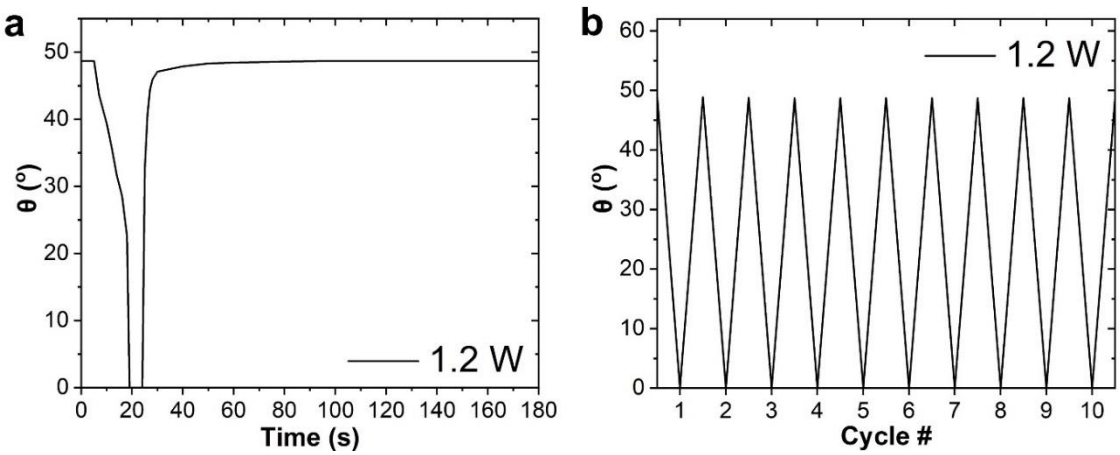

Figure 5.9. a) Tilt angle θ vs time for a PG plate located at R=2.5 cm during exposure to a 1.2 W laser beam. The laser is turned on at 5 seconds and then the θ begins to decrease. At 19 seconds, θ suddenly drops to 0 and the plate lies flat on the magnet. The laser is then turned off. At 24 seconds, the plate pops back up and then returns to its original θ_{eq}. **b)** cyclical oscillations observed at 1.2 W with the sample always returning to its original θ_{eq}. The laser is turned off once the θ drops to 0 and is left off for 5 minutes between each cycle to ensure full recovery.

5.4. Conclusion

In this chapter, we have shown computationally that a balance of magnetic and gravitational forces can lead to a stable tilt for a diamagnetic plate resting on the surface of a strong magnet. The model predicts that the tilt angle θ of the plate depends linearly on χ_{mag}, which in turn can be modified by changing the plate temperature. The qualitative predictions of this model were experimentally confirmed by using a laser to heat a graphite plate that can pivot on top of a strong permanent magnet. This photothermal method provided a noncontact way to control θ with high precision for laser powers up to 800 mW.

The laser induced tilt $\Delta\theta$ was linearly dependent on incident laser power and stabilized within 2-3 irradiation cycles, suggesting that the graphite could act as a robust photomechanical transducer. Larger ΔT changes at high laser powers were observed to lead to nonlinear angle changes and even oscillatory behavior. Overall, the results in this chapter suggest that photothermal tilting of a graphite plate levitated in a static magnetic field can function as a laser-controlled beam steering device.

5.5 Supporting Information

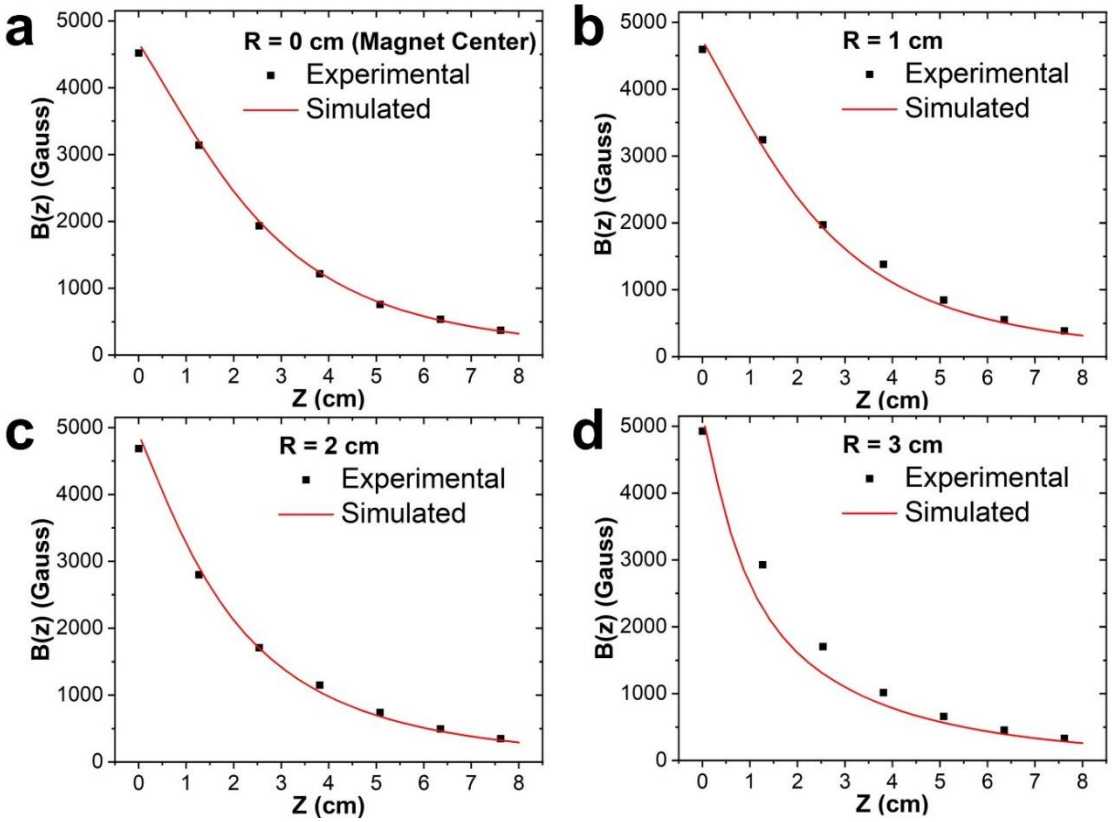

Figure S5.1. Comparison of theoretical and experimental data on flux density at different heights Z for: **a)** R = 0 cm (Magnet center), **b)** R = 1 cm, **c)** R = 2 cm, and **d)** R = 3 cm.

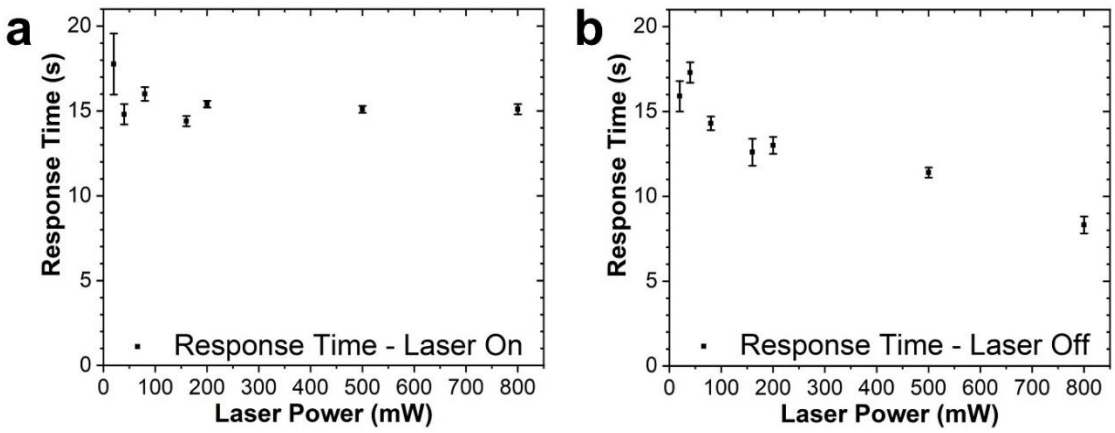

Figure S5.2. Response time variations plotted against laser power with data points acquired at R = 2.5 cm for **a)** when the laser is on and **b)** when the laser is turned off.

Table S5.1. Response times from the plots in Figure S2.

Response Times:	Laser On (s)	Laser Off (s)
20 mW	17.76 ± 1.8	15.9 ± 0.9
40 mW	14.8 ± 0.6	17.3 ± 0.6
80 mW	16.0 ± 0.4	14.3 ± 0.4
160 mW	14.4 ± 0.3	12.6 ± 0.8
200 mW	15.4 ± 0.2	13.0 ± 0.5
500 mW	15.1 ± 0.2	11.4 ± 0.3
800 mW	15.1 ± 0.3	8.3 ± 0.5

5.6 References

(1) Ikeda, T.; Mamiya, J.-i.; Yu, Y., Photomechanics of Liquid-Crystalline Elastomers and Other Polymers. *Angew. Chem. Int. Ed.* **2007,** *46*, 506-528. **doi:** 10.1002/anie.200602372

(2) Kim, T.; Zhu, L.; Al-Kaysi, R. O.; Bardeen, C. J., Organic photomechanical materials. *ChemPhysChem* **2014,** *15*, 400-414. **doi:** 10.1002/cphc.201300906

(3) Naumov, P.; Chizhik, S.; Panda, M. K.; Nath, N. K.; Boldyreva, E., Mechanically Responsive Molecular Crystals. *Chem. Rev.* **2015,** *115*, 12440-12490. **doi:** 10.1021/acs.chemrev.5b00398

(4) White, T. J., *Photomechanical Materials, Composites, and Systems*. 1 ed.; Wiley: Hoboken, New Jersey, 2017.

(5) Han, B.; Zhang, Y.-L.; Chen, Q.-D.; Sun, H.-B., Carbon-Based Photothermal Actuators. *Adv. Funct. Mater.* **2018**, 1802235. **doi:** 10.1002/adfm.201802235

(6) Lui, B. F.; Bardeen, C. J., Using Small Molecule Absorbers to Create a Photothermal Wax Motor. *Small* **2022,** *18*, 2105356. **doi:** 10.1002/smll.202105356

(7) Lewis, G. N.; Calvin, M.; Kasha, M., Photomagnetism. Determination of the Paramagnetic Susceptibility of a Dye in Its Phosphorescent State. *J. Chem. Phys.* **1949,** *17*, 804-812. **doi:** 10.1063/1.1747403

(8) Evans, D. F., Photomagnetism of Triplet States of Organic Molecules. *Nature* **1955,** *176*, 777-778. **doi:** 10.1038/176777a0

(9) Li, M.; Wang, Y.; Chen, A.; Naidu, A.; Napier, B. S.; Li, W.; Rodriguez, C. L.; Crooker, S. A.; Omenettoa, F. G., Flexible magnetic composites for light-controlled actuation and interfaces. *Proc. Nat. Acad. Sci.* **2018,** *115*, 8119–8124. **doi:** 10.1073/pnas.1805832115

(10) Li, M.; Kim, T.; Guidetti, G.; Wang, Y.; Omenetto, F. G., Optomechanically Actuated Microcilia for Locally Reconfigurable Surfaces. *Adv. Mater.* **2020,** *32*, 2004147. **doi:** 10.1002/adma.202004147

(11) Jha, A. K.; Douglas, E. S.; Li, M.; Fucetola, C.; Omenetto, F. G., Demonstration of magnetic and light-controlled actuation of a photomagnetically actuated deformable mirror for wavefront control. *Opt. Engin.* **2021,** *60*, 124102. **doi:** 10.1117/1.OE.60.12.124102

(12) Sato, O., Photoinduced magnetization in molecular compounds. *J. Photochem. Photobio. C* **2004,** *5*, 203–223. **doi:** 10.1016/j.jphotochemrev.2004.10.001

(13) Felts, A. C.; Slimani, A.; Cain, J. M.; Andrus, M. J.; Ahir, A. R.; Abboud, K. A.; Meisel, M. W.; Boukheddaden, K.; Talham, D. R., Control of the Speed of a Light-

Induced Spin Transition through Mesoscale Core–Shell Architecture. *J. Am. Chem. Soc.* **2018,** *140*, 5814–5824. **doi:** 10.1021/jacs.8b02148

(14) Paquette, M. M.; Plaul, D.; Kurimoto, A.; Patrick, B. O.; Frank, N. L., Opto-Spintronics: Photoisomerization-Induced Spin State Switching at 300 K in Photochrome Cobalt–Dioxolene Thin Films. *J. Am. Chem. Soc.* **2018,** *140*, 14990–15000. **doi:** 10.1021/jacs.8b09190

(15) Liu, J. A.-C.; Gillen, J. H.; Mishra, S. R.; Evans, B. A.; Tracy, J. B., Photothermally and magnetically controlled reconfiguration of polymer composites for soft robotics. *Sci. Adv.* **2019,** *5*, eaaw2897. **doi:** 10.1126/sciadv.aaw2897

(16) Kobayashi, M.; Abe, J., Optical Motion Control of Maglev Graphite. *J. Am. Chem. Soc.* **2012,** *134*, 20593–20596. **doi:** 10.1021/ja310365k

(17) Simon, M. D.; Geim, A. K., Diamagnetic levitation: Flying frogs and floating magnets. *J. Appl. Phys.* **2000,** *87*, 6200-6204. **doi:** 10.1063/1.372654

(18) Subramaniam, A. B.; Yang, D.; Yu, H.-D.; Nemiroski, A.; Tricard, S.; Ellerbee, A. K.; Soh, S.; Whitesides, G. M., Noncontact orientation of objects in three-dimensional space using magnetic levitation. *Proc. Nat. Acad. Sci.* **2014,** *111*, 12980–12985. **doi:** 10.1073/pnas.1408705111

(19) Waldron, R. D., Diamagnetic Levitation Using Pyrolytic Graphite. *Rev. Sci. Instrum.* **1966,** *37*, 29–35. **doi:** 10.1063/1.1719946

(20) Niu, C.; Lin, F.; Wang, Z. M.; Bao, J.; Hu, J., Graphene levitation and orientation control using a magnetic field. *J. Appl. Phys.* **2018,** *123*, 044302. **doi:** 10.1063/1.5005539

(21) Huang, J.; Zhao, P.; Zhang, C.; Xie, J.; Xia, N.; Fu, J., Stable Levitation of Pyrolytic Graphite Above Circular Magnet Arrays. *IEEE Trans. Magnet.* **2022,** *58*, 8500111. **doi:** 10.1109/TMAG.2022.3182214

(22) Kim, J. H.; Pyo, J.-B.; Kim, T.-S., Highly Mobile Levitating Soft Actuator Driven by Multistimuli-Responses. *Adv. Mater. Intefaces* **2020,** *7*, 2001051. **doi:** 10.1002/admi.202001051

(23) Iwata, Y. M. A. T. T.; Otani, Y., Optically driven method for magnetically levitating diamagnetic material using photothermal effect. *J. Appl. Phys.* **2012,** *111*, 023909. **doi:** 10.1063/1.3675182

(24) Young, J.; Biggs, H.; Yee, S.; ElBidweihy, H., Optical control and manipulation of diamagnetically levitated pyrolytic graphite. *AIP Advances* **2019,** *9*, 125038. **doi:** 10.1063/1.5129886

(25) Ewall-Wice, M.; Yee, S.; DeLawder, K.; Montgomery, S. R.; Joyce, P. J.; Brownell, C.; ElBidweihy, H., Optomechanical Actuation of Diamagnetically

Levitated Pyrolytic Graphite. *IEEE Trans. Magnet.* **2019,** *55*, 2501506. **doi:** 10.1109/TMAG.2019.2892332

(26) Fujimoto, M.; Koshino, M., Diamagnetic levitation and thermal gradient driven motion of graphite. *Phys. Rev. B* **2019,** *100*, 045405. **doi:** 10.1103/PhysRevB.100.045405

(27) Yee, S.; Oney, L.; Cosby, T.; Durkin, D. P.; ElBidweihy, H., Photothermal actuation of levitated pyrolytic graphite revised. *APL Mater.* **2021,** *9*, 101107. **doi:** 10.1063/5.0061390

(28) Vereda, F.; Vicente, J. d.; Hidalgo-lvarez, R., Physical Properties of Elongated Magnetic Particles: Magnetization and Friction Coefficient Anisotropies. *ChemPhysChem* **2009,** *10*, 1165–1179. **doi:** 10.1002/cphc.200900091

(29) Laufer, A. R., The Orientation of Paramagnetic and Diamagnetic Rods in Magnetic Fields. *Am. J. Phys.* **1951,** *19*, 275-279. **doi:** 10.1119/1.1932802

(30) Prozorov, R.; Kogan, V. G., Effective Demagnetizing Factors of Diamagnetic Samples of Various Shapes. *Phys. Rev. Appl.* **2018,** *10*, 014030. **doi:** 10.1103/PhysRevApplied.10.014030

(31) Reynolds, W. N., *Physical Properties of Graphite*. Elsevier: London, 1968.

(32) Kelly, B. T., *Physics of Graphite*. Applied Science Publishers: London, 1981.

(33) Fischbach, D. B., Diamagnetic Susceptibility of Pyrolytic Graphite. *Phys. Rev.* **1961,** *123*, 1613-1614. **doi:** 10.1103/PhysRev.123.1613

(34) Gallais, L.; Vidal, T.; Lescoute, E.; Pontillon, Y.; Rullier, J. L., High power continuous wave laser heating of graphite in a high temperature range up to 3800 K. *J. Appl. Phys.* **2021,** *129*, 043102 **doi:** 10.1063/5.0033530

Chapter 6. Conclusions and Future Outlook

This dissertation has presented a comprehensive study on the manipulation of photomechanical motion through various methods, highlighting the intricate interplay between light and matter.

Our exploration began with investigating the properties of (2,2,6,6-tetramethylpiperidine-1-oxyl (TEMPO), a stable free radical, demonstrating controlled mechanical motion. We discovered TEMPO's supercooling phase and characterized its supercooling properties. Remarkably, TEMPO can remain supercooled for months if lrft undisturbed and shows mechanical robustness to perturbations. Crystals of TEMPO can form in sample vials and can be crystalized in remote locations. The ability of TEMPO to absorb visible light enables us to melt TEMPO with a continuous-wave (cw) laser, creating a supercooled liquid when cooled to room temperature, and then solidify the same sample using a nanosecond pulse laser. These supercooling properties introduce a new class of materials with potential applications in energy storage and beyond.

By introducing light, we utilized the properties of ortho-chloro-hexaarylbiimidizole (HABI) to photochemically generate triphenylimidazolyl radicals (TPIRs), which altered the material's magnetic susceptibility (χ_{mag}). This alteration enabled photomechanical motion under an external magnetic field. Although we successfully demonstrated photomechanical motion using HABI, the results were not consistently reproducible. One potential application of this technology could be coating HABI films with a highly opaque

material, such as black paint. This coating could transform HABI films into shutters capable of blocking and unblocking incoming light beams.

Lastly, working with pyrolytic graphite (PG) allowed for a photothermal approach for photomechanical motion under an external magnetic field. We demonstrated that a diamagnetic plate's stable tilt on a strong magnet can be computationally modeled as a balance between magnetic and gravitational forces, with the tilt angle (θ) linearly dependent on χ_{mag}, which varies with temperature. Experimental validation was achieved by heating a PG plate with a laser, allowing it to pivot on a strong magnet, showcasing a precise, noncontact method to adjust θ using laser power up to 800 mW. The laser-induced tilt showed a linear response to laser power, stabilizing after 2-3 irradiation cycles, indicating the PG's potential as a durable photomechanical transducer. The findings suggest that photothermal tilting of a levitated graphite plate in a magnetic field can serve as a laser-controlled beam steering mechanism.

In conclusion, this dissertation contributes significantly to the field of photomechanical motion, offering novel insights and methodologies that could revolutionize how we interact with and manipulate materials at the macroscopic level.